Topology optimization of silicon anode structures for lithium-ion battery applications

A Thesis by

Sarah L. Mitchell

In Partial Fulfillment of the Requirements
for the Degree of
Doctor of Philosophy

California Institute of Technology
Pasadena, California

2016
(Defended 5 February 2016)

For Mum, Dad, and Steffie

Acknowledgments

I would like to thank my advisor, Professor Michael Ortiz, for his support and guidance throughout my time at Caltech. It has been a true honour and privilege to work with such an esteemed scientist. To the members of my thesis committee, Professor Sergio Pellegrino, Professor Dennis Kochmann, and Professor Fehmi Cirak, I would like to express my sincere gratitude for their time, guidance, feedback, and teachings.

I gratefully acknowledge support from Robert Bosch GmbH through the Bosch Energy Research Network (BERN) Project No.: 07-15-CS13, and from the U.S. National Science Foundation through the Partnership for International Research and Education (PIRE) on Science at the Triple Point Between Mathematics, Mechanics and Materials Science, Award Number 0967140. I would like to express my gratitude to Professor K. Svanberg for providing the MMA and GCMMA optimization subroutines. I am also very thankful for the generous support of Fulbright New Zealand and the North Harbour Club.

I wish to extend my warmest thanks to Lydia, a truly kind and caring person, for all her help and encouragement on this journey. Also, many thanks to Cheryl Geer, who was always available to patiently answer my questions.

I thank my kiwi ladies, Jenny and Victoria, who I was so lucky to meet all those years ago. No matter where in the world our lives take us, we always manage to find a way back to each other. I am truly grateful for their love and friendship. Many thanks to Natalie, a genuinely kind-hearted person who was always forthcoming with words of encouragement on our many lunch dates by the turtle pond. And to Wendy, who came into my life at a turning point and quickly became a pillar of support. I couldn't have done this without her.

Most importantly, I would like to thank my family. To my grandparents, who were always so genuinely delighted to hear from me, I thank them for their love and support. To my sister Steffie, my wingwoman and best friend who made my Caltech experience infinitely more

awesome, thank you so much for being the best big sister a girl could ask for. And finally to my Mum and Dad, whose love, encouragement, and unwavering faith in me means absolutely everything. I truly appreciate all they have done for me, and I feel so incredibly fortunate to be their daughter.

Abstract

This thesis presents a topology optimization methodology for the systematic design of optimal multifunctional silicon anode structures in lithium-ion batteries. In order to develop next generation high performance lithium-ion batteries, key design challenges relating to the silicon anode structure must be addressed, namely the lithiation-induced mechanical degradation and the low intrinsic electrical conductivity of silicon. As such, this work considers two design objectives of minimum compliance under design dependent volume expansion, and maximum electrical conduction through the structure, both of which are subject to a constraint on material volume. Density-based topology optimization methods are employed in conjunction with regularization techniques, a continuation scheme, and mathematical programming methods. The objectives are first considered individually, during which the iteration history, mesh independence, and influence of prescribed volume fraction and minimum length scale are investigated. The methodology is subsequently extended to a bi-objective formulation to simultaneously address both the compliance and conduction design criteria. A weighting method is used to derive the Pareto fronts, which demonstrate a clear trade-off between the competing design objectives. Furthermore, a systematic parameter study is undertaken to determine the influence of the prescribed volume fraction and minimum length scale on the optimal combined topologies. The developments presented in this work provide a foundation for the informed design and development of silicon anode structures for high performance lithium-ion batteries.

Contents

List of Figures

List of Tables

Nomenclature

Acronyms

BESO	Bi-directional Evolutionary Structural Optimization
CMC	Constant mean curvature
CONLIN	Convex linearization method
ESO	Evolutionary Structural Optimization
GCMMA	Globally convergent method of moving asymptotes
Li-ion	Lithium-ion
MBB	Messerschmidt-Bölkow-Blohm
MEMS	Microelectromechanical systems
MMA	Method of moving asymptotes
OC	Optimality criteria
RAMP	Rational Approximation of Material Properties
SEI	Solid-electrolyte interface
SIMP	Solid Isotropic Material with Penalization
SiNW	Silicon nanowire
SOFC	Solid oxide fuel cell
TSC	Thermal stress coefficient

Commonly Used Symbols

$\alpha(\tilde{x}_e)$	Thermal expansion coefficient
$\mathbf{B}_e$	Element strain-displacement matrix
$\mathbf{C}_e(\tilde{x}_e)$	Constitutive matrix
$\bar{\mathbf{C}}_e$	Constitutive matrix for a unit Young's modulus
$c(\tilde{\mathbf{x}})$	Compliance
$\mathbf{D}_e(\tilde{x}_e)$	Element conductivity matrix
$\boldsymbol{\epsilon}_e^*(\tilde{x}_e)$	Element volumetric strain vector
e	Element
$E_e(\tilde{x}_e)$	Element Young's modulus
$\mathbf{F}$	Global design independent force vector
$\mathbf{F}(\tilde{\mathbf{x}})$	Global design dependent force vector
$\mathbf{F}^m$	Global mechanical force vector
$\mathbf{F}^v(\tilde{\mathbf{x}})$	Global volumetric expansion load vector
$\mathbf{f}_e(\tilde{x}_e)$	Element force vector
$\mathbf{f}_e^v(\tilde{x}_e)$	Element volumetric expansion load vector
$\bar{\mathbf{f}}_e^v$	Density independent integral term of $\mathbf{f}_e^v(\tilde{x}_e)$
$\Gamma(\tilde{x}_e)$	Interpolation function
$\gamma(\tilde{x}_e)$	Volume expansion load coefficient
$\mathbf{K}(\tilde{\mathbf{x}})$	Global stiffness or conductance matrix
$\mathbf{k}_e(\tilde{x}_e)$	Element stiffness or conductance matrix
ν	Poisson's ratio

N	Number of elements
Ω	Reference domain
ϕ	The vector [1 1 1 0 0 0] for a three-dimensional analysis
$\mathbf{\Phi}(\tilde{\mathbf{x}})$	Global voltage vector
p	Penalization parameter
r	Filter radius
$\Delta T(\tilde{x}_e)$	Element temperature change
$\mathbf{T}(\tilde{\mathbf{x}})$	Global temperature vector
$\mathbf{t}_e(\tilde{x}_e)$	Element temperature vector
$\mathbf{U}(\tilde{\mathbf{x}})$	Global displacement vector
$\mathbf{u}_e(\tilde{x}_e)$	Element displacement vector
$V(\tilde{\mathbf{x}})$	Material volume
V_0	Design domain volume
v_e	Element volume
V_f^{max}	Upper limit on volume fraction
V_f^{min}	Lower limit on volume fraction
w_c	Conduction objective weighting factor
w_s	Structural objective weighting factor
$\tilde{\mathbf{x}}$	Vector of physical densities
$\mathbf{x}$	Vector of design variables, the element densities
$\tilde{x}_e$	Physical element density
x_e	Element design variable

Chapter 1

Introduction

This chapter provides an overview of lithium-ion battery technology and summarizes the key benefits and current limitations of improving battery performance using silicon anode structures. Approaches to overcoming these challenges are subsequently reviewed in order to motivate the use of topology optimization methods for the design of multifunctional high performance silicon anode structures.

1.1 The lithium-ion battery

A battery is a collection of electrochemical cells that store electrical energy in the form of chemical energy. There are two types of batteries: primary and secondary batteries. In primary batteries the stored chemical energy can be converted to electricity only once, whilst secondary batteries are rechargeable. A dominant high energy storage device is the lithium-ion (Li-ion) battery, which is a secondary battery used to power electric cars, phones, laptops and other portable devices. A schematic of a Li-ion cell during discharge is depicted in Figure 1.1. The Li-ion battery typically consists of a graphite anode and a lithium metal oxide cathode, i.e., lithium cobalt oxide ($LiCoO_2$). The electrodes have different chemical potentials, with reactions at the anode taking place at lower electrode potentials than at the cathode. As such, the anode and cathode are commonly referred to as the negative and positive electrodes, respectively. The electrodes are separated by an ion-conducting electrolyte that is electrically insulating and may be in the form of an aqueous, gel or solid solution of lithium salt in a mixed organic solvent. Within the electrolyte is a semi-permeable membrane that separates the two electrodes and allows ions but not electrons to pass.

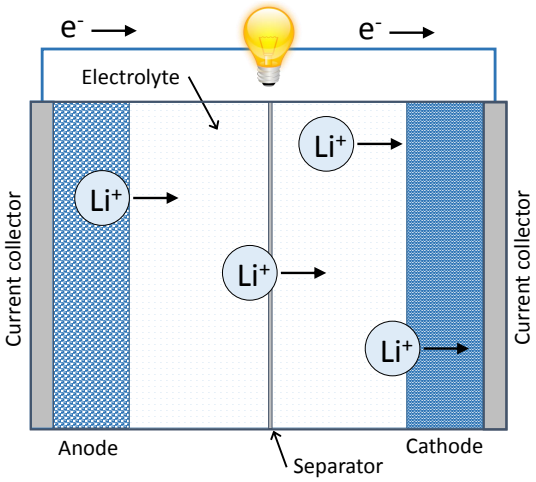

Figure 1.1: A Li-ion cell during discharging.

Electrochemical reactions occur spontaneously when the two electrodes are connected by an electronic load, allowing chemical energy to be converted to electrical energy by electron transfer through the circuit from the more negative to the more positive potential. During battery discharge (Figure 1.1), lithium atoms at the anode-electrolyte interface become oxidized. The atoms each loose an electron which travels from the anode material to the current collector and through the external circuit where the electrons perform work, such as lighting a bulb or powering a mobile phone, and through to the cathode. At the same time, the remaining Li cations leave the anode, enter into the electrolyte and diffuse through the separator to the cathode where a reduction reaction takes place. To recharge the battery, an external electrical power source applies an opposite sense voltage at least as large at that measured during discharge. The lithium atoms leave the cathode and ionize into Li-ions with the release of an electron for each atom. These Li-ions migrate through the electrolyte and are intercalated into the molecular structure of the anode while the electrons travel through the external circuit. This process of intercalation is also referred to as an insertion reaction or lithiation.

A battery is typically enclosed in packaging that provides structural and chemical protection, preventing any parasitic reactions with air and moisture. Li-ion batteries are manufactured in a range of shapes and sizes specific to their application. For example, coin cells are used in small devices such as hearing aids (Oudenhoven et al., 2011), while microelectronics may require a footprint area of less than several square millimetres.

Battery performance may be quantified by several characteristics. The *specific capacity*

is the quantity of electricity involved in the electrochemical reaction, expressed in terms of mass (units of Ah/kg). The specific capacity relates to the amount of lithium ions that can be reversibly inserted and extracted during charge and discharge, and is determined by the cell's chemistry (Ceder et al., 2011). In practice the full capacity cannot be achieved due to mass calculations involving non-reactive components such as binders, conducting particles, separators, electrolytes, current collectors, substrates and packaging. Furthermore, batteries undergo incomplete chemical reactions due to poor reactivity at the electrode/electrolyte interface or active materials being unavailable to the reaction (Aifantis et al., 2010). The *specific energy density* is the energy that can be derived per unit weight of the cell and is a function of the cell's voltage and specific capacity (units of Wh/kg). Efficient battery design requires maximum energy density, or in other words the highest energy level for the minimum mass. This theoretical value does not account for losses incurred in the ionic conductor, current collectors or packaging, therefore practical values are typically significantly lower. For example, the maximum theoretical specific energy density for a 4.2 V Li-ion cell with a graphite anode ranges between 380-460 Wh/kg, while an actual specific energy density of 160 Wh/kg may be practically achieved (Aifantis et al., 2010). *Specific power density* indicates the rate at which the energy can be delivered (units of W/kg). The cell design and kinetics determine the power density. Capacity, energy density and power density may also be expressed in volumetric form, which places constraints on the size rather than the weight of the battery. A trade-off exists between achieving high energy density and high power density. For example, thicker and less porous layers of active material in an electrode will maximize the volumetric energy density, while thinner and more porous layers will maximize power density by allowing faster charge transport. The *cycle life* is defined as the number of charge/discharge cycles the battery can undergo before capacity falls to 80%. Current commercial Li-ion batteries can undergo over 1000 cycles and have a shelf life of 10 years (Aifantis et al., 2010).

1.2 Improving Li-ion battery performance using silicon anodes

The energy demand for portable electronic devices is ever increasing with the introduction of multifunctional high performance devices, such as mobile phones and tablets. Graphite is the traditional choice of anode material owing to its long cycle life, abundant material supply and relatively low cost. However, the graphite anode also exhibits a low theoretical

specific capacity of 372 mAh/g and is prone to catching fire when operated under the wrong conditions (Shukla & Prem Kumar, 2008). As such, investigation has been undertaken to develop new anode materials with significantly improved performance in terms of capacity, energy density and rate capability. An ideal material under consideration is silicon, which can accept over four times more Li-ions than graphite during lithiation, forming $Li_{22}Si_4$ at high temperature. This behaviour corresponds to the highest known theoretical specific capacity for Li-ion intercalation of 4200 mAh/g, over ten times higher than that of graphite (Szczech & Jin, 2011; Teki et al., 2009). Furthermore, silicon is an abundant, inexpensive, and sustainable material.

Clearly, the use of silicon as an anode material has huge potential to significantly improve battery capacity. However, this excellent capacity comes at the expense of a 310% volume expansion and contraction of the silicon anode during lithium insertion and extraction, compared to the 6-10% volume expansion observed for a graphite anode (Beaulieu et al., 2001, 2003; Benedek & Thackeray, 2002; Kasavajjula et al., 2007; Zhang, 2011). This change in volume results in significant detrimental effects that render the battery impractical for commercialization unless significant anode design changes are made. In terms of adverse affects, the anode experiences extremely high compressive stresses upon lithiation due to the restrained volume expansion, while large tensile stresses are induced due to the volume contraction upon delithation (Zhang, 2011). These stresses cause cracking and pulverization of the active particles, leading to disconnected charge transport paths which in turn cause incomplete intercalation, and as a result high irreversible capacity loss (Kim et al., 2005; Wachtler et al., 2002). Electrochemical aggregation of the active particles has also been observed due to the induced stress, which results in an increase in diffusion length and therefore a decrease in rate capability. This agglomeration of active particles can also trap the passivating solid-electrolyte interface (SEI) film within the anode structure and cause a loss of electronic contact and further irreversible capacity loss (Li et al., 2001). Furthermore, silicon is considered a semiconductor and as such has a low intrinsic conductivity. Therefore silicon anode structures typically exhibit poor rate performance due to slow electron transport within the anode material (Kim et al., 2005), which in turn reduces the energy capacity of the battery (Klankowski et al., 2013).

Therefore, in order to utilize silicon as a new anode material several important design requirements must be met. The anode structure must adequately accommodate the volume expansion upon lithiation, and reduce the associated induced mechanical stress. The design

must exhibit efficient charge transport paths and small Li-ion diffusion lengths to attain good rate capability. Experimental and numerical efforts have been undertaken by various authors to address this anode design problem. These works are reviewed in the following two sections, and motivate the structural optimization approach presented in this thesis.

1.3 Experimental efforts

Several methods have been adopted by experimentalists to improve the performance of Li-ion batteries using silicon anode structures. These techniques include reducing the active particle size to the nanometer range, and using porous structures, multiphase composites, thin film alloys, and nanowire anodes.

1.3.1 Nanoscale structures

Nanostructured anode configurations reduce the irreversible capacity loss because the active particles can accommodate the large stress and strain without cracking (Chan et al., 2008; Yang et al., 1996). This is a result of size-induced ductility where decreasing the grain size to the nanometer scale will dramatically increase the yield and fracture strengths (Meyers et al., 2006; Yip, 1998). The nanostructures can therefore sustain considerably greater stresses before pulverization. Furthermore, structures on the nanoscale have a significantly greater surface area to volume ratio compared to bulk active material. This results in improved Li-ion diffusivity due to smaller charge transport distances and therefore enhanced power capabilities (Aifantis et al., 2010; Scrosati & Garche, 2010). However, the enhanced surface area also increases the risk of secondary reactions involving electrolyte decomposition, such as the formation of a larger SEI film (Arico et al., 2005).

1.3.2 Porous structures

The large volume expansion upon lithiation may be accommodated by the voids in porous electrode structures, as shown by Shin et al. (2005) in Figure 1.2. Porous structures can show improved power density over microbattery structures that have thin film electrode layers. This is because the active material is exposed to the electrolyte in all three dimensions whilst maintaining small diffusion lengths. However, the large volume of pores will decrease the total volumetric energy density of the cell (Zhang, 2011).

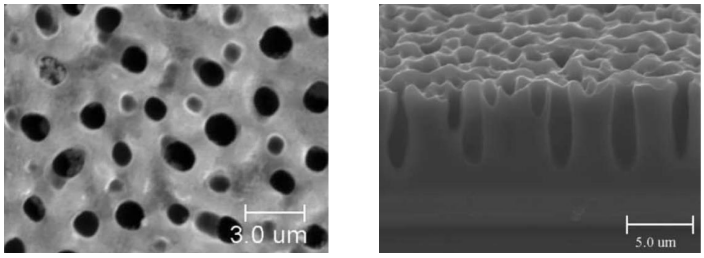

(a) Top view (b) Side view

Figure 1.2: Porous silicon structures produced by Shin et al. (2005). Reprinted from Shin et al. (2005), Copyright (2004), with permission from Elsevier.

1.3.3 Multiphase composites

In multiphase composites the active material is dispersed within a composite matrix, which allows the efficient transport of both electrons and Li-ions. The host matrix buffers the large volume change upon lithiation to maintain the structural integrity of the anode (Yang et al., 1996). Typically a thick SEI layer does not form as the matrix protects the surface of the active material (Aifantis et al., 2010). Furthermore, the host matrix has the added effect of reducing active particle aggregation during cycling (Yang et al., 1999). The matrix may be electrochemically inert such as Cu, Fe or TiN, or may react with Li at a different onset potential than the active material, such as SbSn (Zhang, 2011).

1.3.4 Thin-film anodes

Thin-film silicon anodes are of great interest for high performance Li-ion batteries. Silicon thin films have an amorphous structure which can better accommodate Li-ions than crystalline silicon due to the homogeneous expansion and contraction of the structure, thus achieving a large capacity (Aifantis et al., 2010; Ohara et al., 2004). The performance of thin-film anodes is highly dependent on the thickness of the film, deposition rate, deposition temperature, substrate-surface roughness and post annealing treatment (Liang et al., 2014; Takamura et al., 2006). Thinner films ($\leq 1\ \mu m$) exhibit superior performance due to decreased lithium diffusion length, resulting in fast charging and discharging rates, decreased electrical resistance and a lower state of stress upon lithiation (Liang et al., 2014; Notten et al., 2007). However, if the film is extremely thin the storage capacity will be too low to be commercially viable due to insufficient active material (Chan et al., 2008). Thin-film silicon anodes exhibit good cycling

performance, which may be attributed to the strong adhesion of the active material to the conductive substrate (Liang et al., 2014). Unfortunately a thick SEI layer may form on the surface of thin films during initial cycling which causes irreversible capacity loss (Baggetto et al., 2011).

Figure 1.3 depicts patterned thin-films produced by He et al. (2012). The gaps between the patterns allows stress relaxation, reduces cracking, and improves cycling stability in comparison to a continuous thin film.

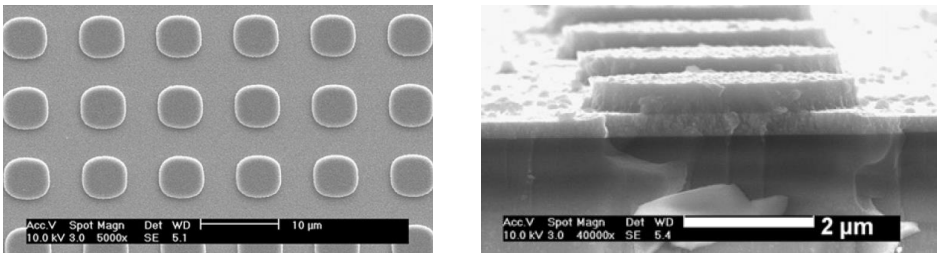

(a) Top view (b) Side view

Figure 1.3: Patterned thin films produced by He et al. (2012). Reprinted from He et al. (2012), Copyright (2012), with permission from Elsevier.

Figure 1.4 shows novel honeycomb-structured silicon films developed by Baggetto et al. (2011). These structures accommodate the volume change upon lithitaion by the lengthening and subsequent buckling of the honeycomb struts. Upon delithiation, the curved structures returned to their original shape with only slight permanent deformation.

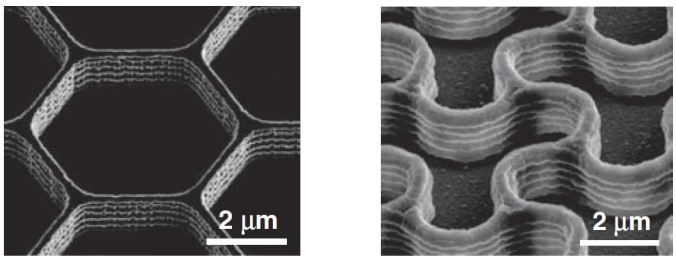

(a) Unlithiated structure (b) Lithiated structure

Figure 1.4: Honeycomb structured films produced by Baggetto et al. (2011). Reprinted from Baggetto et al. (2011), Copyright (2011), with permission from John Wiley and Sons.

Thin film anode structures have given promising results to date; however the deposition process is expensive and the current methods used are not yet suitable for large scale manufacture.

1.3.5 Nanowire anodes

Silicon nanowire (SiNW) anodes, depicted in Figure 1.5, show excellent promise as a high performance anode structure in a Li-ion battery. The SiNW structure can accommodate the large volume change upon lithiation without fracture or fragmentation. The large surface area to volume ratio results in short Li-ion diffusion distances and therefore high rate capability. The SiNWs also allow rapid charge transport through one-dimensional electronic pathways. Furthermore, these structures can be directly connected to a current collector without the need for binders or conducting additives, which eliminates redundant weight and allows each nanowire to contribute to the capacity (Chan et al., 2008; Liang et al., 2014). However, SiNWs are generally insulating and therefore require doping to make the wires conductive (Peng et al., 2008).

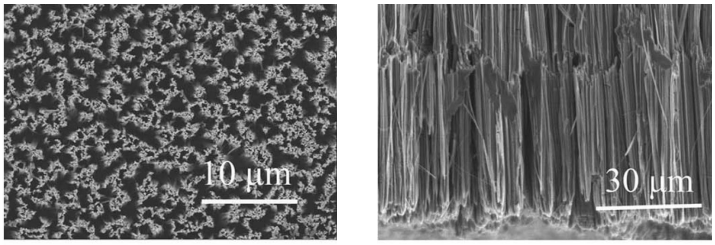

(a) Top view (b) Side view

Figure 1.5: Silicon nanowires produced by Huang et al. (2009). Reprinted with permission from Huang et al. (2009). Copyright (2009), AIP Publishing LLC.

1.3.6 Improving electrical conductivity

Improving the electrical conductivity of silicon anodes results in improved capacity retention and cycleability of the battery. One approach to improving the electrical conductivity is to coat the anode surface with conductive materials, such as carbon or copper, to provide an effective electronic pathway (Kim et al., 2005; Liu et al., 2005). The carbon shell also cushions and constrains the expansion of the silicon, minimizing pulverization and fracture. Furthermore, the thin-film layer of carbon can suppress the decomposition of the electrolytes modifying the SEI formation, which in turn results in a reduction of irreversible capacity (Yoshio et al., 2002). Doping is another method commonly used to improve the electrical conductivity of the silicon anode through the intentional introduction of impurities to vary the carrier concentration (Szczech & Jin, 2011).

1.4 Numerical modeling and simulation

In addition to experimental efforts, another area of investigation relating to the improvement of silicon anode structures is the numerical modelling and simulation of electrodes and the corresponding Li-ion battery system. These methods offer a crucial insight into battery behavior and performance, such as lithiation and diffusion processes, stress analysis, degradation phenomena, and cycling performance.

The vast majority of numerical models used to simulate electrochemical performance in Li-ion batteries are based on the porous electrode and concentrated solution theories proposed by Newman & Tiedemann (1975) and Doyle et al. (1993). Porous electrode models consider the electrodes to be a combination of solid and electrolyte phases characterised by the electrolyte volume fraction, also known as the porosity of the electrode. The model solves lithium diffusion dynamics and charge transfer kinetics to predict the electrical response of a cell in a paired intercalation electrode system. Porous electrode models have since been enhanced to account for various other phenomena and configurations, for example, capacity fade (Spotnitz, 2003), regular and random arrays of cathode particles (Wang & Sastry, 2007), and thermal effects (Kumaresan et al., 2008).

Several studies have focussed on particle scale numerical models in order to better understand the lithium insertion and extraction process within an electrode. Christensen & Newman (2006) presented a mathematical model that calculated the volume expansion, volume contraction, concentration, and stress profiles during lithium insertion and extraction from a spherical particle. Zhang et al. (2008) simulated intercalation induced stress and heat generation inside Li-ion battery cathode particles under potentiodynamic control, while Cheng & Verbrugge (2008) examined the effects of surface mechanics on diffusion induced stresses within spherical nanoparticles.

Lithiation processes have also been modelled for other electrode configurations. Deshpande et al. (2010) developed a mathematical model relating surface energy with diffusion-induced stresses in SiNW electrodes. The authors found that the electrode is less prone to mechanical degradation with decreasing nanowire radius. Bucci et al. (2014) conducted both numerical simulations and experimental measurements to characterize the mechanical and electrochemical response of thin film amorphous silicon anodes during lithiation.

Other studies have considered fracture mechanics and crack nucleation under diffusion

induced stresses for different electrode geometries, such as a bilayer plate (Huggins & Nix, 2000), a single particle electrode (Woodford et al., 2010), a strip electrode (Bhandakkar & Gao, 2010), and a cylindrical electrode (Bhandakkar & Gao, 2011).

Multi-scale battery cell models have been used to model the transport processes, electric potentials, and mechanical deformations across the battery cell. The micro-scale typically analyses a representative particle of the electrode, and homogenization methods are used to relate the macro- and micro-scales (Salvadori et al., 2014). Kim et al. (2011) developed a multi-scale multi-dimensional model framework to evaluate the design of stacked prismatic Li-ion battery cells. The authors investigated the impact of different cell stack aspect ratios as well as tab configurations and sizes. Golmon et al. (2012, 2014) presented a multi-scale numerical model in conjunction with a mathematical optimization scheme to maximize the battery capacity and limit electrode stress levels through the modification of the local porosities and particle radii of the electrodes.

1.5 Topology optimization

An alternative approach to addressing the silicon anode design problem is to utilize topology optimization methods. Topology optimization may be considered a fundamental design phase that typically precedes both experimental techniques and numerical modelling methods. However, topology optimization is underutilized in the field of silicon anode structures, where anode designs are typically crafted by experimentalists based on historical testing results, simulation performance, and design intuition. As such, the anode structures are not necessarily optimal from the outset, and there is huge potential to use this structural optimization method to produce silicon anodes with significantly enhanced performance. These optimal designs could subsequently be used in both experimental testing and battery simulation phases.

Structural optimization methods may be classified into three broad categories, namely sizing, shape, and topology optimization, depicted schematically in Figure 1.6. Both sizing and shape optimization methods are used to optimize design variables of predefined structural configurations. Sizing optimization involves optimizing specific dimensions of the structure, such as thickness, length, or cross-sectional area, whilst the geometry (shape) and topology of the design remain constant. The work presented by Golmon et al. (2012, 2014) in Section 1.4 is an example of sizing optimization. Shape optimization methods optimize the geometric

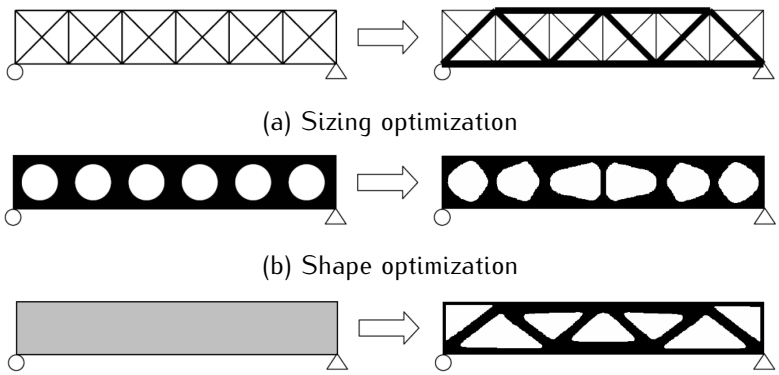

(a) Sizing optimization

(b) Shape optimization

(c) Topology optimization

Figure 1.6: The three categories of structural optimization. The initial design problems are shown on the left, while the optimal solutions are shown on the right. Republished with permission of Springer, from Bendsøe & Sigmund (2003); permission conveyed through Copyright Clearance Center, Inc.

features of the design, such as the shape of void spaces within a structure, yet the underlying topology of the design remains unchanged.

Topology optimization is the most generalized structural optimization method. Topology optimization is used to determine the optimal material distribution within a design domain for a given set of loading and boundary conditions. This method determines the boundary and connectivity of a structure, and the location and shape of voids for a given design problem. Because the optimum design is not based on a predefined structural configuration, the solution obtained by topology optimization is regarded as the true optimum in a design space for a specific problem. This method is an extremely useful tool for conceptual design stages, or for problems where there is limited physical intuition of the optimal structural design. Topology optimization methods are implemented through the use of finite element and optimization techniques, and typical design objectives include minimizing compliance, displacement, stress, resonant frequencies, and eigenvalues.

1.6 Research objective and thesis outline

To summarize, the Li-ion battery is a highly successful rechargeable battery that requires significant performance enhancement to meet the energy demands of today's portable electronic devices. One method to improve battery performance is to replace the traditional graphite anode with silicon, which has the highest known theoretical specific capacity for Li-ion in-

tercalation. However, upon lithiation the silicon anode structures undergo a 310% volume expansion, which causes severe damage, such as pulverization of the active particles and disconnected charge transport paths. These detrimental effects, in addition to the low intrinsic electric conductivity of silicon, renders these silicon anode Li-ion batteries impractical for commercialization unless significant design changes are made. The design requirements are that the silicon anode structure must adequately accommodate the volume expansion upon litihiation, and reduce the associated mechanical stress. The design must also maximize electrical conduction through the structure to compensate for the low conductivity of silicon and ensure good rate capability of the battery.

Experimentalists have endeavoured to address these design requirements by investigating a range of silicon structures, such as nanoscale structures, porous structures, composites, thin-films, and nanowire structures. Their methods involve manufacturing, testing, and iteratively refining designs chosen by intuition, and therefore from the outset these structures are not necessarily optimal. Additionally, numerical methods have been used to simulate the electrochemical performance of Li-ion battery systems. However, these models primarily use porous electrode theory and focus on particle scale analysis, with little interest in novel architectures or silicon anodes. Furthermore, numerical methods focus on analysing the performance of a chosen battery configuration; therefore, these structures are also not necessarily optimal from the outset.

Our research objective is to use topology optimization methods to determine optimal multifunctional silicon anode structures for Li-ion battery applications. Topology optimization is the most general form of structural optimization, which is used to determine the optimal distribution of material within a design domain for a given set of loading and boundary conditions. The designs obtained by topology optimization methods are regarded as the true optimum in a design space for a specific problem, and therefore unlike the experimental and numerical efforts, this novel approach to the silicon anode design problem will produce structures that are optimal from inception. We aim to develop optimal anode designs that address the structural problems associated with the large volume expansion upon lithiation, and also the low intrinsic electronic conductivity of the anode material. The design requirements are first considered individually, then subsequently addressed simultaneously to produce multifunctional silicon anode designs. These designs will provide a solid foundation for the informed design and development of silicon anode structures, and may subsequently be used by experimentalists

for testing, and may also be incorporated into numerical models of Li-ion battery systems.

This thesis is structured as follows. In Chapter 2 we present a literature review that surveys the previous topology optimization work relevant to this thesis. Chapter 3 details the topology optimization methodology and algorithm structure. We then present topology optimization analysis and results for the design objective of minimum compliance under design dependent volume expansion in Chapter 4, and subsequently for the design objective of maximum electrical conduction in Chapter 5. In Chapter 6 we analyse a multi-objective topology optimization problem that simultaneously addresses both compliance and conduction criteria. Finally, in Chapter 7 we present a summary and outline avenues for future investigation.

Chapter 2

Literature Review of Topology Optimization Methods

This chapter provides a literature review of the current topology optimization methods and applications that are relevant to this body of work. A brief introduction outlining the origins and prevailing methods of topology optimization is followed by specific areas of interest, including thermoelastic topology optimization, heat and electric conduction, material design, multi-objective problem formulations, and work relating to fuel cell applications.

2.1 Origins and prevailing methods

Topology optimization was first introduced in the seminal work by Bendsøe & Kikuchi (1988). The authors presented a microstructure or homogenization based structural optimization method that models porous structures, where the material in each element is composed of both solid material and voids. Homogenization theory is then used to determine the effective macro-scale properties of the periodic microstructure. The aim of the topology optimization problem is to determine the microstructure layout that corresponds to the optimal macro-scale distribution of material properties, such that an objective function is minimized or maximized. This method is capable of providing bounds on the theoretical performance of composite structures. However, a disadvantage of the homogenization method is that the evaluation of the optimal microstructures is cumbersome due to the large number of design variables. Furthermore, no definite length scale is associated with the microstructures, resulting in complications for practical applications.

Since the introduction of the homogenization method, topology optimization has been a

very active area of research with the development of a range of robust and efficient methods. Density-based methods are the most widely used topology optimization methodology. As with the homogenization method, the domain is discretized into finite elements. However, with density methods each element is assigned a design variable that is the density of material, rather than a set of microstructure properties. The aim is to obtain an optimized structure that consists of a macroscopic variation of a solid material and void such that the density may be expressed by a 1-0 integer parametrization. To avoid numerical difficulties, density methods utilize continuous design variables. The intermediate densities are then penalized through an interpolation scheme, such as the Solid Isotropic Material with Penalization (SIMP) (Bendsøe, 1989; Zhou & Rozvany, 1991), which steers the solution to the desired solid-void design. An objective function such as compliance is minimized, in conjunction with imposed constraints such as a limit on the volume of material in the final design.

Alternate topology optimization approaches include the Evolutionary Structural Optimization (ESO) method and the level set approach. Originally developed by Xie & Steven (1993), the ESO method identifies unnecessary or inefficient portions of a structure and subsequently eliminates them from the finite element model. Querin et al. (2000) later introduced an additive algorithm named the Bi-directional Evolutionary Structural Optimization (BESO) which is capable of both the removal and reintroduction of material in the structure. Unlike density methods, ESO and BESO do not relax the discrete density variables to a continuous formulation. As such, these methods produce optimal structures with well-defined structural boundaries without the need for post processing. However, the addition or removal of material is based on heuristic criteria, which may not be based on sensitivities. Therefore there exists no rigorous proof that this methods yields an optimal solution (Rozvany, 2009).

The level set method is a boundary variation method that was first applied to topology optimization by Sethian & Wiegmann (2000). The level set method is based on an implicit function that defines the structural boundaries, as opposed to an explicit parameterization of the design domain using element densities. This method produces structures with distinct boundaries; however, the optimal designs are highly dependent on the initial design. Furthermore, reinitialization is required when the level set functions become too flat or too steep, thereby reducing computational efficiency (Deaton & Grandhi, 2014).

2.2 Thermoelastic topology optimization

Thermoelastic topology optimization problems involve both mechanical and thermal loading, where the thermal load is inherently design dependent. Design dependent loading relates to loads that are a function of element density, and as such vary with each iteration as the design evolves towards the optimum solution. The design dependent variable for thermal loading is the coefficient of thermal expansion. The change in temperature of the structure may be uniform (design independent), or as an added complication the temperature change may also be design dependent.

Early thermoelastic topology optimization work by Rodrigues & Fernandes (1995) utilized the homogenization method to minimize the compliance of thermally loaded structures subject to an isoperimetric constraint on volume. The authors considered a bi-clamped beam subject to both mechanical loading and a uniform temperature change. This problem has been extensively studied by numerous authors and is now considered a thermoelastic benchmark problem, much like the Messerschmidt-Bölkow-Blohm (MBB) beam for minimum compliance problems under pure mechanical loading (Olhoff et al., 1991).

The minimum compliance objective has frequently been adopted for thermoelastic structural topology optimization. This objective minimizes a global measure of displacement and therefore generates a structure resistant to expansion, or maximizes the stiffness of the structure. Xia & Wang (2008) performed minimum compliance topology optimization of thermoelastic structures using a level set method. Gao & Zhang (2010) studied the effects of different material interpolation schemes using the minimum compliance benchmark problem by Rodrigues & Fernandes (1995). Additionally, Gao & Zhang (2010) introduced the concept of penalizing a thermal stress coefficient (TSC) to effectively interpolate the design dependent thermal loading. Pedersen & Pedersen (2012) also investigated the influence of interpolation on thermoelastic topology optimization problems. Yan et al. (2008) proposed concurrent optimization of both the macro and microstructure to minimize the structural compliance under combined mechanical and thermal loads. The optimizations at the two scales are integrated into one system using homogenization theory. Jog (1996) explored non-linear thermoelastic topology optimization problems using the perimeter method and a compliance objective. Furthermore, Li et al. (1999b) used the ESO method to minimize the displacement of several thermoelastic structures, including the bi-clamped beam problem introduced by Rodrigues & Fernandes

(1995).

Most of the above work considers combined mechanical and thermal loading. Typically, the thermal loads are relatively low such that the mechanical loads dominate throughout the optimization process. However, when there are no mechanical loads or if thermal loads dominate, numerical difficulties may arise. Deaton & Grandhi (2013a) investigated stiffening and stress reduction in thermal structures subject to restrained thermal expansion. The authors considered multiple formulations, including minimum compliance using a thermal load and an upper limit on volume fraction. This problem formulation failed to yield suitable results, with the structure achieving zero density throughout the domain. In structural design, a reduction in stress and deformation of mechanically loaded structures may be achieved by the strategic addition of material to increase the stiffness of the structure. However, when the structure is subjected to a positive temperature change, the addition of material will increase the thermal loads, which may lead to greater deformation and stresses. Therefore, for problems where thermal loads dominate, the minimum compliance objective will drive the solution to the lower limit of material volume. If no lower limit is set, the solution becomes singular (zero density throughout the domain). One solution is to prescribe both an upper and lower bound on volume, or an equality constraint (Bruyneel & Duysinx, 2005).

For design independent or pure mechanical loading, the optimal design for minimum compliance is the same as the optimal design for maximum strength (Kohn & Wirth, 2014; Pedersen & Pedersen, 2012). However, for strength optimized thermoelastic problems, Pedersen & Pedersen (2010a, 2012) questioned the validity of the minimum compliance formulation with only an upper bound on material volume. This is due to the inactive volume constraint and the competing nature of compliance and strength objectives which drive the design to opposite material volumes. In order to ensure the upper volume constraint remains active and avoid the need to treat the volume as a further design parameter, the authors suggest performing strength optimization using a uniform energy density objective.

Optimizing for strength directly poses a significant challenge compared with other objectives that use measures on the global level, such as compliance or uniform energy density. The three primary difficulties are the singularity phenomenon, the local nature of stress constraints, and the highly non-linear stress behaviour (Bendsøe & Sigmund, 2003). Deaton & Grandhi (2013b) expanded on their previous work by investigating stress-based design criteria for structures subject to thermoelastic loading. Specifically, they considered objective of mass

minimization subject to a constraint on stress. In practical terms, this relates to finding the lightest structure that does not fail. For the case of an anode in a battery where a particular volume of material is specified in order to achieve the required energy density, the objective of mass minimization with stress constraints becomes less relevant. Furthermore, for a specific volume, compliance minimization is deemed to reflect the minimum stress objective adequately. As such, this research focuses on objectives that are global in nature only, and the author refers the reader to Le et al. (2010) and Lee et al. (2012) for further details on stress-based topology optimization.

2.3 Heat conduction and electromagnetics

Topology optimization with the objective of maximizing heat conduction produces structures that effectively dissipate or transmit heat generated by a source. This design problem has been explored for a range of applications by various authors. Haslinger et al. (2002) used the homogenization method to optimize isotropic bi-material conducting structures. Gersborg-Hansen et al. (2006) compared heat conduction topology optimization results modelled by the finite element method and the finite volume method. Dede (2009) utilized COMSOL Multiphysics software and a method of moving asymptotes optimizer to investigate a benchmark heat conduction problem involving internal heat generation and a heat sink, resulting in an optimal 'branching' structure. The author then extended the analysis to a three-terminal heat transfer and fluid flow device. Takezawa et al. (2014) considered topology optimization of a mechanical structure that minimized material volume under both strength and thermal conductivity constraints.

One particular area of interest has been that of multiple heat load cases, where a number of heat sources act on the structure at different times, locations, and with different heat boundary conditions. Li et al. (1999) investigated shape and topology design for steady-state heat conduction problems using the ESO method for both single and multiple heat load cases. Zhuang et al. (2007) used a level set method to explore steady-state heat conduction problems subject to multiple heat load cases with the design objective of constructing an effective transport path for heat dissipation under a given volume constraint.

Design dependent heat loads, or heat loads that depend on the material distribution, have been a recent topic of investigation. Gao et al. (2008) used BESO method to explore steady-

state heat conduction under both design independent and design dependent heat loads. Iga et al. (2009) considered a total potential energy objective to determine optimally conducting structures subject to design dependent boundary conditions of heat convection and internal heat generation.

Heat conduction and electricity play a role in compliant mechanism topology optimization, where the mechanism relies on the device's own elastic deformation to transfer a motion or force. Sigmund (2001a,b) used topology optimization to design thermally and electrothermally driven micro actuators for use in microelectromechanical systems (MEMS). In these systems an electrical current is converted to heat, which causes thermal strain, which then causes structural deformation. The author considered the design objective of maximizing the deformation of a workpiece subject to the electrical, thermal and elastic equilibrium equations, and constraints on material volume, electrical current, and out of plane displacement . Yin & Ananthasuresh (2002) presented a design parameterization scheme for topology optimization of MEMS made of multiple materials, and also explored design dependent boundary conditions, namely heat convection from the device surfaces. Li et al. (2004) designed thermally actuated compliant mechanisms that consider the time-transient effect of heat transfer to produce the localized thermal actuation.

Topology optimization has also been utilized for electromagnetic applications. de Lima et al. (2007) and Mello et al. (2008) performed topology optimization to obtain conductivity image distributions in electrical impedance tomography (EIT), where EIT is an imaging method that estimates the conductivity distribution within a body given measured voltages on electrodes attached to the body. Petrova (2010) performed topology optimization of electromagnetic media described by the eddy current equations to determine the optimal design of conductive devices that minimized the energy dissipation. Zhou et al. (2010b) presented a level-set framework that optimized the structure of a dipole antenna, with the design objective of more effectively receiving and reflecting electromagnetic signals formulated in terms of the surface current and incident electric field. Nomura et al. (2007) investigated the optimization of dielectric resonator antennas to achieve enhanced bandwidths using topology optimization methods in conjunction with the finite difference time domain method.

2.4 Material optimization

Material optimization methods such as the inverse homogenization method are used to design material structures with improved properties. Recall that homogenization methods involve determining the effective macroscale properties of a composite porous material from the homogenized, or averaged, properties of a periodic microstructure defined within a unit cell (Hassani & Hinton, 1998a,b,c). In contrast, the inverse homogenization method proposed by Sigmund (1994) aims to find the microstructure of a material with desired macroscale physical properties. The design problem is formulated as a minimization of the difference between the homogenized material properties and the target material properties within a representative volume element. The inverse homogenization method has been used for various applications, including achieving tailored thermal conductivity (Patil et al., 2008; Zhou & Li, 2008a,b), maximum fluid permeability (Guest & Prévost, 2007), generalized transport properties (Zhou et al., 2012), phononic/photonic bandgap materials (Halkjær et al., 2006; Sigmund & Jensen, 2003), negative Poisson's ratios (Andreassen et al., 2014; Chen et al., 2001; Sigmund, 1994), and functionally graded materials whose material properties vary gradually in one or more specified directions (Paulino et al., 2009; Zhou & Li, 2008c).

When performing material design using the inverse homogenization method, the two material phases of the optimal structure are sometimes separated by a constant mean curvature (CMC) surface. A CMC surface is one that has a mean curvature equal to an arbitrary constant at every point (Zhou & Li, 2007). A minimal surface is a special case of the CMC surface where the mean curvature is equal to zero, such as a soap bubble or the triply-periodic Schwarz primitive (P) minimal surface (Schwarz, 1890) depicted in Figure 2.1.

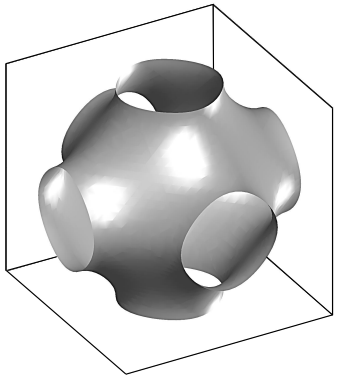

Figure 2.1: Unit cell of the triply-periodic Schwarz P minimal surface.

A Schwarz P-type structure is commonly obtained if the volume fractions of both material phases are equal, while a CMC surface separates phases of unequal volumes. Zhou & Li (2008a) obtained a Schwarz P-type structure for the objective of maximizing thermal conductivity, as shown in Figure 2.2. The plotted elements depict the highly conductive material phase, while the void space represents the poorly conductive material phase. Guest & Prévost (2007) produced the same design for a maximum fluid permeability objective, where the solid phase is represented by the structure depicted in Figure 2.2, and the fluid phase represented by the internal void space.

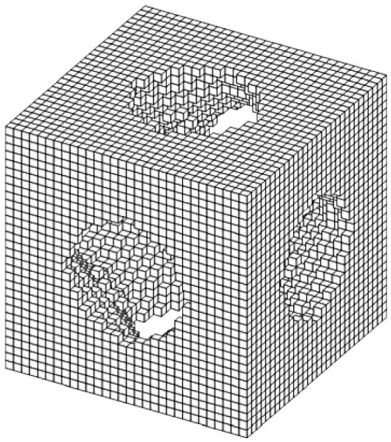

Figure 2.2: Schwarz P-type structure showing the highly conductive material phase for the objective of maximum thermal conductivity. Reprinted with permission from Zhou & Li (2008a). Copyright (2008), Taylor & Francis.

There has been significant interest in using the inverse homogenization method to obtain structures with maximum stiffness or minimum compliance. The first instance of designing 2D periodic microstructures for minimum compliance using this method was by Sigmund (1994), who minimized the weight of the base cell subject to a target constitutive elasticity tensor. Neves et al. (2000) considered a maximum bulk modulus objective, and attained structures similar to those designed by Sigmund (1994). The bulk modulus measures the elastic resistance of a material to hydrostatic compression or expansion, thus maximizing the bulk modulus effectively maximizes the stiffness of the structure. Sigmund (2000) studied two-phase extremal composites that incorporated layered sub-microstructures while Gibiansky & Sigmund (2000) maximized the bulk modulus of isotropic elastic composites composed of three or more constituent phases. Zhang et al. (2007) proposed an alternative strain energy method for the

prediction of effective elastic properties of cellular periodic materials. Their results are in agreement with those obtained by the above authors for the objective of maximum bulk modulus. Huang et al. (2011) designed 2D and 3D periodic microstructures with maximum bulk or shear modulus under a prescribed volume constraint using the BESO method. Their 3D results for a two-phase material consisting of solid and void for prescribed volume fractions of 30% and 50% are given in Figure 2.3. These structures also show some resemblance to CMC surfaces.

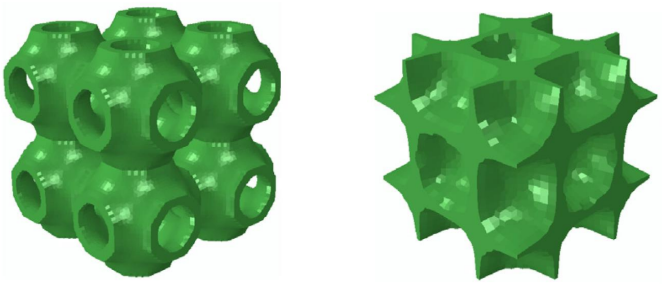

(a) $V_f = 0.30$ (b) $V_f = 0.50$

Figure 2.3: Results for a maximum bulk modulus objective function subject to a constraint on volume. Reprinted from Huang et al. (2011), Copyright (2011), with permission from Elsevier.

Sigmund & Torquato (1996, 1997, 1998) investigated the design of three phase isotropic composites with extreme coefficients of thermal expansion using the inverse homogenization method. The composites were comprised of two material phases and a void phase. The authors considered objectives such as maximum directional thermal expansion for the application of thermal actuators, zero isotropic thermal expansion, and negative isotropic thermal expansion, subject to constraints such as elastic symmetry or volume fractions of the constituent phases.

2.5 Multiobjective topology optimization

Engineering design problems typically involve simultaneously optimizing several conflicting and possibly non-commensurable (measured in different units) design criteria by which the performance of the system is measured, such as compliance, heat conduction, electrical conduction, displacement, or stress. This section reviews the recent multiobjective topology optimization efforts that are relevant to this thesis.

2.5.1 Compliance and heat conduction

The bi-objective formulation of minimizing compliance and maximizing heat conduction is of particular relevance to this body of work. Chen et al. (2010) developed a topology optimization algorithm for multifunctional 3D finite periodic structures, simultaneously addressing the maximum stiffness and maximum heat conductivity criteria using a weighted average method. This optimization problem is further investigated in Chapter 6.2 for algorithm validation purposes. In other works, Liang et al. (2010) presented a multi-objective topology optimization of 2D steady-state diffusion flow problems based on finite volume analysis with specific emphasis on heat conduction. Suresh (2010) developed an algorithm to trace the Pareto frontier of multi-objective topology optimization problems involving a minimum compliance objective, based on the concept of topological sensitivity.

de Kruijf et al. (2007) performed topology optimization with design objectives of maximum stiffness and minimum resistance to heat dissipation for the structural design of a two-dimensional plate. The authors also performed two-dimensional material design using inverse homogenization methods to tailor ill-ordered two-phase composites with effective thermal conductivity and bulk modulus attaining their upper theoretical bounds.

Challis et al. (2008) utilized the level set topology optimization method to design three-dimensional isotropic periodic multifunctional composites. The objective was to maximize a linear combination of the effective bulk modulus and conductivity of a composite structure. The authors considered a two-phase ill-ordered composite, where one phase is stiff and insulating while the other is mechanically compliant and conductive, resulting in optimal structures similar to Schwarz surfaces.

In related work, Guest & Prévost (2006) investigated the optimization problem of maximum stiffness and maximum fluid permeability. They also obtained Schwarz P-type optimal structures. Chen et al. (2009) and Torquato & Donev (2004) claim that Schwarz-type microstructures are obtained when combining objectives of maximum stiffness and any transport property using material optimization methods such as inverse homogenization.

2.5.2 Compliance and thermal expansion

Minimum compliance has also been combined with the objective of minimizing the expansion of thermally loaded structures. Wang et al. (2011) performed three-phase topology optimization

of a space camera supporting structure that is subject to a large thermal gradient. The authors used a bi-objective formulation to determine the optimum structure for maximum stiffness under a given mechanical load and minimum thermal expansion in a predefined direction. Deng et al. (2013) performed concurrent topology optimization of both the macro and microstructure of lightweight thermoelastic structures. In this work the authors considered the objectives of minimizing structural compliance under mechanical loading, and minimizing the thermal expansion of specific surfaces under thermal loading.

2.5.3 Heat conduction and electric conduction

Torquato et al. (2002) obtained Schwarz P-type structures when optimizing multifunctional ill-ordered two-phase composite microstructures for simultaneous transport of heat and electricity. Figure 2.4 shows the design produced by Torquato et al. (2002) for combined maximum heat and maximum electricity objectives. The authors considered two material phases in equal proportions where one phase (shown in red) is a good thermal conductor but poor electrical conductor while the other phase (shown in green) is a poor thermal conductor but a good electrical conductor. Torquato et al. (2003) showed the optimality of the Schwarz structures for this bi-objective formulation using finite element calculations and rigorous cross-property bounds.

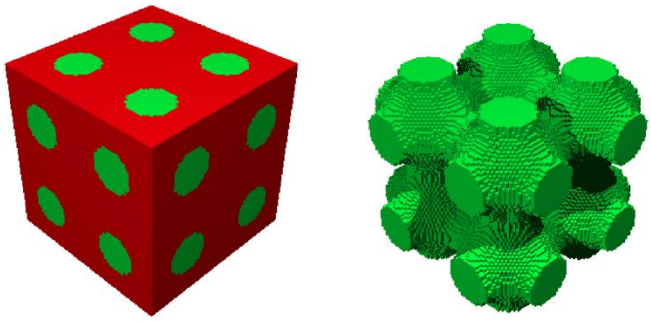

Figure 2.4: Optimized microstructure for simultaneous transport of heat and electricity. The red material phase is a good thermal conductor but poor electrical conductor while the green phase is a poor thermal conductor but a good electrical conductor. Reprinted figure with permission from Torquato et al. (2002), Copyright (2002) by the American Physical Society, http://dx.doi.org/10.1103/PhysRevLett.89.266601.

2.5.4 Electrical permittivity and magnetic permeability

Huang et al. (2012) utilized the BESO method to design ill-ordered two-phase periodic microstructures with extremal electrical permittivity and magnetic permeability. The effective permittivity and permeability were homogenized within the periodic base cell, and these electromagnetic properties maximized subject to a constraint on volume fraction. The optimal structures resemble Schwarz P surfaces similar to Figure 2.4. For this particular problem, the red phase of Figure 2.4 would represent the low permeability, high permittivity material.

Zhou et al. (2010a) obtained similar results using the inverse homogenization procedure to simultaneously maximize the permittivity and permeability of 3D metamaterial microstructures. Zhou et al. (2010a) also designed anisotropic composites with high permittivity in one direction, as shown in Figure 2.5. The optimal structures were cylindrical in shape, spanning the length of the domain parallel to the direction of maximal permittivity. The cylindrical cross-sections were not necessarily square-symmetric, depending on the permittivity of the other two principal directions.

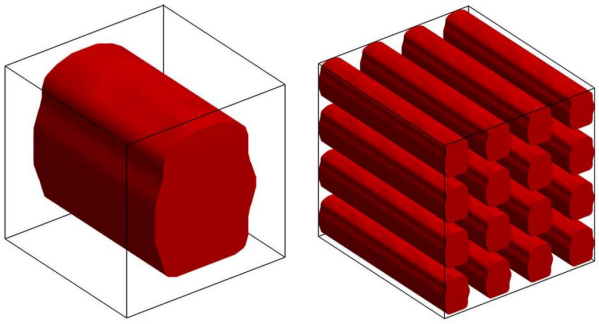

Figure 2.5: Optimal microstructure of a composite with anisotropic permittivity. The optimal base cell (*left*), and 4 x 4 x 4 base cells with the high permittivity material only (*right*) for a $V_f = 0.5120$. Reprinted with permission from Zhou et al. (2010a), Copyright (2010), IEEE.

2.6 Solid oxide fuel cells

There have been no instances of topology optimization methods being applied to the silicon anode design problem. In fact, topology optimization methods have been completely underutilized for battery systems in general. Several authors have applied structural optimization methods to solid oxide fuel cells (SOFCs), an entirely different electrochemical energy storage system. These works focused on the shape optimization, rather than topology optimization, of

cathodes or gas channels in SOFCs, typically performing only two-dimensional analysis.

Iwai et al. (2011) performed two-dimensional shape optimization using the level set method to determine the optimal cathode-electrolyte interface shape in SOFCs. The authors considered the objective function of maximum current density for a given terminal voltage. This level set method was coupled with a SOFC simulation to examine how interface modification affected the cell's power density. It was found that a larger interface area improved the current density of the cell.

Song et al. (2013) also performed shape optimization using topology optimization methods in order to identify the optimal shape of a nano-composite cathode in a SOFC that minimized the cathode's resistance to current. The authors considered a periodic, two-dimensional conduction problem with design dependent ionic transfer boundary conditions and isoperimetric constraints on the material volume and perimeter. Song et al. (2013) subsequently used topology optimization methods to design the shape of an air supply channel in an SOFC in order to maximize the current generation by the cathode.

Kim & Sun (2012) presented a two-dimensional density-based topology optimization formulation for fluid flow to determine the optimum route for gas flow channels in the bipolar plate of a fuel cell. An objective of the maximum mean reaction rate between the gas and an oxidant flowing through the channel was considered, with constraints of a specified pressure drop between the inlet and outlet in the design domain.

Zadin et al. (2013) utilized the level set method to design power-optimized microbattery geometries. The optimization problem considered a $LiCoO_2$ cathode and a LiC_6 anode separated by a polymer electrolyte, with the objective of maximizing the uniform electrochemical activity over the electrode surface area.

Chapter 3

Methodology

This chapter details the methodology and techniques implemented in our custom three-dimensional topology optimization code that was developed using the programming language MATLAB. First, the problem formulation of minimum compliance is presented as an illustrative example. Density methods and interpolation schemes are discussed, and a detailed review of the algorithm structure is provided, including the initialization and finite element stages, regularization and continuation schemes, mathematical programming methods, and post processing techniques.

3.1 Problem formulation

A general inequality-constrained nonlinear programming problem may be written in the following form

$$\begin{aligned} \text{minimize}: \quad & f_0(\mathbf{x}) \\ \text{subject to}: \quad & f_i(\mathbf{x}) \leq 0, \quad i = 1, \ldots, m \\ & x_j^{min} \leq x_j \leq x_j^{max}, \quad j = 1, \ldots, n, \end{aligned} \tag{3.1}$$

where f_0 is the given objective function and f_i are the constraint functions, all of which are typically twice continuously differentiable, real-valued function. $\mathbf{x} = (x_1, \ldots, x_n)^\mathsf{T} \in \mathbb{R}^n$ is the vector of design variables, and x_j^{min} and x_j^{max} are lower and upper bounds on the design variable, respectively.

An illustrative example used throughout this chapter is the topology optimization problem of minimum compliance for an isotropic linearly elastic structure subject to a constraint

on material volume. This problem formulation is a common choice for topology optimization applications due to its stability and ease of implementation, and builds the foundation for all analyses presented in future chapters. Let us consider a reference domain Ω, where displacements u are applied on a part of the boundary Γ_u, boundary tractions t are prescribed on Γ_t, and body forces b are also considered, as shown in Figure 3.1.

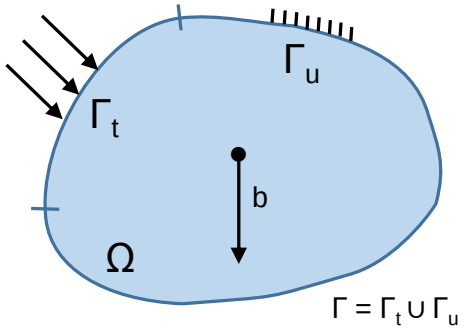

Figure 3.1: The reference domain with prescribed displacement, tractions, and body forces.

The minimum compliance objective may be defined as a minimization of force multiplied by displacement, over admissible designs and displacement fields satisfying equilibrium. The energy bilinear form is given by

$$a(u,v) = \int_\Omega \mathbf{C}_{ijkl}(x)\epsilon_{ij}(u)\epsilon_{kl}(v)\ d\Omega, \tag{3.2}$$

which represents the internal virtual work of an elastic body at the equilibrium u and for an arbitrary virtual displacement v (Bendsøe & Sigmund, 2003). With linearized strains

$$\epsilon_{ij}(u) = \frac{1}{2}\left(\frac{\partial u_i}{\partial x_j} + \frac{\partial u_j}{\partial x_i}\right). \tag{3.3}$$

Introducing the load linear form,

$$l(u) = \int_\Omega bu\ d\Omega + \int_{\Gamma_t} tu\ ds, \tag{3.4}$$

the minimum compliance problem is given by (Bendsøe, 1995; Bendsøe & Sigmund, 1999)

$$\begin{aligned} \min_{u \in U, \rho} : \quad & l(u) \\ \text{subject to} : \quad & a_\rho(u, v) = l(v), \quad \text{for all } v \in U, \\ & \int_\Omega \rho(x)\, d\Omega \leq V, \\ & \rho(x) \in \{0, 1\}. \end{aligned} \tag{3.5}$$

The equilibrium equation is written in its weak, variational form. U denotes the space of kinematically admissible displacement fields, x is a point within the domain Ω, $\rho(x)$ is the pointwise volume fraction, and V is the material volume. Using a finite element discretization for linear elasticity, the minimum compliance objective may be expressed as

$$\begin{aligned} \min_{x} : \quad & c(\mathbf{x}) = \mathbf{U}(\mathbf{x})^{\mathsf{T}} \mathbf{K}(\mathbf{x}) \mathbf{U}(\mathbf{x}) = \mathbf{F}^T \mathbf{U}(\mathbf{x}) \\ \text{subject to} : \quad & \mathbf{K}(\mathbf{x})\mathbf{U}(\mathbf{x}) = \mathbf{F}, \\ & \frac{V(\mathbf{x})}{V_0} \leq V_f^{max}, \\ & \mathbf{0} \leq \mathbf{x} \leq \mathbf{1}, \end{aligned} \tag{3.6}$$

where $\mathbf{x}$ is the vector of element densities, $c(\mathbf{x})$ is the compliance, $\mathbf{U}(\mathbf{x})$ is the global displacement vector, $\mathbf{K}(\mathbf{x})$ is the global stiffness matrix, $\mathbf{F}$ is the global force vector, $V(\mathbf{x}) = \sum_{e=1}^{N} x_e v_e$ is the material volume, V_0 is the design domain volume, and V_f^{max} is the prescribed volume fraction. This objective minimizes a global measure of displacement and therefore generates a structure resistant to expansion, or maximizes the stiffness of the structure (Penzler et al., 2012). For design independent loads, the compliance is equal to the total elastic energy (twice the elastic strain energy), which is the potential energy stored in a structure by elastic deformation, and also is equal to work that must be done to produce this deformation (Bendsøe & Sigmund, 2003). Furthermore, strain energy measures the stress state of the structure, to some extent (Zhang et al., 2014). If the structure deforms in a stress free state, the strain energy tends to be zero. With design independent loads and a constrained volume, the optimal design for minimum compliance is the same as that for maximum strength (Kohn & Wirth, 2014; Li et al., 1999a; Pedersen & Pedersen, 2012).

3.2 Density methods

Density-based methods are used to the solve optimization problems detailed in this thesis. In this approach, each finite element is assigned a continuous design variable x_e, representing the material density where $0 \leq x_e \leq 1$. Here, the values 1 and 0 represent an element that consists entirely of material phase a or b, respectively. Despite requiring a discrete valued or "$a-b$" final design, discrete optimization problems are often ill-posed and often cannot be solved for large scale problems. Therefore, in order to utilize derivative based mathematical programming algorithms, this continuous design variable is employed, and interpolation schemes are then used to penalize intermediate densities and steer the design to the desired discrete solution. Material properties such as the Young's modulus and diffusivity are functions of the continuous element density. For example, for the minimum compliance formulation the element material stiffness E_e may be interpolated as follows for the case of two material phases

$$E_e(x_e) = E^{(b)} + \Gamma(x_e)(E^{(a)} - E^{(b)}), \qquad x_e \in [0,1], \tag{3.7}$$

where $E^{(a)}$ and $E^{(b)}$ are the Young's Moduli of the two material phases, and $\Gamma(x_e)$ is the interpolation function. $\Gamma(x_e)$ satisfies the following relations

$$\begin{aligned} \Gamma(1) &= 1, \\ \Gamma(0) &= 0, \end{aligned} \tag{3.8}$$

such that

$$\begin{aligned} E_e(1) &= E^{(a)}, \\ E_e(0) &= E^{(b)}. \end{aligned} \tag{3.9}$$

In classical topology optimization problems, materials a and b are solid and void, respectively. This is a special case of the above formulation where the void material has zero stiffness, but is implemented as a very small number to prevent singularities in the finite element formulation, i.e., $E^{(b)} \approx 0$. Common interpolation schemes include the Solid Isotropic Material with Penalization (SIMP), and the Rational Approximation of Material Properties (RAMP) scheme, each of which will be detailed below.

3.2.1 SIMP interpolation scheme

The SIMP interpolation scheme (Bendsøe, 1989; Zhou & Rozvany, 1991), also called the power-law approach, is a simple yet efficient interpolation method where

$$\Gamma(x_e) = x_e^p. \tag{3.10}$$

p is the penalization parameter, typically set to a value of $p \geq 3$. Figure 3.2a shows the SIMP interpolation function as a function of density for element e. For $p = 1$ there is a linear relationship, while a further increase in the penalty parameter causes elements with intermediate densities to have a disproportionally low interpolation function value relative to the volume of material in that element. With the objective of maximizing stiffness of the structure, it is therefore inefficient for the optimization algorithm to choose intermediate density values.

Despite the non-physical nature of continuous formulations, Bendsøe & Sigmund (1999) have shown that this approach falls within the framework of microstructure models. The authors introduced bounds on the penalty parameter based on the Hashin-Shtrikman bounds for two-phase materials (solid and void), which allowed the material stiffness of an element to be interpreted as the stiffness of a composite structure consisting of the two material phases. Bendsøe & Sigmund (1999) also claimed that a better computational scheme may be obtained if the penalization parameter was increased beyond these allowable bounds. The authors justified that the physical meaning of solutions from iterations prior to the final solution, which may include intermediate densities, can be ignored providing a discrete solution is obtained. Other authors, such as Bruns (2005), Le et al. (2010), and Yin & Ananthasuresh (2001) are in agreement with this statement.

3.2.2 RAMP interpolation scheme

An alternate interpolation scheme is the RAMP scheme introduced by Stolpe & Svanberg (2001a)

$$\Gamma(x_e) = \frac{x_e}{1 + p(1 - x_e)}, \tag{3.11}$$

where p is the penalty factor, which typically takes a value of $p = 1 - 8$. This scheme is depicted in Figure 3.2. Unlike the SIMP method, the RAMP interpolation scheme ensures a

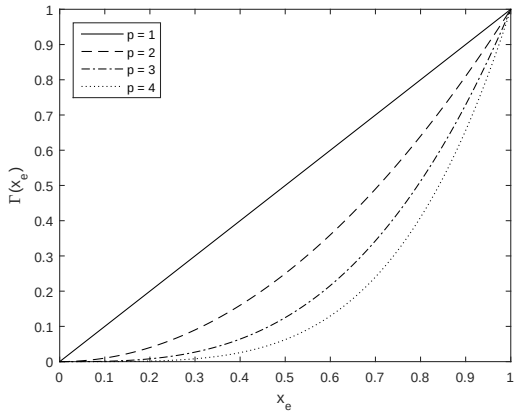

(a) SIMP: $\Gamma(x_e) = x_e^p$

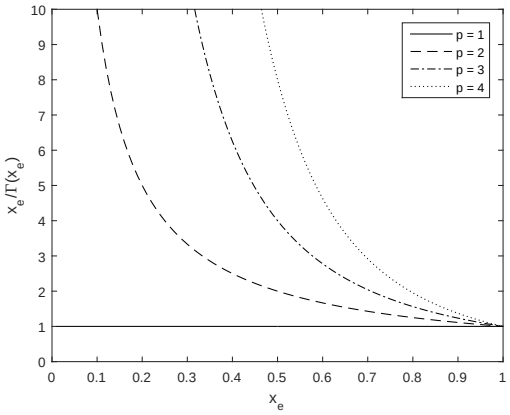

(b) SIMP: Density to $\Gamma(x_e)$ ratio

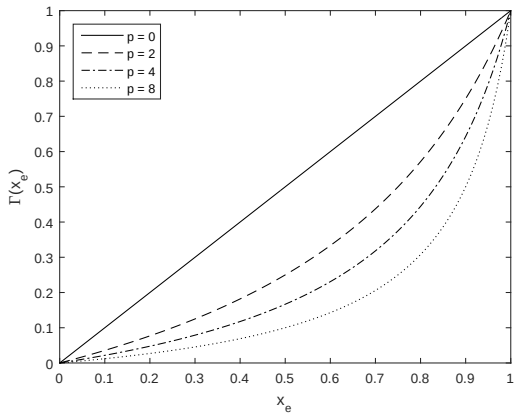

(c) RAMP: $\Gamma(x_e) = \frac{x_e}{1+p(1-x_e)}$

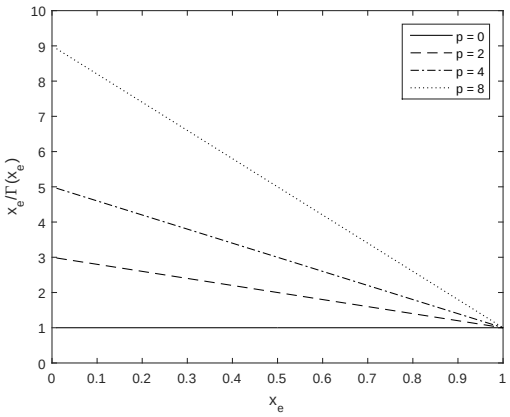

(d) RAMP: Density to $\Gamma(x_e)$ ratio

Figure 3.2: SIMP and RAMP interpolation schemes (*left*) and density ratios (*right*) for different penalization values p.

finite mass-to-stiffness ratio as the density vanishes (Figure 3.2d), and a non-zero first order derivative with respect to element density at $x_e = 0$. This non-zero sensitivity may help avoid numerical difficulties for certain optimization problems, such as the difficultly of void elements to regain material under the SIMP scheme under design dependent loading.

3.3 Algorithm structure

The topology optimization algorithm structure is depicted in the flowchart in Figure 3.3.

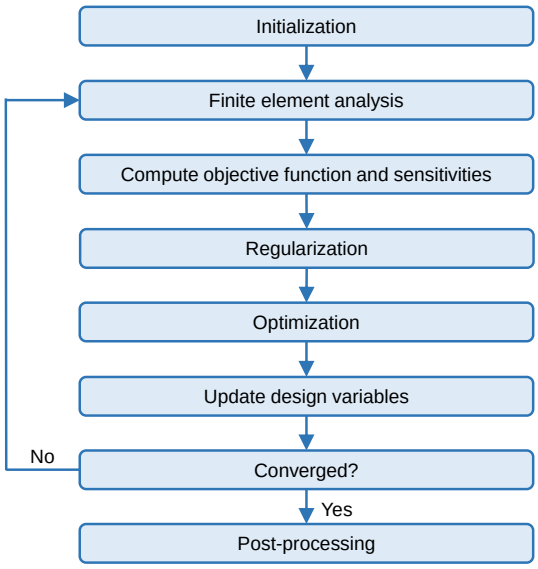

Figure 3.3: Topology optimization algorithm flow chart.

The first step is to initialize all parameters, prescribe boundary conditions, and design independent loads. Within the iterative loop, finite element analysis is undertaken and the objective function and sensitivities are computed. Regularization techniques are subsequently implemented, and optimization methods are used to update the design variables. Once the solution has converged to an optimal design, the algorithm exits the loop and performs post-processing, which includes design visualization and data output. The remainder of this chapter explores these phases of the topology optimization algorithm in further detail.

3.4 Initialization

In the initialization phase, the design domain is first discretized into N eight node hexahedral finite elements. Each element is assigned a design variable x_e that ranges from $0 \leq x_e \leq 1$, with the corresponding vector of design variables $\mathbf{x} = [x_1, x_2, \ldots, x_N]^T$. The design variables are initialized, typically to the prescribed volume fraction so there exists a uniform distribution of material throughout the domain. Any non-designable elements are set, the material properties and optimization parameters are initialized, and boundary conditions and design independent loads are prescribed.

3.5 Finite element analysis

The first step within the iterative loop is to perform finite element analysis. Within this loop the design dependent loads are applied, because the loads are a function of the material layout which changes with each iteration. The global stiffness matrix $\mathbf{K}(\mathbf{x})$ and force vector $\mathbf{F}$ are assembled from their corresponding element contributions

$$\mathbf{k}_e(x_e) = \int_{\Omega_e} \mathbf{B}_e^T \mathbf{C}_e(x_e) \mathbf{B}_e \, \mathrm{d}\Omega, \tag{3.12}$$

where $\mathbf{B}_e$ is the element strain-displacement matrix and $\mathbf{C}_e(x_e)$ is the constitutive matrix. $\mathbf{C}_e(x_e)$ is a function of element density by way of the interpolated material stiffness given in Equation 3.7. The general element force vector including design dependent body loads is given by

$$\begin{aligned} \mathbf{f}_e &= \mathbf{f}_e^b + \mathbf{f}_e^t \\ &= \int_{\Omega_e} \mathbf{N}_e{}^T \mathbf{b} \, \mathrm{d}\Omega + \int_{\Gamma_{t,e}} \mathbf{N}_e{}^T \mathbf{t}^* \, \mathrm{d}\Gamma, \end{aligned} \tag{3.13}$$

where $\mathbf{f}_e^b$ and $\mathbf{f}_e^t$ are the contribution from body forces and surface tractions, respectively. The global displacement vector is evaluated using either a direct or iterative solver from the relation

$$\mathbf{K}(\mathbf{x})\mathbf{U}(\mathbf{x}) = \mathbf{F}. \tag{3.14}$$

A full derivation of the finite element formulation for linear elasticity is provided in Appendix A.

3.6 Objective function and sensitivities

In this step the objective function and sensitivities are computed. Recall for the example minimum compliance formulation with design independent loading that the objective function may be expressed as

$$c(\mathbf{x}) = \mathbf{U}(\mathbf{x})^{\mathsf{T}}\mathbf{K}(\mathbf{x})\mathbf{U}(\mathbf{x}) = \mathbf{F}^{T}\mathbf{U}(\mathbf{x}). \tag{3.15}$$

Sensitivity analysis involves taking derivatives of the objective and constraint functions with respect to the design variable of element x_e. The sensitivities are required by the optimization algorithm to determine whether the element density should be increased or decreased in order to move closer to an optimal solution.

Taking the derivative of Equation 3.15 with respect to the density of element e,

$$\frac{\partial c(\mathbf{x})}{\partial x_e} = \mathbf{F}^{T}\frac{\partial \mathbf{U}(\mathbf{x})}{\partial x_e}. \tag{3.16}$$

Now, recall the equilibrium equation

$$\mathbf{K}(\mathbf{x})\mathbf{U}(\mathbf{x}) = \mathbf{F}. \tag{3.17}$$

Taking derivatives of both sides with respect to x_e and rearranging for the displacement derivative yields

$$\frac{\partial \mathbf{U}(\mathbf{x})}{\partial x_e} = -\mathbf{K}(\mathbf{x})^{-1}\frac{\partial \mathbf{K}(\mathbf{x})}{\partial x_e}\mathbf{U}(\mathbf{x}). \tag{3.18}$$

Substituting Equation 3.18 into Equation 3.16

$$\begin{aligned}\frac{\partial c(\mathbf{x})}{\partial x_e} &= -\mathbf{F}^{T}\mathbf{K}(\mathbf{x})^{-1}\frac{\partial \mathbf{K}(\mathbf{x})}{\partial x_e}\mathbf{U}(\mathbf{x}) \\ &= -\mathbf{U}(\mathbf{x})^{T}\frac{\partial \mathbf{K}(\mathbf{x})}{\partial x_e}\mathbf{U}(\mathbf{x}).\end{aligned} \tag{3.19}$$

The derivative is localized, meaning that it may be expressed in terms of element e only; however, the effect from other element densities is hidden in the element displacement vector (Bendsøe & Sigmund, 2003),

$$\frac{\partial c(\mathbf{x})}{\partial x_e} = -\mathbf{u}_e(x_e)^{T}\frac{\partial \mathbf{k}_e(x_e)}{\partial x_e}\mathbf{u}_e(x_e). \tag{3.20}$$

The sensitivity of the volume constraint is given by

$$\begin{aligned} \frac{\partial}{\partial x_e}\left(V(\mathbf{x}) - V_f^{max} V_0\right) &= \frac{\partial}{\partial x_e}\left(\sum_{i=1}^{N} x_i v_e\right) \\ &= \frac{\partial x_e v_e}{\partial x_e} \\ &= v_e, \end{aligned} \tag{3.21}$$

where the element volume v_e is the same for each element in a uniform mesh.

3.7 Regularization

Regularization techniques such as filtering and perimeter control methods are used to prevent numerical instabilities, ensure the existence of solutions and the manufacturability of optimal designs. Numerical instabilities include checkerboarding and mesh dependence.

Checkerboarding refers to the formation of alternating solid-void elements, resulting in a checkerboard-like pattern, depicted in Figure 3.4. This phenomenon occurs because topology optimization problems are typically ill-posed (Kohn & Strang, 1986a,b,c). Improved structures may be found by considering an increasingly smaller microstructure and, as such, the problem in general has no solution. For example, the objective function for the minimum compliance formulation will decrease with the introduction of more holes in a structure for a constant material volume (Sigmund & Petersson, 1998). In other words, checkerboard structures have an artificially high stiffness (Díaz & Sigmund, 1995).

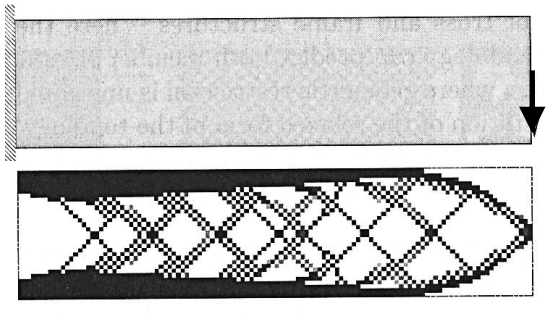

Figure 3.4: The checkerboard problem for a cantilever beam subject to an end load. Republished with permission of Springer, from Bendsøe & Sigmund (2003); permission conveyed through Copyright Clearance Center, Inc.

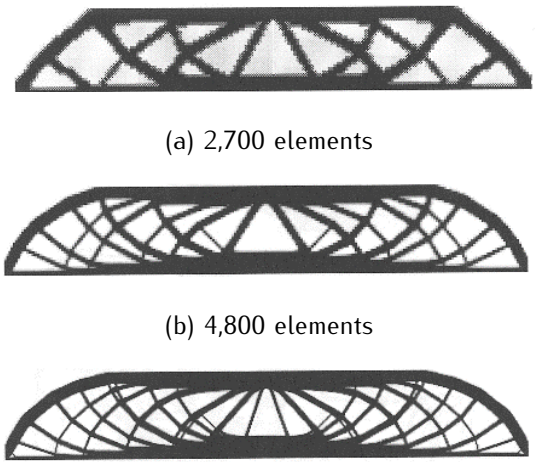

(a) 2,700 elements

(b) 4,800 elements

(c) 17,200 elements

Figure 3.5: MBB example showing mesh dependence. Republished with permission of Springer, from Bendsøe & Sigmund (2003); permission conveyed through Copyright Clearance Center, Inc.

Mesh dependence refers to the generation of different topologies for different domain discretizations of the same design problem, illustrated in Figure 3.5. Without regularization methods, an increase in the number of elements will typically result in a structure with a greater number of void spaces. Conversely, an increase in the number of elements of a mesh independent design results in a smoother representation of the same optimal structure.

Filtering is a common regularization method, and has been implemented in our code. This technique essentially sets the minimum length scale of the solution, thereby restricting the design space and ensuring the existence of solutions to the original continuum problem. The requirement of achieving a minimum length scale not only prevents the occurrence of checkerboards and mesh dependence but can also ensure the manufacturability of a design by controlling the minimum size of structural features. Two filtering methods are considered, namely sensitivity filtering (Sigmund & Petersson, 1998) and density filtering (Bourdin, 2001; Bruns & Tortorelli, 2001).

3.7.1 Sensitivity filtering

The sensitivity filter modifies the sensitivity of an element to be a weighted average of the sensitivities within a fixed neighbourhood. The filtered sensitivity may be expressed as follows,

$$\widehat{\frac{\partial c}{\partial x_e}} = \frac{1}{\max(\xi, x_e)\sum_{i\in N_e} H_{ei}} \sum_{i\in N_e} H_{ei} x_i \frac{\partial c}{\partial x_i}, \tag{3.22}$$

where N_e is the set of elements i for which the center-to-center distance $\Delta(e, i)$ from element e to element i is smaller than the filter radius r, and H_{ei} is a weight factor defined as

$$H_{ei} = \max(0, r - \Delta(e, i)). \tag{3.23}$$

H_{ei} decays linearly with distance from element e, and is equal to zero beyond the filter radius. The term ξ is a small positive number introduced to avoid division by zero. Figure 3.6 provides an illustrative two-dimensional schematic. The filter radius extends from the grey center element e to form the dark blue 'circle of influence'. The sensitivity of element e will be a weighted average of all elements whose centre lies within this circle, colored light blue for clarity. This concept is easily extended to three dimensions by instead considering a 'sphere of influence'.

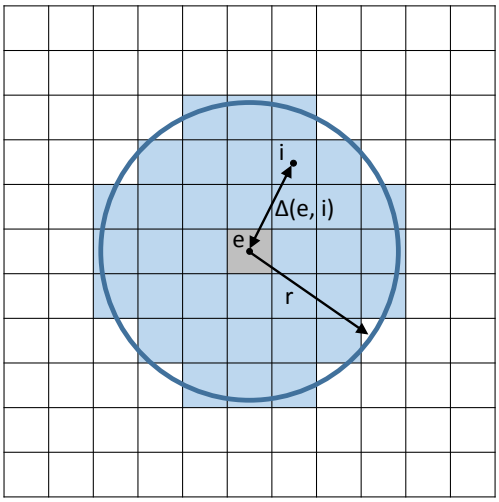

Figure 3.6: Schematic depicting the filter parameters

3.7.2 Density filtering

An alternate regularization approach is the use of a density filter which transforms the original densities x_e to be the weighted average of the densities within a fixed neighbourhood,

$$\tilde{x}_e = \frac{1}{\sum_{i \in N_e} H_{ei}} \sum_{i \in N_e} H_{ei} x_i. \tag{3.24}$$

The filtered densities $\tilde{x}_e$ are referred to as the physical densities. When a density filter is applied, the sensitivities of the objective function are first calculated using the physical densities $\tilde{x}_e$ rather than the design variables x_e. The sensitivities with respect to the design variables x_j are then obtained by means of the chain rule,

$$\frac{\partial \Psi}{\partial x_j} = \sum_{e \in N_j} \frac{\partial \Psi}{\partial \tilde{x}_e} \frac{\partial \tilde{x}_e}{\partial x_e} = \sum_{e \in N_j} \frac{1}{\sum_{i \in N_e} H_{ei}} H_{je} \frac{\partial \Psi}{\partial \tilde{x}_e}, \tag{3.25}$$

where the function Ψ represents either the objective function c or the material volume V.

3.8 Continuation schemes

Another common issue associated with topology optimization methods is obtaining locally optimal solutions rather than globally optimal solutions. This is a result of the optimization formulation being inherently nonconvex, and often having a large number of local minima. Conversely, for convex optimization problems every locally optimal solution is globally optimal and, as such, convex problems can be solved reliably and efficiently. A continuation method is therefore used to gradually change the optimization problem from an artificial convex problem to the original nonconvex design problem with each iteration (Bendsøe & Sigmund, 2003; Sigmund & Petersson, 1998). This is achieved by progressively increasing the penalization factor p in Equations 3.10 and 3.11.

In our analyses, the following continuation scheme is applied: for the first 10 iterations the penalty parameter is assigned a minimum value of

$$p = p^{min} = \begin{cases} 1, & \text{for SIMP interpolation,} \\ 0, & \text{for RAMP interpolation.} \end{cases} \tag{3.26}$$

Then, from the eleventh iteration onwards, the value of p is increased by Δp every 5 iterations until the maximum penalty value is attained. This jump in penalty value on the 11^{th}, 16^{th}, 21^{th}, etc., iterations is given by

$$\Delta p = \begin{cases} 0.5, & \text{for SIMP interpolation,} \\ 2, & \text{for RAMP interpolation,} \end{cases} \tag{3.27}$$

while the maximum penalty value is typically

$$p^{max} = \begin{cases} 3, & \text{for SIMP interpolation,} \\ 8, & \text{for RAMP interpolation.} \end{cases} \tag{3.28}$$

Continuation methods are not guaranteed to result in discrete final designs, and the trajectory followed by the global optimal solutions to the penalized problem may be discontinuous (Stolpe & Svanberg, 2001b). However, the continuation approach combined with penalization methods performs well in practice.

3.9 Mathematical programming methods

Performance of a topology optimization code in terms of convergence and efficiency is highly dependent on the choice of optimization algorithm, or mathematical programming method. The optimality criteria (OC), method of moving asymptotes (MMA), and the globally convergent method of moving asymptotes (GCMMA) are used in this project. The applicability of each method is highly dependent on the optimization problem and, as such, the methods' characteristics and formulations are detailed below.

3.9.1 Optimality criteria method

The OC method is a classical approach commonly used for minimum compliance problems with one constraint, typically a limit on volume or mass. The foundations of the OC method were introduced by Michell (1904). The OC method is an indirect method of optimization, where it does not optimize the objective function directly but attempts to satisfy a set of criteria related to the behaviour of the structure (Hassani & Hinton, 1998a). The method is formulated using a Lagrange function composed of objective and constraint functions according to the Kuhn-Tucker

condition,

$$\frac{\partial c(\mathbf{x})}{\partial x_e} + \lambda \frac{\partial V(\mathbf{x})}{\partial x_e} = 0, \tag{3.29}$$

where $c(\mathbf{x})$ is the compliance objective and λ is the Lagrange multiplier associated with a constraint on volume $V(\mathbf{x})$. Bendsøe (1995) constructed a heuristic updating scheme for the design variables

$$x_e^{new} = \begin{cases} \max(0, x_e - m), & \text{if } x_e B_e^{\eta} \leq \max(0, x_e - m), \\ \min(1, x_e + m), & \text{if } x_e B_e^{\eta} \geq \min(1, x_e - m), \\ x_e B_e^{\eta}, & \text{otherwise}, \end{cases} \tag{3.30}$$

where m is a positive move-limit, η is a numerical damping coefficient, and B_e is found from the optimality condition

$$B_e = -\frac{\partial c}{\partial x_e} \left(\lambda \frac{\partial v}{\partial x_e} \right)^{-1}, \tag{3.31}$$

where λ, the only unknown, is found by a bi-sectioning algorithm. The design variables are updated on each iteration until the optimal design is obtained. The OC method exhibits superior computational efficiency in comparison to the MMA and GCMMA, and typically converges in tens rather than hundreds of iterations. However, it has limited applicability due to the single constraint condition.

3.9.2 Method of moving asymptotes

The MMA is an efficient and robust method for general non-linear programming problems. It was introduced by Svanberg (1987) as a further generalization of the convex linearization method (CONLIN) presented by Fleury & Braibant (1986) . Unlike the OC method, there is no explicit updating scheme for the design variables. The MMA generates and solves an approximate subproblem in each iteration. The subproblem is computed using the function value and gradient information at the current iteration point, and so called moving asymptotes which are automatically updated on each iteration based on the information from previous iteration points. These subproblems are strictly convex and separable. Convexity allows the subproblems to be solved using dual or primal-dual methods, while separability means the necessary optimality conditions of the subproblem do not couple the design variables, resulting in solving n one-dimensional problems rather than one n-dimensional problem, which greatly

improves computational efficiency. The solution of the subproblem becomes the next iteration point, and the process continues until convergence is achieved.

The general formulation of nonlinear optimization problems given by Equation 3.1 is now expressed in the extended form, which includes "artificial" optimization variables

$$\begin{aligned} \text{minimize :} \quad & f_0(\mathbf{x}) + a_0 z + \sum_{i=1}^{m} (c_i y_i + \frac{1}{2} d_i y_i^2) \\ \text{subject to :} \quad & f_i(\mathbf{x}) - a_i z - y_i \leq 0, \quad i = 1, \ldots, m \\ & \mathbf{x} \in \mathbf{X}, \quad \mathbf{y} \geq \mathbf{0}, \quad z \geq 0, \end{aligned} \tag{3.32}$$

where

- $\mathbf{x} = (x_1, \ldots, x_n)^T \in \mathbb{R}^n$ is the vector of design variables, the "natural" optimization variables,
- $\mathbf{y} = (y_1, \ldots, y_m)^T \in \mathbb{R}^m$ and $z \in \mathbb{R}$ are the "artificial" optimization variables,
- $\mathbf{X} = \left\{ \mathbf{x} \in \mathbb{R}^n \,\middle|\, x_j^{min} \leq x_j \leq x_j^{max}, \; j = 1, \ldots, n \right\}$, where x_j^{min} and x_j^{max} are given real numbers which satisfy $x_j^{min} < x_j^{max} \; \forall \; j$,
- $f_0, f_1, \ldots, f_m$ are given, continuously differentiable, real-valued functions on $\mathbf{X}$. f_0 is the objective function, while $f_1, \ldots, f_m$ are the constraint functions,
- a_0, a_i, c_i, and d_i are given real numbers which satisfy $a_0 > 0, a_i \geq 0, c_i \geq 0, d_i \geq 0$, and $c_i + d_i > 0 \; \forall \; i$, and also $a_i c_i > a_0 \; \forall \; i$ with $a_i > 0$.

Typically in any optimal solution $(\hat{x}, \hat{y})$ of Equation 3.32, $\hat{y} = 0$ and the corresponding $\hat{x}$ is an optimal solution of Equation 3.1, providing the constants c_i are chosen to be very large. It is advantageous to work with Equation 3.32 as opposed to Equation 3.1 because there always exists feasible solutions and at least one optimal solution of Equation 3.32, and each optimal solution will always satisfy the Karush-Kuhn-Tucker conditions.

Recalling the problem formulation of Equation 3.32, and given the current iteration point $(\mathbf{x}^{(k)}, \mathbf{y}^{(k)}, z^{(k)})$, the approximate subproblem is generated, where the functions $f_i(\mathbf{x})$ are replaced by convex functions $\tilde{f}_i(\mathbf{x})$. The subproblem is solved to obtain the next iteration point

$(\mathbf{x}^{(k+1)}, \mathbf{y}^{(k+1)}, z^{(k+1)})$,

$$\begin{aligned} \text{minimize}: \quad & \tilde{f}_0^{(k)}(\mathbf{x}) + a_0 z + \sum_{i=1}^{m} (c_i y_i + \frac{1}{2} d_i y_i^2) \\ \text{subject to}: \quad & \tilde{f}_i^{(k)}(\mathbf{x}) - a_i z - y_i \leq 0, \quad i = 1, \ldots, m \\ & \alpha_j^{(k)} \leq x_j \leq \beta_j^{(k)}, \quad j = 1, \ldots, n \\ & y_i \geq 0, \quad i = 1, \ldots, m \\ & z \geq 0. \end{aligned} \tag{3.33}$$

The approximating functions $\tilde{f}_i^{(k)}(\mathbf{x})$ are chosen as

$$\tilde{f}_i^{(k)}(\mathbf{x}) = \sum_{j=1}^{n} \left(\frac{p_{ij}^{(k)}}{u_j^{(k)} - x_j} + \frac{q_{ij}^{(k)}}{x_j - l_j^{(k)}} \right) + r_i^{(k)}, \quad i = 1, \ldots, m. \tag{3.34}$$

For one design variable, either $p_{ij}^{(k)}$ or $q_{ij}^{(k)}$ must equal zero, and therefore the MMA approximation is monotonous. The author refers the reader to Svanberg (1987) for further details. The bounds $\alpha_j^{(k)}$ and $\beta_j^{(k)}$ are chosen as

$$\alpha_j^{(k)} = \max \left\{ x_j^{min},\ l_j^{(k)} + 0.1(x_j^{(k)} - l_j^{(k)}),\ x_j^{(k)} - 0.5(x_j^{max} - x_j^{min}) \right\}, \tag{3.35}$$

$$\beta_j^{(k)} = \min \left\{ x_j^{max},\ u_j^{(k)} - 0.1(u_j^{(k)} - x_j^{(k)}),\ x_j^{(k)} + 0.5(x_j^{max} - x_j^{min}) \right\}. \tag{3.36}$$

The lower asymptotes $l_j^{(k)}$ and upper asymptotes $u_j^{(k)}$ are given by the following rules. For the first two iterations, $k = 1$ and $k = 2$,

$$l_j^{(k)} = x_j^{(k)} - 0.5(x_j^{max} - x_j^{min}), \tag{3.37}$$

$$u_j^{(k)} = x_j^{(k)} + 0.5(x_j^{max} - x_j^{min}). \tag{3.38}$$

For subsequent iterations ($k \geq 3$),

$$\begin{aligned} l_j^{(k)} &= x_j^{(k)} - \gamma_j^{(k)}(x_j^{(k-1)} - l_j^{(k-1)}), \\ u_j^{(k)} &= x_j^{(k)} + \gamma_j^{(k)}(u_j^{(k-1)} - x_j^{(k-1)}), \end{aligned} \tag{3.39}$$

where

$$\gamma_j^{(k)} = \begin{cases} 0.7 & \text{if} \quad (x_j^{(k)} - x_j^{(k-1)})(x_j^{(k-1)} - x_j^{(k-2)}) < 0, \\ 1.2 & \text{if} \quad (x_j^{(k)} - x_j^{(k-1)})(x_j^{(k-1)} - x_j^{(k-2)}) > 0, \\ 1.0 & \text{if} \quad (x_j^{(k)} - x_j^{(k-1)})(x_j^{(k-1)} - x_j^{(k-2)}) = 0. \end{cases} \tag{3.40}$$

Taking $l_j = 0$ and $u_j = +\infty$ reduces the MMA to the CONLIN approach.

The moving asymptotes adjust the degree of convexity of the approximation, thereby affecting the speed of convergence. It can be seen from Equations 3.39 and 3.40 that if the signs of the last three iterations oscillate, then the two asymptotes are moved closer to the current iteration point $x_j^{(k)}$ to yield a more conservative approximation of the original problem. Alternately, if the signs are equal, then the two asymptotes are moved further away from $x_j^{(k)}$ to relax the process and improve the rate of convergence.

3.9.3 Globally convergent method of moving asymptotes

A disadvantage of the MMA is that it may not converge to a solution for certain problems. Svanberg (2002) therefore proposed the GCMMA, which relies on strictly convex conservative approximations to solve problems in the form of Equation 3.32 . This method is globally convergent in the sense that from any starting point, the sequence of generated iteration points converges to a stationary point, or in other words to the set of Karush-Kuhn-Tucker points. However, there is no guarantee that the stationary point will be the global optimum of the problem, therefore continuation schemes as detailed in section 3.8 must be implemented.

The GCMMA consists of “outer" and “inner" iterations. The outer iteration starts from the current iterate $x^{(k)}$ and results in a new iterate $x^{(k+1)}$. Gradients of the original functions f_i are calculated only once in each outer iteration, thus computational efficiency is acceptable yet slower than the MMA. A convex subproblem is generated and solved in each inner iteration. This solution may be accepted as the new iterate $x^{(k+1)}$ or it may be rejected, in which case another inner iteration takes place with a modified subproblem. Solution acceptance requires the approximating functions to be conservative, that is the approximating objective and constraint functions become greater than or equal to the original functions at the optimal solution of the subproblem. This implies that the optimal solution of the subproblem is a feasible solution of the original problem with a lower objective value than the previous iterate. The formulation is very similar to that for the MMA; however, in the case of the GCMMA the

coefficients $p_{ij}^{(k)}$ or $q_{ij}^{(k)}$ in Equation 3.34 are simultaneously non-zero which leads to a non-monotonous approximation of the initial problem. The bounds $\alpha_j^{(k)}$ and $\beta_j^{(k)}$ and the asymptotes $l_j^{(k)}$ and $u_j^{(k)}$ are updated between each outer iteration as in the original MMA.

An important difference between the MMA and GCMMA is that the former uses monotonous approximation methods, while the latter uses non-monotonous approximation methods. The choice of best optimization algorithm is therefore highly dependent on the nature of the optimization problem, where the convexity and conservativeness must be accurately represented. The rate of convergence is typically high when using the MMA for a monotonous structural response function, or when using the GCMMA for a non-monotonous function. If the MMA is used for a non-monotonous function, or likewise the GCMMA for a monotonous function, convergence is slow or the method may fail to produce an optimal solution (Zuo et al., 2007). In problems where both methods converge, the MMA typically converges in fewer iterations than the GCMMA. This is due to the conservative nature of the GCMMA approximations.

3.10 Post-processing

Post-processing occurs once the solution has converged to an optimal design and the algorithm has quit the iterative loop. This stage includes design visualization and data output. Image processing techniques, such as thresholding, are typically applied to the optimal design to ensure a discrete solution with no intermediate densities. As is customary in topology optimization methods, the final design is subsequently represented using a smoothed iso-density surface rather than the original mesh discretization. This iso-density surface is generated using the MATLAB function *isosurface* and the optimal volumetric densities obtained from the analysis. Furthermore, output data such as the iteration history may also be plotted.

3.11 Hardware and computational time

This topology optimization code was run using a desktop computer with Microsoft Windows 7, an Intel Core i7-3770 @ 3.4 GHz processor, 16 GB memory, and MATLAB R2015b. In terms of computational time, the code was deemed to be efficient. For example, the computational time was calculated for the most complex analysis presented in this thesis: the multi-objective problem detailed in Section 6.3. For the particular instance of a domain discretization of 30 x

30 x 30 elements, a structural Pareto weight of $w_s = 0.5$, a volume fraction of $V_f = 0.30$, and a filter radius of $r = 1$ μm, the computational time for the pre-optimization loop calculations was 5.3 seconds, while a single optimization loop iteration, computed as an average over ten iterations, was calculated to be 4.4 seconds. Convergence to an optimal solution by 80 iterations was on the order of 6 minutes.

Chapter 4

Minimum Compliance with Design Dependent Volume Expansion

This chapter explores a minimum compliance problem formulation with design dependent volume expansion to simulate lithiation of the anode structure. The problem formulation, including both the objective function and sensitivity analysis, is first presented. The key numerical difficulties associated with design dependent topology optimization problems are subsequently discussed. A benchmark thermoelastic problem is then investigated, followed by the detailed optimization and analysis of the silicon anode structure.

4.1 Problem formulation

The design objective is to determine a silicon anode structure that can better withstand the large volume expansion upon lithiation, and reduce the lithiation-induced stress. We formulate the problem in terms of linear elasticity, and assume uniform lithiation of the structure. We consider an extension of the classical problem formulation of minimum compliance presented in Chapter 3.1, where the problem formulation is modified to include design dependent volume expansion. The volume expansion of the structure due to lithiation is conveniently modelled using the equations for volume expansion due to thermal loading. While thermal loading does not physically occur within the battery, the application of a volumetric strain equivalent to the lithiation-induced strain is an efficient approach to modelling lithiation behaviour. The design dependent nature of the problem relates to the fact that the volume expansion is applied only to the silicon anode, and not the electrolyte.

The compliance may be defined as the virtual work of the loads on the displacements they

generate Prager (1968). Therefore, this design objective minimizes the product of resulting displacements and their corresponding total loads (Pedersen & Pedersen, 2010a), and effectively minimizes a global measure of deformation and an average measure of stress. Unlike the design independent loading case, the compliance is not equal to the total elastic energy for thermoelastic structures or structures with design dependent loads (Pedersen & Pedersen, 2012). For a detailed comparison between compliance and elastic strain energy for mechanical and thermal loads, the author refers the reader to Zhang et al. (2014).

The general variational problem formulation for a minimum compliance objective with design dependent volume expansion is given by

$$
\begin{aligned}
\min_{u\in U,\rho} : \quad & \int_\Omega bu \; d\Omega + \int_\Omega \mathbf{C}_{ijkl}(x)\epsilon_{ij}(u)\epsilon^*_{kl}(x) \; d\Omega + \int_{\Gamma_t} tu \; ds \\
\text{subject to} : \quad & \int_\Omega \mathbf{C}_{ijkl}(x)\epsilon_{ij}(u)\epsilon_{kl}(v) \; d\Omega = \\
& \quad \int_\Omega bv \; d\Omega + \int_\Omega \mathbb{C}_{ijkl}(x)\epsilon_{ij}(v)\epsilon^*_{kl}(x) \; d\Omega + \int_{\Gamma_t} tv \; ds, \quad \text{for all } v \in U, \\
& \int_\Omega \rho(x) \; d\Omega \leq V, \\
& \rho(x) \in \{0, 1\}.
\end{aligned}
$$

Here, b denotes the body forces, u the equilibrium displacement, $\mathbf{C}(x)$ the constitutive matrix, x a point within the domain Ω, $\epsilon(u)$ the linearized strains, $\epsilon^*(x)$ the design dependent volumetric strain, t the surface tractions, and U the space of kinematically admissible displacement fields. The minimum compliance objective is subject to the equilibrium equation and a constraint on material volume, where $\rho(x)$ is the pointwise volume fraction and V the total volume of material. $\epsilon^*(x)$ typically represents the strain due to thermal loading,

$$\epsilon^*_{kl}(x) = \alpha_{kl}(x)\Delta T, \tag{4.1}$$

where $\alpha(x)$ is the coefficient of thermal expansion, and ΔT is the change in temperature. This problem formulation assumes the constitutive law for linear thermoelasticity,

$$\sigma_{ij}(u) = \mathbf{C}_{ijkl}(x)\epsilon_{kl}(u) - \mathbf{C}_{ijkl}(x)\epsilon^*_{kl}(x). \tag{4.2}$$

In our research, $\epsilon^*(x)$ is used to model the volumetric expansion of the silicon anode due to

lithiation.

Using a finite element discretization, the discrete formulation of this minimum compliance problem is given by

$$\begin{aligned} \min_{x}: \quad & c(\tilde{\mathbf{x}}) = \mathbf{F}(\tilde{\mathbf{x}})^T \mathbf{U}(\tilde{\mathbf{x}}) \\ \text{subject to}: \quad & \mathbf{K}(\tilde{\mathbf{x}})\mathbf{U}(\tilde{\mathbf{x}}) = \mathbf{F}(\tilde{\mathbf{x}}) = \mathbf{F}^m + \mathbf{F}^v(\tilde{\mathbf{x}}), \\ & \frac{V(\tilde{\mathbf{x}})}{V_0} \leq V_f^{max}, \\ & \mathbf{0} \leq \mathbf{x} \leq \mathbf{1}. \end{aligned} \tag{4.3}$$

The use of a density filter is assumed from the outset, and therefore the problem formulation is expressed in terms of physical densities $\tilde{\mathbf{x}}$. Here, $c(\tilde{\mathbf{x}})$ is the compliance, $\mathbf{F}(\tilde{\mathbf{x}})$ is the global force vector, $\mathbf{U}(\tilde{\mathbf{x}})$ is the global displacement vector, and $\mathbf{K}(\tilde{\mathbf{x}})$ is the global stiffness matrix. Neglecting body forces, $\mathbf{F}(\tilde{\mathbf{x}})$ is composed of two terms: the design independent mechanical load vector $\mathbf{F}^m$, and the design dependent volume expansion load vector $\mathbf{F}^v(\tilde{\mathbf{x}})$. Furthermore, $V(\tilde{\mathbf{x}}) = \sum_{e=1}^{N} \tilde{x}_e v_e$ is the material volume, V_0 is the design domain volume, and V_f^{max} is the maximum allowable volume fraction.

The global stiffness matrix is assembled from the element contributions,

$$\mathbf{k}_e(\tilde{x}_e) = \int_{\Omega_e} \mathbf{B}_e^T \mathbf{C}_e(\tilde{x}_e) \mathbf{B}_e \, \mathrm{d}\Omega, \tag{4.4}$$

where $\mathbf{B}_e$ is the element strain-displacement matrix and $\mathbf{C}_e(x_e)$ is the constitutive matrix, which is a function of element density. The element stiffness matrix may be equivalently expressed as the product of the design dependent and design independent terms,

$$\mathbf{k}_e(\tilde{x}_e) = E_e(\tilde{x}_e) \int_{\Omega_e} \mathbf{B}_e^T \bar{\mathbf{C}}_e \mathbf{B}_e \, \mathrm{d}\Omega, \tag{4.5}$$

$$= E_e(\tilde{x}_e) \bar{\mathbf{k}}_e, \tag{4.6}$$

where $E_e(\tilde{x}_e)$ is the design dependent Young's Modulus, $\bar{\mathbf{C}}_e$ is the constitutive matrix for a unit Young's Modulus given in Appendix A, and $\bar{\mathbf{k}}_e$ is the design independent integral term that may be computed just once outside the iterative loop of the topology optimization algorithm.

The global force vector is assembled from the element contributions of the mechanical load

vector and the volume expansion load vector,

$$\mathbf{f}_e^m = \int_{\Gamma_{t,e}} \mathbf{N}_e{}^T \mathbf{t}\, d\Gamma, \tag{4.7}$$

where $\mathbf{N}_e$ is the element shape function matrix, and

$$\mathbf{f}_e^v(\tilde{x}_e) = \int_{\Omega_e} \mathbf{B}_e^T \mathbf{C}_e(\tilde{x}_e) \boldsymbol{\epsilon}_e^*(\tilde{x}_e) d\Omega. \tag{4.8}$$

Assuming isotropic expansion, Equation 4.8 may be expressed as

$$\mathbf{f}_e^v(\tilde{x}_e) = \int_{\Omega_e} \mathbf{B}_e^T \mathbf{C}_e(\tilde{x}_e) \epsilon^*(\tilde{x}_e) \boldsymbol{\phi}^T d\Omega, \tag{4.9}$$

where

$$\boldsymbol{\phi} = [1 \quad 1 \quad 1 \quad 0 \quad 0 \quad 0] \tag{4.10}$$

for three-dimensional analysis. Shifting the design dependent terms outside of the integral yields

$$\begin{aligned} \mathbf{f}_e^v(\tilde{x}_e) &= E_e(\tilde{x}_e) \epsilon^*(\tilde{x}_e) \int_{\Omega_e} \mathbf{B}_e^T \bar{\mathbf{C}}_e \boldsymbol{\phi}^T d\Omega, \\ &= \gamma(\tilde{x}_e)\ \bar{\mathbf{f}}_e^v, \end{aligned} \tag{4.11}$$

where $\gamma(\tilde{x}_e)$ is termed the volume expansion load coefficient, which is equivalent to the TSC introduced by Gao and Zhang Gao & Zhang (2010) for the case of thermal loading. $\gamma(\tilde{x}_e)$ allows for just one material interpolation for the volume expansion load vector, ensuring compatibility with the linear design dependence of the stiffness matrix. For a uniform mesh, the integral term $\bar{\mathbf{f}}_e^v$ is the same for each element and independent of density, and therefore $\bar{\mathbf{f}}_e^v$ is computed just once outside the optimization loop.

4.1.1 Sensitivity analysis.

Some changes must be made to the sensitivities presented in Section 3.6, as the force vector is now dependent on density. Furthermore, the sensitivities presented in this section are expressed in terms of physical densities. As such they require subsequent modification using Equation 3.25 to transform the sensitivities to a derivative with respect to the design variables.

Recall the compliance may be expressed as

$$c(\tilde{\mathbf{x}}) = \mathbf{F}(\tilde{\mathbf{x}})^{\mathsf{T}}\mathbf{U}(\tilde{\mathbf{x}}). \tag{4.12}$$

Taking the derivative with respect to physical density of element e using the chain rule,

$$\frac{\partial c(\tilde{\mathbf{x}})}{\partial \tilde{x}_e} = \left(\frac{\partial \mathbf{F}(\tilde{\mathbf{x}})}{\partial \tilde{x}_e}\right)^T \mathbf{U}(\tilde{\mathbf{x}}) + \mathbf{F}(\tilde{\mathbf{x}})^T \frac{\partial \mathbf{U}(\tilde{\mathbf{x}})}{\partial \tilde{x}_e}. \tag{4.13}$$

Now, recall the equilibrium equation

$$\mathbf{K}(\tilde{\mathbf{x}})\mathbf{U}(\tilde{\mathbf{x}}) = \mathbf{F}(\tilde{\mathbf{x}}) = \mathbf{F}^m + \mathbf{F}^v(\tilde{\mathbf{x}}). \tag{4.14}$$

Taking derivatives of both sides with respect to $\tilde{x}_e$,

$$\frac{\partial \mathbf{K}(\tilde{\mathbf{x}})}{\partial \tilde{x}_e}\mathbf{U}(\tilde{\mathbf{x}}) + \mathbf{K}(\tilde{\mathbf{x}})\frac{\partial \mathbf{U}(\tilde{\mathbf{x}})}{\partial \tilde{x}_e} = \frac{\partial \mathbf{F}(\tilde{\mathbf{x}})}{\partial \tilde{x}_e}, \tag{4.15}$$

and rearranging for the displacement derivative,

$$\frac{\partial \mathbf{U}(\tilde{\mathbf{x}})}{\partial \tilde{x}_e} = \mathbf{K}(\tilde{\mathbf{x}})^{-1}\left(\frac{\partial \mathbf{F}(\tilde{\mathbf{x}})}{\partial \tilde{x}_e} - \frac{\partial \mathbf{K}(\tilde{\mathbf{x}})}{\partial \tilde{x}_e}\mathbf{U}(\tilde{\mathbf{x}})\right). \tag{4.16}$$

Substitution of Equation 4.16 into Equation 4.13 yields

$$\frac{\partial c(\tilde{\mathbf{x}})}{\partial \tilde{x}_e} = \left(\frac{\partial \mathbf{F}(\tilde{\mathbf{x}})}{\partial \tilde{x}_e}\right)^T \mathbf{U}(\tilde{\mathbf{x}}) + \mathbf{F}(\tilde{\mathbf{x}})^T \mathbf{K}(\tilde{\mathbf{x}})^{-1}\left(\frac{\partial \mathbf{F}(\tilde{\mathbf{x}})}{\partial \tilde{x}_e} - \frac{\partial \mathbf{K}(\tilde{\mathbf{x}})}{\partial \tilde{x}_e}\mathbf{U}(\tilde{\mathbf{x}})\right). \tag{4.17}$$

Using the relation $\mathbf{F}(\tilde{\mathbf{x}})^T\mathbf{K}(\tilde{\mathbf{x}})^{-1} = \mathbf{U}(\tilde{\mathbf{x}})^T$ and rearranging the above expression yields the final compliance sensitivity expression in terms of the physical element density

$$\begin{aligned}\frac{\partial c(\tilde{\mathbf{x}})}{\partial \tilde{x}_e} &= 2\mathbf{U}^T(\tilde{\mathbf{x}})\frac{\partial \mathbf{F}(\tilde{\mathbf{x}})}{\partial \tilde{x}_e} - \mathbf{U}(\tilde{\mathbf{x}})^T\frac{\partial \mathbf{K}(\tilde{\mathbf{x}})}{\partial \tilde{x}_e}\mathbf{U}(\tilde{\mathbf{x}}) \\ &= 2\mathbf{u}_e^T(\tilde{x}_e)\frac{\partial \mathbf{f}_e(\tilde{x}_e)}{\partial \tilde{x}_e} - \mathbf{u}_e(\tilde{x}_e)^T\frac{\partial \mathbf{k}_e(\tilde{x}_e)}{\partial \tilde{x}_e}\mathbf{u}_e(\tilde{x}_e).\end{aligned} \tag{4.18}$$

The RAMP interpolation presented in Chapter 3.2.2 is used to interpolate the Young's modulus

$E_e(\tilde{x}_e)$ and the design dependent force term $\gamma(\tilde{x}_e)$. For example,

$$\begin{aligned}\gamma(\tilde{x}_e) &= \gamma^{(b)} + \frac{\tilde{x}_e}{1+p(1-\tilde{x}_e)}(\gamma^{(a)} - \gamma^{(b)}) \\ &= E^{(b)}\epsilon^{*(b)} + \frac{\tilde{x}_e}{1+p(1-\tilde{x}_e)}(E^{(a)}\epsilon^{*(a)} - E^{(b)}\epsilon^{*(b)}).\end{aligned} \tag{4.19}$$

Therefore, the derivative of force in Equation 4.18 is given by

$$\begin{aligned}\frac{\partial \mathbf{f}_e(\tilde{x}_e)}{\partial \tilde{x}_e} &= \frac{\partial}{\partial \tilde{x}_e}(\mathbf{f}_e^m + \mathbf{f}_e^v(\tilde{x}_e)) \\ &= \frac{\partial \gamma(\tilde{x}_e)}{\partial \tilde{x}_e}\ \bar{\mathbf{f}}_e^v \\ &= \frac{1+p}{(1+(1-\tilde{x}_e))^2}(\gamma^{(a)} - \gamma^{(b)})\ \bar{\mathbf{f}}_e^v,\end{aligned} \tag{4.20}$$

while the derivative of the element stiffness matrix is

$$\begin{aligned}\frac{\partial \mathbf{k}_e(\tilde{x}_e)}{\partial \tilde{x}_e} &= \frac{\partial E(\tilde{x}_e)}{\partial \tilde{x}_e}\bar{\mathbf{k}}_e \\ &= \frac{1+p}{(1+p(1-\tilde{x}_e))^2}(E^{(a)} - E^{(b)})\ \ \bar{\mathbf{k}}_e.\end{aligned} \tag{4.21}$$

The sensitivity of the volume constraint is the same as for the design independent loading case (Equation 3.21), only now it is written in terms of the physical densities,

$$\frac{\partial}{\partial \tilde{x}_e}\left(V(\tilde{\mathbf{x}}) - V_f^{max}V_0\right) = v.$$

4.2 Difficulties of design dependent loading

There are some difficulties associated with design dependent loading problems that must be resolved in order for topology optimization methods to yield successful results. These problems include the fact that the objective function may oscillate and fail to converge to an optimum, the optimal solution may have an inactive volume constraint, or the optimal solution may be singular (the entire domain has zero density) when an upper inequality bound on volume is imposed (Gao et al., 2008; Turteltaub & Washabaugh, 1999). This behaviour may be attributed to the non-monotonous nature of the objective function and the formulation of the volume constraint. Furthermore, design dependent loads may cause an undesirable parasitic effect for low density regions, manifesting as light grey elements in regions that should be

void (Bruyneel & Duysinx, 2005). This issue may be remedied by careful selection of the interpolation scheme.

Due to the addition of design dependent loading, Equation 4.18 shows that the derivative of the objective function gains an extra term, which may result in a non-monotonous objective function with respect to some design variables. This has the effect of possibly increasing the compliance with the addition of material, unlike the case of pure mechanical loading where additional material always decreases the value of the compliance. Recall from Chapter 3.9 that the MMA is best suited to monotonous functions such as design independent loading problems. If this method were to be used for a design dependent loading case, one can expect the value of the objective to oscillate and that it may fail to converge, or that the volume constraint may become inactive (Bruyneel & Duysinx, 2005). Therefore, to avoid convergence difficulties for design dependent problems, the non-monotonous nature of the objective function necessitates the use of the GCMMA optimization algorithm.

Singular behaviour and parasitic effects may be attributed to an inactive volume constraint at the optimal topology. This unconstrained nature is characteristic of problems with design dependent loads. Classical minimum compliance topology optimization problems prescribe an inequality volume constraint, which is an upper limit on the allowable design material. One method to help prevent these undesirable effects is to impose both an upper and a lower bound on volume fraction (Bruyneel & Duysinx, 2005; Gao et al., 2008). This theoretically prevents the optimizer from attaining zero density throughout the domain. However, it must be noted that this method must be used in conjunction with the appropriate optimizer for a successful outcome. The updated problem formulation may be expressed as

$$\begin{aligned} \min_{x} : \quad & c(\tilde{\mathbf{x}}) = \mathbf{U}(\tilde{\mathbf{x}})^{\mathsf{T}}\mathbf{K}(\tilde{\mathbf{x}})\mathbf{U}(\tilde{\mathbf{x}}) \\ \text{subject to} : \quad & V_f^{min} \leq \frac{V(\tilde{\mathbf{x}})}{V_0} \leq V_f^{max}, \\ & \mathbf{K}(\tilde{\mathbf{x}})\mathbf{U}(\tilde{\mathbf{x}}) = \mathbf{F}^m + \mathbf{F}^v(\tilde{\mathbf{x}}), \\ & \mathbf{0} \leq \mathbf{x} \leq \mathbf{1}. \end{aligned} \tag{4.22}$$

Another cause of parasitic effects for design dependent loading problems is the SIMP interpolation scheme, which exhibits zero sensitivity at zero density. This causes the compliance to be insensitive to element density near values of zero density and makes it difficult

for elements that become void to regain material. Gao & Zhang (2010) has shown that an effective solution to stabilize convergence and produce discrete optimal structures is to utilize the RAMP interpolation model instead of the SIMP model for problems with design dependent loading.

4.3 Thermoelastic test case

This section explores a benchmark thermoelastic problem first studied by Rodrigues & Fernandes (1995) using a homogenization method, then subsequently by other authors such as Gao & Zhang (2010), Pedersen & Pedersen (2010b) and Deaton & Grandhi (2013b). The problem determines the material distribution of a 2D linear-elastic solid for a bi-clamped beam that minimizes compliance subject to a uniform temperature difference in terms of a design dependent load, in addition to a design independent mechanical load and a constraint on volume. A schematic of the problem setup and a selection of results as implemented by Rodrigues & Fernandes (1995) are shown in Figure 4.1.

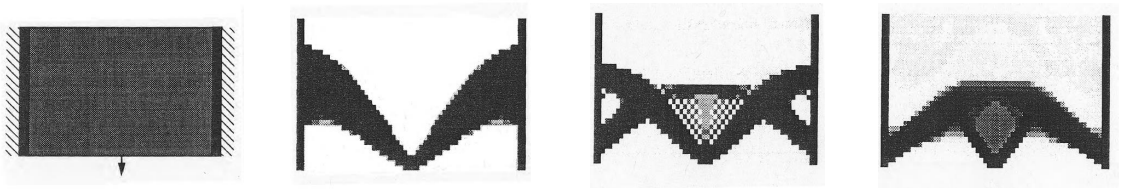

(a) Initial design (b) $\Delta T = 0°C$ (c) $\Delta T = 1°C$ (d) $\Delta T = 4°C$

Figure 4.1: The bi-clamped beam thermoelastic problem. Reprinted from Rodrigues & Fernandes (1995), Copyright (1995), with permission from John Wiley and Sons.

This problem is explored in detail for several reasons. Firstly, it is directly relevant to the design dependent problem of minimizing the volume expansion of a Li-ion battery upon lithiation, which will be discussed later in this chapter. Secondly, this test case provides an opportunity to explore of the difficulties associated with design dependent loading cases and experiment with potential solutions to overcome these issues whilst working on a known problem.

4.3.1 Implementation

The thermoelastic test case is implemented in our topology optimization code with every attempt made to replicate the problem accurately. Notable differences include a three dimensional implementation rather than the 2D implementation in the various literature, the choice of optimizer, and the use of both a lower and upper bound on volume fraction. Where no parameter values were given, the author chose the most suitable values based on experience and experimentation.

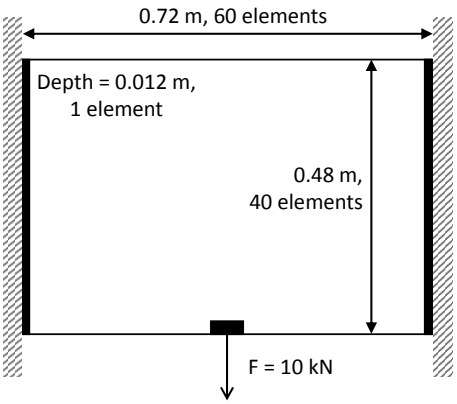

Figure 4.2: Thermoelastic benchmark problem schematic

Figure 4.2 depicts a schematic of the optimization problem. The size of the domain is 0.72 m x 0.48 m x 0.012 m, and is discretized into 60 x 40 x 1 elements such that each element is cubic in shape. The left and right faces are rigidly constrained while all other faces are free. As in Rodrigues & Fernandes (1995), one column of non-design elements is placed at both the left and right ends of the beam. Additionally a non-design region consisting of 8 elements is located at the site of the applied mechanical load to prevent a stress singularity (Deaton & Grandhi, 2013b). The domain is initialized with a homogeneous distribution of material, i.e., each element is initially assigned a density equal to the upper volume fraction bound. The material properties and important parameters are listed below

- Elastic modulus, $E = 210$ GPa,
- Poisson's ratio, $\nu = 0.3$,
- Mechanical load, $F^m = 10$ kN applied along the center of the bottom face,
- Coefficient of thermal expansion, $\alpha = 1.1$ x 10^{-5}/°C,
- Uniform change in temperature, $\Delta T = 1$°C or $\Delta T = 3$°C

- Volume fraction, $V_f = 0.25 - 0.30$,
- RAMP interpolation scheme, $p = 8$ for $E_e(\tilde{x}_e)$, $p = 0$ for $\beta(\tilde{x}_e)$,
- Density filter, r = 0.024 m (= 2 element lengths).

4.3.2 Results

Figure 4.3 shows results for the case of mechanical loading only ($\Delta T = 0°C$), using both MMA and GCMMA optimizers. The MMA algorithm converges quickly to the solution shown in Figure 4.3a, which is consistent with the results given in Pedersen & Pedersen (2010b). The volume fraction is very slightly greater than the upper bound of 0.3, which is acceptable for this method. Figure 4.3c shows that the GCMMA has difficulty obtaining a physical solution, with the two struts not reaching the side supports. This is despite the iteration history indicating convergence to an optimal solution, as shown in Figure 4.3d. This behaviour is due to the objective function being monotonous for the pure mechanical loading case. Thus, as previously mentioned in Section 3.9, the MMA is best suited to a problem with design independent loads rather than the GCMMA method which is better suited for design dependent loading. As a side note, the jumps in values on the plots at 10, 15, 20, 25, and 30 iterations are due to the continuation scheme progressively increasing the RAMP penalization in the hopes of converging to a global rather than local optimum. For further details see Section 3.8.

A temperature change is now applied, in addition to the mechanical loading. Firstly, we explore the effect of choosing the MMA method. Results are shown in Figure 4.4 for a temperature change of $\Delta T = 1°C$. The volume constraint is severely violated, reaching almost 90%, leading to an unsuitable solution. This is likely due to the MMA monotonous approximations being incompatible with the non-monotonous behavior of design dependent problems. This result once again confirms the importance of selecting an appropriate optimizer based on the behavior of the problem to be optimized.

Figure 4.5 shows results using the GCMMA for two temperature cases. The optimal solutions appear in agreement with the literature, such as the results shown in Figure 4.1 by Rodrigues & Fernandes (1995). Both results of Figure 4.5 exhibit good convergence, and the volume fractions remain within allowable bounds. One interesting difference between the results shown in Figure 4.1 and Figure 4.5, is that our results feature gaps between the side walls and the internal structure. These slits result in less coupling and potentially improved thermoelastic performance in comparison to the designs presented by Rodrigues. Possible

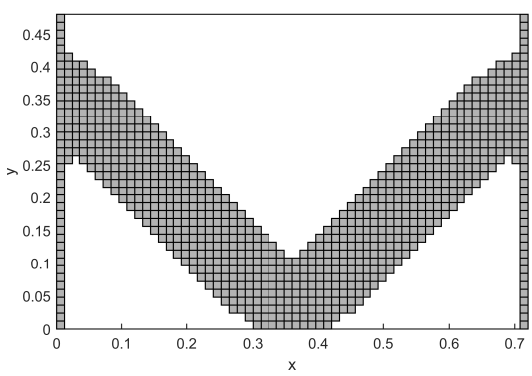

(a) Density distribution: MMA

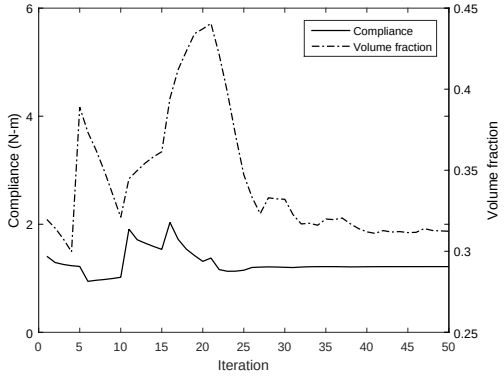

(b) Iteration history: MMA

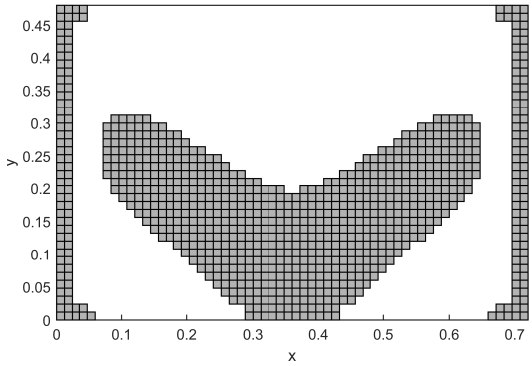

(c) Density distribution: GCMMA

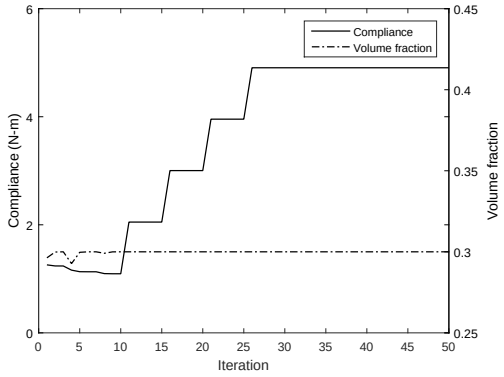

(d) Iteration history: GCMMA

Figure 4.3: Optimized designs and iteration history plots for applied mechanical loading using a volume fraction of $V_f = 0.25 - 0.30$, a temperature of $\Delta T = 0°\text{C}$, and two optimization algorithms: (a) and (b) utilize the MMA optimizer, while (c) and (d) show results for the GCMMA optimizer.

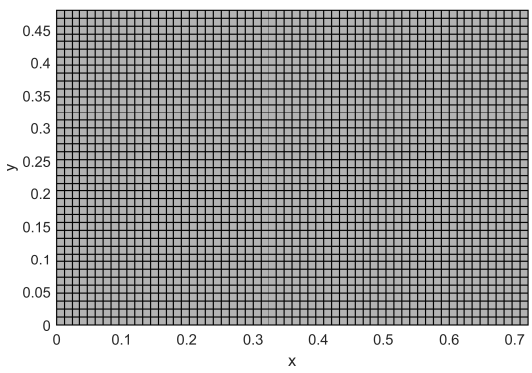

(a) Density distribution

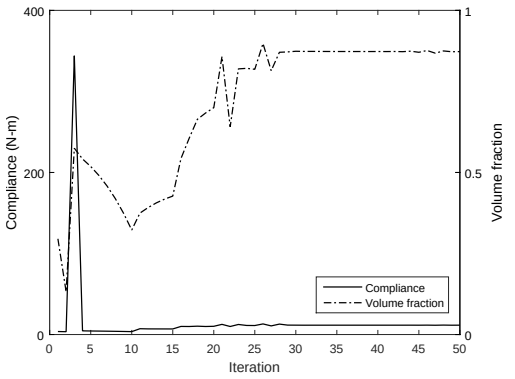

(b) Iteration history

Figure 4.4: Optimized designs and iteration history plots for combined thermal and mechanical loading utilizing the MMA algorithm, $\Delta T = 1°\text{C}$, and $V_f = 0.25 - 0.30$.

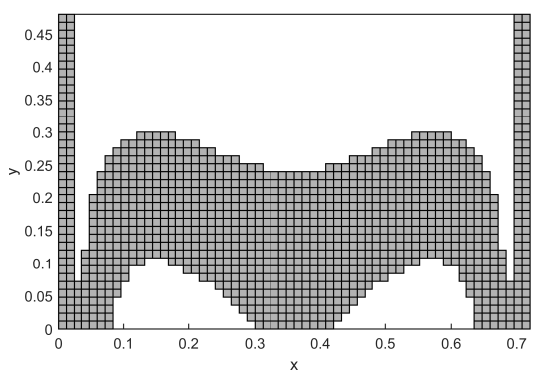

(a) Density distribution: $\Delta T = 1°C$

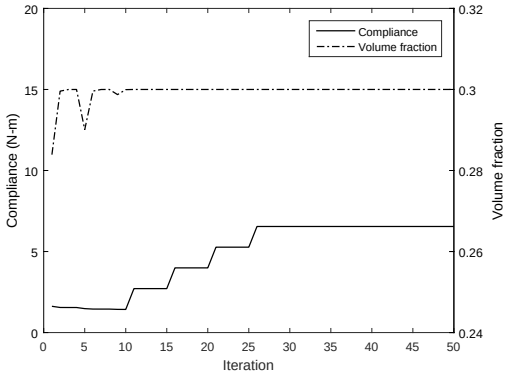

(b) Iteration history: $\Delta T = 1°C$

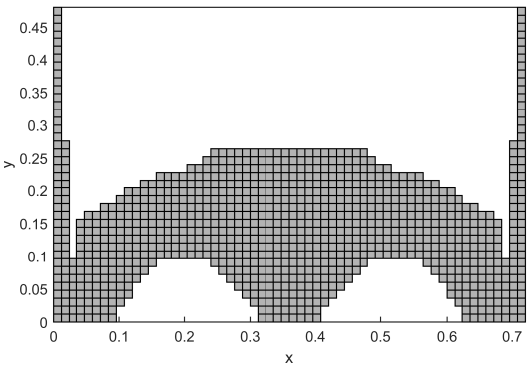

(c) Density distribution: $\Delta T = 3°C$

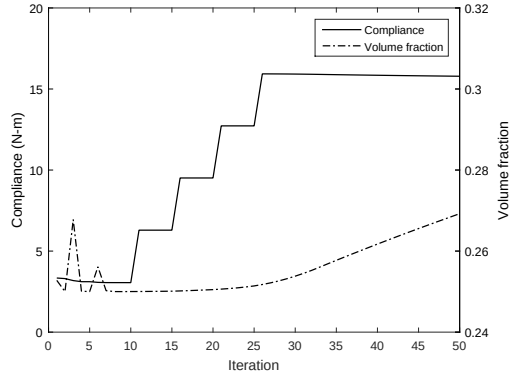

(d) Iteration history: $\Delta T = 3°C$

Figure 4.5: Optimized designs and iteration history plots for combined thermal and mechanical loading, using the GCMMA algorithm, a volume fraction of $V_f = 0.25 - 0.30$, and two temperature cases: (a) and (b) consider $\Delta T = 1°C$, while (c) and (d) consider a temperature change of $\Delta T = 3°C$.

reasons for other discrepancies in the results could be due to 3D rather than 2D analysis, the choice of filter, filter radius, and internal parameters. We also note that Deaton & Grandhi (2013b) and Bruyneel & Duysinx (2005) reported success using the MMA for this thermoelastic problem by employing robust move limits.

4.4 Topology optimization of the anode structure

We now apply this minimum compliance formulation to the design problem of a lithiated silicon anode in a Li-ion battery. The loading, boundary conditions and problem parameters are first presented, followed by the results of the optimization problem. The iteration history, mesh independence, influence of volume fraction, and minimum length scale are all investigated. The average von Mises stress values are compared for different designs, and as a final validation the problem is also solved using a minimum elastic strain energy formulation.

4.4.1 Loading and boundary conditions

The volume expansion of the structure due to lithiation is modelled in the same way as volume expansion due to thermal loading. Therefore, the volumetric strain variable $\epsilon^*(\tilde{x}_e)$ is assigned values to represent a 300% change in volume in the anode due to lithiation, while no volume change is applied to the electrolyte,

$$\epsilon^*(\tilde{x}_e) = \begin{cases} 1 & \text{when } \tilde{x}_e = 1 \text{ (anode)}, \\ 0 & \text{when } \tilde{x}_e = 0 \text{ (electrolyte)}. \end{cases} \tag{4.23}$$

The above equation clearly illustrates the design dependent nature of this problem. The volume expansion will therefore be a function of element density, which is interpolated between the values for the anode and the electrolyte.

The design domain representing the anode structure is depicted in Figure 4.6a. The bottom face of the anode is rigidly fixed to the substrate, while the sides are constrained by battery packaging and reinforcement. This is a common choice of boundary conditions when modelling electrodes and is typically called the "manufacturing condition" as it represents the entire battery system being constrained by the outer casing (Aifantis et al., 2010).

We consider a 5 μm x 5 μm x 5 μm cubic base cell which is periodic in the x-z plane and discretized into finite elements (Figure 4.6b). The base cell size was chosen such that it was consistent with dimensions used by experimentalists who work with silicon anode structures (Baggetto et al., 2011, 2008; He et al., 2012). With respect to the base cell, the boundary conditions are a fixed bottom face, sliding conditions on the side faces, and a free top face. Symmetry is a characteristic feature of the solution, therefore sliding boundary conditions are deemed to be an acceptable alternative to implementing periodic boundary conditions.

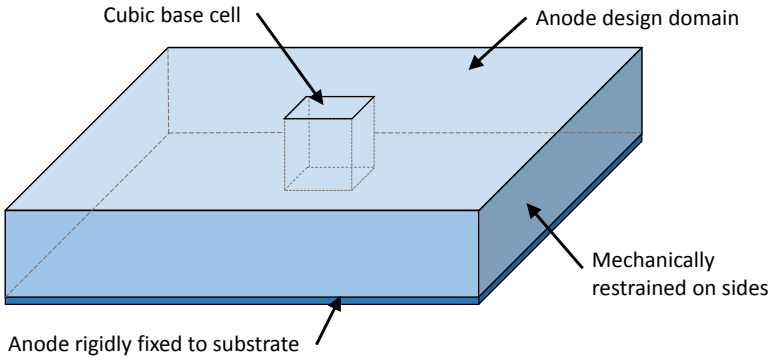

(a) Anode design domain

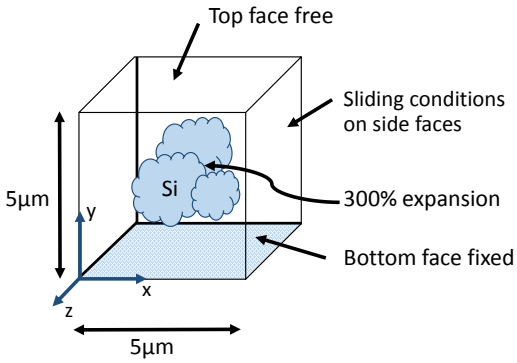

(b) Periodic base cell

Figure 4.6: Schematic of design domain and boundary conditions.

4.4.2 Problem parameters

In these analyses we consider two material phases: the anode and the electrolyte. For the anode, the material properties of a-$Li_{15}Si_4$ are used. The Young's modulus and Poisson's ratios are set to values of $E_{anode} = 35$ GPa and $\nu = 0.23$, respectively (Shenoy et al., 2010). During the first discharge of Li-Si at room temperature, crystalline silicon becomes amorphous Li_xSi (Li & Dahn, 2007; Obrovac & Christensen, 2004). As lithiation progresses, various amorphous phases of increasing lithium concentration are formed until the anode is fully lithiated. The material properties, such as Young's modulus and Poisson's ratio are therefore functions of lithium concentration. If the electrode is exposed to voltages less than 50 mV the crystalline $Li_{15}Si_4$ phase forms upon full lithiation, while if the cycling is limited to above 50 mV the structure will remain amorphous (Li & Dahn, 2007; Obrovac & Christensen, 2004). The greatest change in volume is associated with the final phase transition (Kang et al., 2009),

and therefore in our analyses we use the material properties of a-$Li_{15}Si_4$. The other phase representing the electrolyte is modelled as void, which is a common practice in many topology optimization problems. As such, the Young's modulus of the electrolyte is set to a very small number not equal to zero in order to prevent singularities, i.e., $E_{electrolyte} = 1\text{x}10^{-3}$ GPa.

The desired volume fraction of the silicon anode material is $V_f = 0.3$, or 30% of the total design domain volume. This volume fraction was chosen to ensure there was adequate porosity of the structure, whilst also maintaining sufficient active material to achieve the required electrochemical performance of the battery. The desired volume fraction is set to be the lower bound on volume, while the upper bound is set to be 0.1 or 10% greater than the lower bound. This is because the minimum compliance objective will drive the solution to the lowest allowable volume. The initial density distribution is therefore set to the upper bound in each element.

The RAMP interpolation is used for both the Young's modulus $E(\tilde{x}_e)$ and the volume expansion coefficient $\gamma(\tilde{x}_e)$, with maximum penalty values of $p = 8$. To prevent numerical difficulties such as mesh dependence, and to impose a minimum length scale, density filtering is employed with a filter radius of r = 2 μm. We utilize the GCMMA method to determine the updated densities on each iteration.

4.4.3 Results

Figure 4.7 depicts the optimized anode structure. The structure may be considered a periodic array of base cells, and resembles a series of solid cubes that have been hollowed out by spherical shapes. Two different base cells are depicted in Figures 4.7b and 4.7c which result in the same final structure. It is interesting to note that the optimal structure shows some resemblance to the Schwarz P surface, which has been reported as an optimal solution for other topology optimization problems as detailed in Chapters 2.4 and 2.5, such as maximum conductivity, permeability, and bulk modulus objectives.

The iteration history for the compliance and volume fraction are shown in Figure 4.8. It can be seen that the volume fraction quickly drops to the lower bound of 30%, while the compliance steps down with increasing interpolation penalty and converges to the final solution of $c = 4.8726$ x 10^{-6} Nm within 60 iterations.

Mesh independence was tested to ensure that the design remained consistent for different numbers of elements. Figure 4.9 shows the element density distribution for different domain

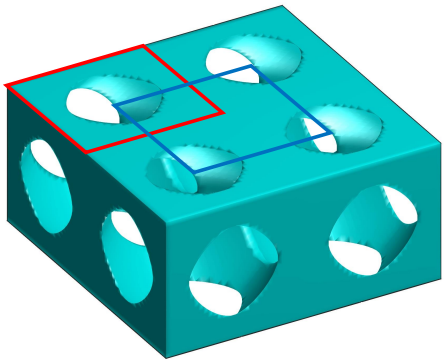

(a) 2 x 2 base cells

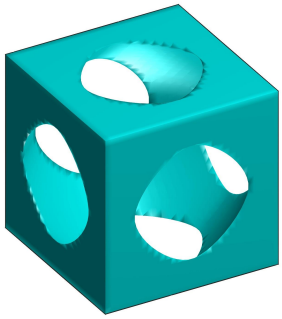

(b) Red base cell

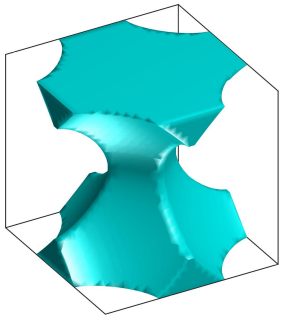

(c) Blue base cell

Figure 4.7: Optimized anode structure for $V_f = 0.3$.

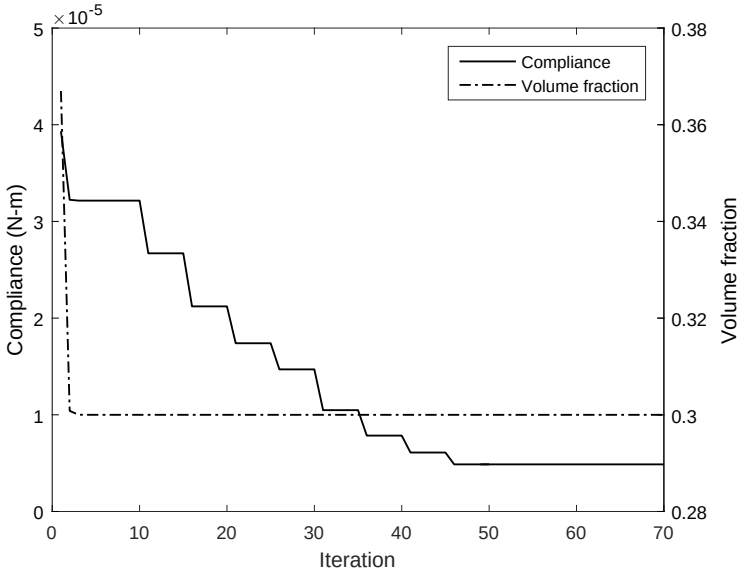

Figure 4.8: Compliance and volume fraction as a function of iterations.

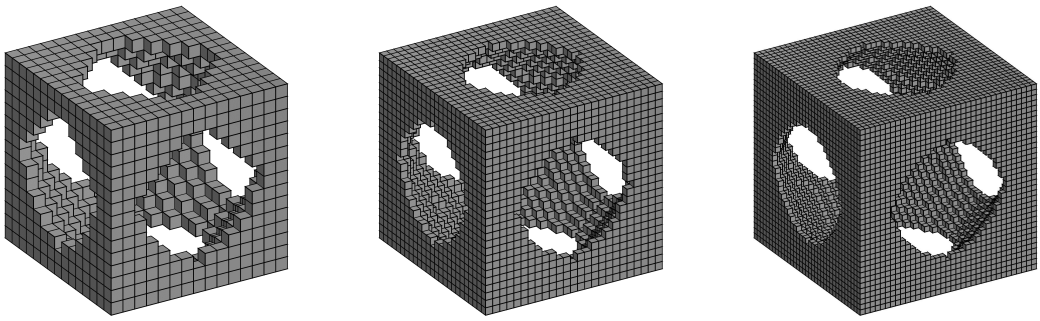

(a) 15 x 15 x 15 elements (b) 25 x 25 x 25 elements (c) 35 x 35 x 35 elements

Figure 4.9: Optimized structure for varying numbers of elements.

discretizations. The optimized structure is consistent for each discretization, and therefore the results are considered mesh independent. As such, unless otherwise stated, the results presented in this chapter are for a design domain discretized into 30 x 30 x 30 elements. This was deemed to be a fair compromise between design detail and computational efficiency.

Figure 4.10 depicts the deformed structure for a volume fraction of $V_f = 0.3$, where the blue horizontal line represents the top of the undeformed base cell. Recall the boundary conditions of Figure 4.6, where the periodic base cell is rigidly fixed to the substrate, restrained on the sides with sliding conditions, and has free expansion on the top face. Therefore, the struts swell to fill the central void while the entire structure expands in the vertical direction.

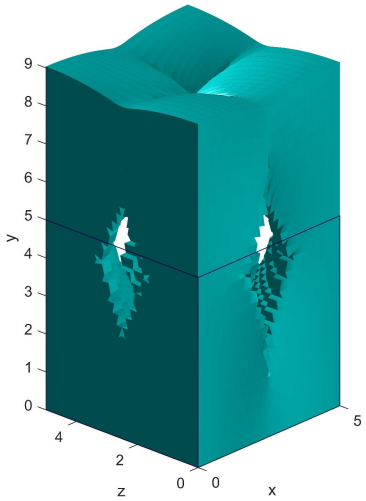

Figure 4.10: Deformed structure, blue horizontal line represents the top of the undeformed base cell.

A selection of volume fractions were tested to ensure the solution remained well behaved, and to assess the effect of changing the limit of allowable material. Figure 4.11 shows that increasing the volume fraction simply results in the thickening of the struts, thereby reducing the size of the center spherical hollow. A plot of the associated compliance values depicted in Figure 4.12 shows that the compliance decreases with decreasing volume fraction. This is because less material in the structure means more voids to accommodate the volume expansion of the silicon and therefore results in lower stresses and hence a lower compliance. However, a trade-off is required as the anode must have sufficient active material to achieve the desired electrochemical performance, and therefore a volume fraction of $v_f = 0.3$ is recommended.

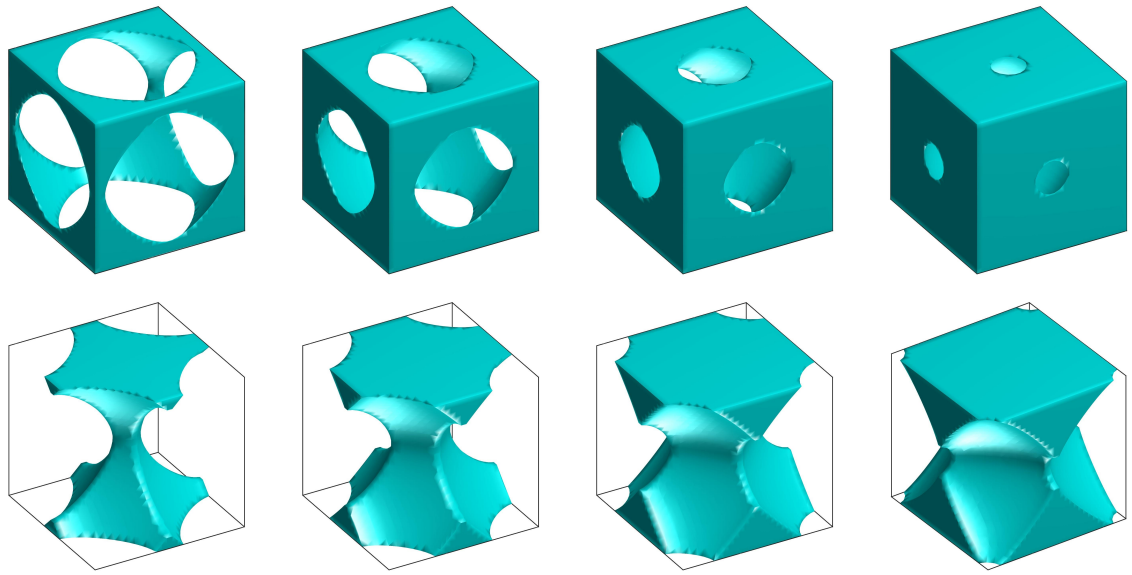

(a) $V_f = 0.15$ (b) $V_f = 0.30$ (c) $V_f = 0.45$ (d) $V_f = 0.60$

Figure 4.11: Optimized base cell structures for varying volume fractions. The top row depicts the original base cell, while the bottom row shows the shifted base cells.

4.4.3.1 Influence of minimum length scale

During the parameter investigation stage, the effect of reducing the minimum length scale was also considered. The minimum length scale of the design is dependent on the comparative values of the filter radius, domain size, and the number of elements. Keeping the domain size and number of elements constant, the filter radius r becomes the dominant length scale parameter. As detailed in Chapter 3.7.2, the density filter modifies each element's density to be a weighted average of the neighboring elements' densities within r. Up to this point, results

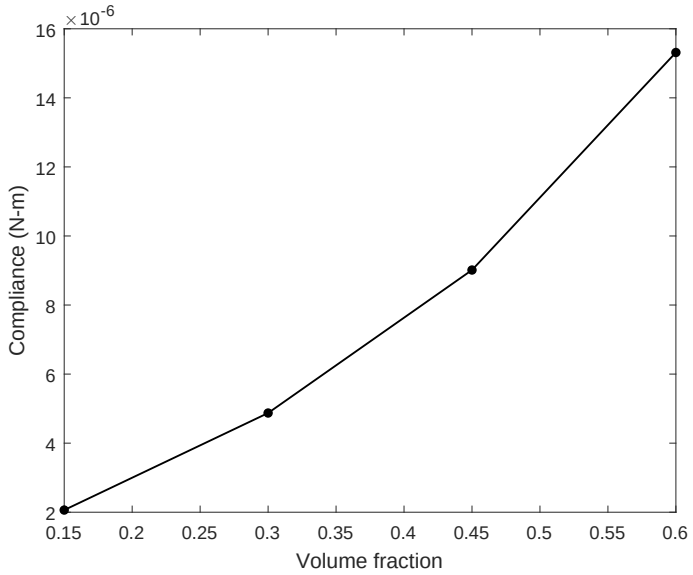

Figure 4.12: Compliance as a function of prescribed volume fraction.

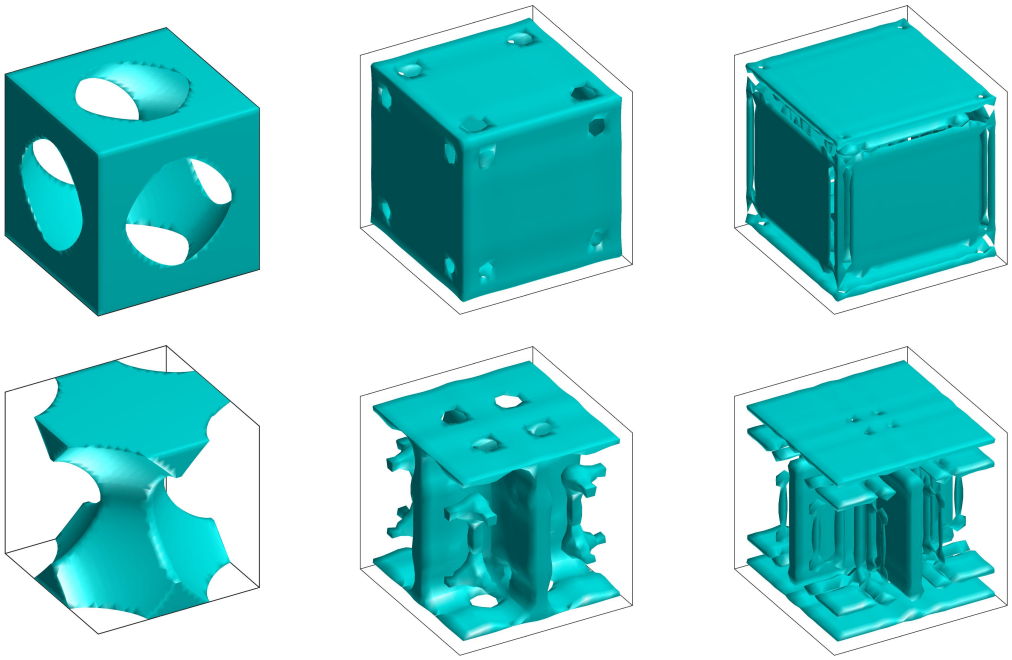

(a) r = 2μm (b) r = 1μm (c) r = 0.5μm

Figure 4.13: Optimized base cells for different filter radii, (a) r = 2 μm, (b) r = 1 μm, (c) r = 0.5 μm. The top row depicts the original base cell, while the bottom row shows the shifted base cells.

are shown for a radius of r = 2 μm. The designs for r = 2 μm, r = 1 μm and r = 0.5 μm are depicted in Figure 4.13. Both the original base cells (top row), and the displaced base cells (bottom row) are shown for clarity.

When comparing the r = 1 μm structure to the original r = 2 μm design, the major changes include four small corner holes on each face rather than one large central hole, which results in the vertical struts spanning the entire face of the base cells, and the appearance of an internal floating structure that resembles a wire-frame cube. In terms of the objective function we calculate a small 1.2% reduction in compliance relative to the r = 2 μm design which indicates a slightly better performance, possibly due to the internal structure being free to expand in all directions within the central void space, thereby reducing the average stress. However the free-floating nature of the internal structure introduces manufacturability challenges, particularly when considering a liquid electrolyte. A further reduction of the filter radius to r = 0.5 μm results in a very fragmented structure. The side faces have now become disconnected vertical plates, and the internal structure has become a series of floating plates and rods. This design has severe manufacturing limitations, and also exhibits a compliance value 2.9% greater than the r = 2 μm structure which is likely due to the fragmented nature of the design. The design requirement of a connected structure necessitates the choice of the r = 2 μm design to be the best solution for this application.

4.4.3.2 Comparison of average von Mises stress values

We now investigate whether the minimum compliance objective does indeed minimize an average measure of stress by computing the average von Mises stress in the structure. The stress vector for a solid element e may be expressed as

$$\begin{aligned} \boldsymbol{\sigma}_e &= \left[\sigma_{xx},\ \sigma_{yy},\ \sigma_{zz},\ \tau_{xy},\ \tau_{yz},\ \tau_{xz}\right] \\ &= \mathbf{C}_e\ \boldsymbol{\epsilon}^m \\ &= \mathbf{C}_e(\boldsymbol{\epsilon} - \boldsymbol{\epsilon}^*) \\ &= E_{anode}\bar{\mathbf{C}}_e\mathbf{B}_e\mathbf{d}_e - E_{anode}\bar{\mathbf{C}}_e\epsilon^*\ \boldsymbol{\phi}^T, \end{aligned} \tag{4.24}$$

where $\boldsymbol{\epsilon}^m$, $\boldsymbol{\epsilon}^v$, and $\boldsymbol{\epsilon}$ are the mechanical, thermal, and total strains, respectively. E_{anode} is the Young's modulus of the anode material, $\bar{\mathbf{C}}_e$ is the constitutive matrix for a unit Young's modulus, $\mathbf{B}_e$ is the element strain-displacement matrix, $\mathbf{d}_e$ is the element displacement vector,

α the coefficient of thermal expansion of the silicon anode, and ΔT the temperature change applied to the anode. The element stress is calculated as the average of the values at the quadrature points. The von Mises failure criterion combines the principal stresses into an equivalent applied stress, and may be computed from the element stress vector

$$\sigma_e^{VM} = \sqrt{\frac{1}{2}\Big[(\sigma_{xx} - \sigma_{yy})^2 + (\sigma_{yy} - \sigma_{zz})^2 + (\sigma_{zz} - \sigma_{xx})^2\Big] + 3(\tau_{xy}^2 + \tau_{yz}^2 + \tau_{zx}^2)}. \tag{4.25}$$

The von Mises stress distribution is plotted in Figure 4.14. As expected, there is high stress in the thinnest section of the struts in the constrained directions, and stress concentrations may be observed at the edges of the holes. These stress concentrations could be reduced with localized mesh refinement and a further shape optimization step (Pedersen & Pedersen, 2008).

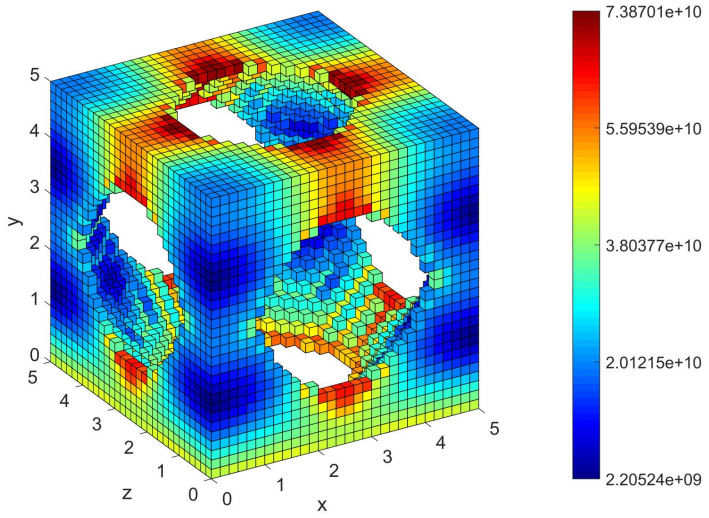

Figure 4.14: The von Mises stress distribution plotted on the undeformed base cell, $V_f = 0.30$.

If we compare the values to a yield stress in nano silicon of 11.06 GPa (Yang et al., 2009), it is clear that the plotted values are reasonably high and that some of the structure has undergone plastic deformation, which has been observed experimentally with other silicon anode structures (Liang et al., 2014; Sethuraman et al., 2010). The large stress values are to be expected as our analysis assumed linear elasticity, and therefore in reality any stress above the yield stress would be significantly lower than is reported here. Furthermore, we are applying a large thermal strain simulating full lithiation of the anode. Reaching a fully lithiated state is highly dependent on battery operating conditions, such as the voltage range within

which the batteries are cycled. Reducing the voltage range prevents full lithiation/delithiation but will greatly improve cycling stability (Zhang, 2011). As such, full lithiation may not take place for practical electrochemical cells, resulting in lower stress values.

Despite the small-strain and full lithiation assumptions and the resulting large stress values, this analysis can adequately capture the lithiation behaviour and produce optimal designs. For example, when analyzing the average von Mises stress of the optimal structures for different volume fractions, depicted in Figure 4.11, it has been observed that a larger volume fraction results in a larger average von Mises stress. When compared to the $V_f = 0.30$ design, there is a 6.4% and a 16.2% increase in average von Mises stress for a prescribed volume fraction of $V_f = 0.45$ and $V_f = 0.60$, respectively. Figure 4.12 shows that the compliance increases for the larger volume fractions, and therefore it may be inferred that the design objective of minimizing the compliance will result in a structure that minimizes the average stress. This is further illustrated by computing the average von Mises stress for a 5 μm x 5 μm x 1.5 μm base cell composed of homogeneous material, where the material volume is equal to 30% of the original design domain. It was found that the average von Mises stress in the block of material upon lithiation was 42.7% greater than the average von Mises stress for the optimized design with a $V_f = 0.30$.

4.4.3.3 Comparison to minimum elastic strain energy formulation

For design independent loads and a constraint on volume, minimum compliance and maximum strength objectives lead to the same optimal design (Kohn & Wirth, 2014; Pedersen & Pedersen, 2012). However, Pedersen & Pedersen (2010a, 2012) questioned validity of using the minimum compliance formulation to obtain a strength optimized design when using thermoelastic loading, and recommended performing strength optimization using a minimum elastic strain energy or uniform energy density objective. As an extra validation of our results, and to confirm that minimizing the compliance leads to maximum strength for the particular loading and boundary conditions of this problem, the minimum elastic strain energy objective was implemented and results are compared to those presented above.

Problem Formulation. The elastic strain energy Φ may be defined as the potential mechanical energy stored in an elastic body as work is performed to distort the structure's volume or

shape (Zhang et al., 2014). Recall the constitutive law for linear thermoelasticity

$$\begin{aligned}\sigma_{ij}(u) &= \mathbf{C}_{ijkl}(x)(\epsilon_{kl}(u) - \epsilon^*_{kl}(x)), \\ &= \mathbf{C}_{ijkl}(x)(\epsilon_{kl}(u) - \alpha_{kl}(x)\Delta T).\end{aligned} \tag{4.26}$$

In indicial notation, the elastic strain energy is given by

$$\Phi(u) = \frac{1}{2}\int_\Omega \mathbf{C}_{ijkl}(x)(\epsilon_{ij}(u) - \epsilon^*_{kl}(x))(\epsilon_{ij}(u) - \epsilon^*_{kl}(x))\ d\Omega,$$

or equivalently,

$$\begin{aligned}\Phi &= \frac{1}{2}\int_\Omega (\boldsymbol{\epsilon} - \boldsymbol{\epsilon}^*)^T \mathbf{C}(\boldsymbol{\epsilon} - \boldsymbol{\epsilon}^*)\ d\Omega \\ &= \frac{1}{2}\int_\Omega \boldsymbol{\epsilon}^T \mathbf{C}\boldsymbol{\epsilon}\ d\Omega - \int_\Omega \boldsymbol{\epsilon}^T \mathbf{C}\boldsymbol{\epsilon}^*\ d\Omega + \frac{1}{2}\int_\Omega (\boldsymbol{\epsilon}^*)^T \mathbf{C}\boldsymbol{\epsilon}^*\ d\Omega \\ &= \frac{1}{2}\int_\Omega \boldsymbol{\epsilon}^T \mathbf{C}\boldsymbol{\epsilon}\ d\Omega - \int_\Omega \boldsymbol{\epsilon}^T \mathbf{C}\boldsymbol{\epsilon}^*\ d\Omega + \Phi^*,\end{aligned} \tag{4.27}$$

where $\boldsymbol{\epsilon}$, and $\boldsymbol{\epsilon}^*$ represent the total and volumetric strains, respectively. The third term Φ^* represents the energy generated by the initial thermal or volumetric strain. Equation 4.27 may be expressed in a discrete form

$$\begin{aligned}\Phi(\tilde{\mathbf{x}}) &= \frac{1}{2}\mathbf{U}(\tilde{\mathbf{x}})^T \mathbf{K}(\tilde{\mathbf{x}})\mathbf{U}(\tilde{\mathbf{x}}) - \mathbf{U}(\tilde{\mathbf{x}})^T \mathbf{F}^v(\tilde{\mathbf{x}}) + \Phi^*(\tilde{\mathbf{x}}) \\ &= \frac{1}{2}c(\tilde{\mathbf{x}}) - \mathbf{U}(\tilde{\mathbf{x}})^T \mathbf{F}^v(\tilde{\mathbf{x}}) + \Phi^*(\tilde{\mathbf{x}}),\end{aligned} \tag{4.28}$$

where $c(\tilde{\mathbf{x}})$ is the compliance from Equation 4.3, and $\mathbf{F}^v$ is the global volumetric load vector is assembled from the element contributions given by Equation 4.11, while $\Phi^*(\tilde{\mathbf{x}})$ is given by

$$\begin{aligned}\Phi^*(\tilde{\mathbf{x}}) &= \frac{1}{2}\Big(\alpha(\tilde{x}_e)\Big)^2\Big(\Delta T(\tilde{x}_e)\Big)^2 \int_{\Omega_e} \boldsymbol{\phi}\ \mathbf{C}_e(\tilde{x}_e)\ \boldsymbol{\phi}^T\ d\Omega \\ &= \frac{1}{2}E_e(\tilde{x}_e)\Big(\alpha(\tilde{x}_e)\Big)^2\Big(\Delta T(\tilde{x}_e)\Big)^2 \int_{\Omega_e} \boldsymbol{\phi}\ \bar{\mathbf{C}}_e\ \boldsymbol{\phi}^T\ d\Omega \\ &= \frac{1}{2}\frac{\Big(\gamma(\tilde{x}_e)\Big)^2}{E_e(\tilde{x}_e)} \int_{\Omega_e} \boldsymbol{\phi}\ \bar{\mathbf{C}}_e\ \boldsymbol{\phi}^T\ d\Omega \\ &= \frac{\Big(\gamma(\tilde{x}_e)\Big)^2}{E_e(\tilde{x}_e)}\bar{\Phi}^*,\end{aligned} \tag{4.29}$$

where

$$\bar{\Phi}^* = \frac{1}{2}\int_{\Omega_e} \boldsymbol{\phi}\ \bar{\mathbf{C}}_e\ \boldsymbol{\phi}^T\ d\Omega. \tag{4.30}$$

The optimization problem formulation with a minimum strain energy objective is

$$\begin{aligned} \min_x: \quad & \Phi(\tilde{\mathbf{x}}) = \frac{1}{2}c(\tilde{\mathbf{x}}) - \mathbf{U}(\tilde{\mathbf{x}})^T\mathbf{F}^v(\tilde{\mathbf{x}}) + \Phi^*(\tilde{\mathbf{x}}) \\ \text{subject to}: \quad & V_f^{min} \leq \frac{V(\tilde{\mathbf{x}})}{V_0} \leq V_f^{max}, \\ & \mathbf{K}(\tilde{\mathbf{x}})\mathbf{U}(\tilde{\mathbf{x}}) = \mathbf{F}^m + \mathbf{F}^v(\tilde{\mathbf{x}}), \\ & \mathbf{0} \leq \mathbf{x} \leq \mathbf{1}. \end{aligned} \tag{4.31}$$

Sensitivity Analysis. For the particular case of the anode structure, there is zero mechanical loading thus the equilibrium equation may be expressed as

$$\mathbf{K}(\tilde{\mathbf{x}})\mathbf{U}(\tilde{\mathbf{x}}) = \mathbf{F}^v(\tilde{\mathbf{x}}), \tag{4.32}$$

leading to a simplified expression for $\Phi(\tilde{\mathbf{x}})$

$$\Phi(\tilde{\mathbf{x}}) = -\frac{1}{2}c(\tilde{\mathbf{x}}) + \Phi^*(\tilde{\mathbf{x}}).$$

Given the derivative of compliance in Equation 4.18 and the expression for the initial strain energy (Equation 4.29), the derivative of the strain energy with respect to element density is

$$\begin{aligned} \frac{\partial\Phi(\tilde{\mathbf{x}})}{\partial\tilde{x}_e} &= -\frac{1}{2}\frac{\partial c(\tilde{\mathbf{x}})}{\partial\tilde{x}_e} + \frac{\partial\Phi^*(\tilde{\mathbf{x}})}{\partial\tilde{x}_e} \\ &= -\mathbf{U}^T(\tilde{\mathbf{x}})\frac{\partial\mathbf{F}^v(\tilde{\mathbf{x}})}{\partial\tilde{x}_e} + \frac{1}{2}\mathbf{U}(\tilde{\mathbf{x}})^T\frac{\partial\mathbf{K}(\tilde{\mathbf{x}})}{\partial\tilde{x}_e}\mathbf{U}(\tilde{\mathbf{x}}) + \frac{\partial}{\partial\tilde{x}_e}\left(\frac{\left(\gamma(\tilde{x}_e)\right)^2}{E_e(\tilde{x}_e)}\right)\bar{\Phi}^*. \end{aligned} \tag{4.33}$$

Relation to Stress. Substituting the stress-strain relation $\boldsymbol{\sigma} = \mathbf{C}(\boldsymbol{\epsilon} - \boldsymbol{\epsilon}^*)$ into Equation 4.27, the strain energy may be expressed in terms of stress,

$$\begin{aligned} \Phi &= \frac{1}{2}\int_\Omega (\boldsymbol{\epsilon} - \boldsymbol{\epsilon}^*)^T\mathbf{C}(\boldsymbol{\epsilon} - \boldsymbol{\epsilon}^*)\ d\Omega \\ &= \frac{1}{2}\int_\Omega \boldsymbol{\sigma}^T\mathbf{C}\boldsymbol{\sigma}\ d\Omega. \end{aligned} \tag{4.34}$$

It is clear that minimizing the strain energy will effectively minimize a measure of stress in the structure and therefore produce a strength optimized design.

Results. The results are almost identical to that obtained by minimum compliance. The optimized structure for a volume fraction of $V_f = 0.3$ is given in Figure 4.15, while Table 4.1 compares the compliance and strain energy values for both objectives. As expected, the minimum compliance objective provides the lowest compliance value, while the minimum strain energy objective provides the lowest value of strain energy, but ultimately the difference is almost negligible. It may be concluded that for this problem a minimum compliance objective successfully minimizes both a global measure of deformation and stress.

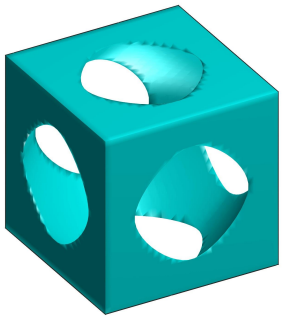

Figure 4.15: Optimal solution for a minimum strain energy objective.

Table 4.1: Table comparing compliance and strain energy values

	Min compliance objective	Min strain energy objective	% Difference
Compliance	4.873 x 10^{-6} Nm	4.836 x 10^{-6} Nm	-0.76 %
Strain energy	1.278 x 10^{-6} Nm	1.248 x 10^{-6} Nm	2.3 %

4.5 Summary

This chapter aimed to produce a topology optimized silicon anode structure that would better withstand the detrimental effects of lithiation processes. The anode design problem was formulated using a minimum compliance objective function, with design dependent volume ex-

pansion due to lithiation. The volume expansion was modelled using the same equations as expansion due to thermal loading. The problem formulation was first presented, followed by a discussion of the key numerical difficulties associated with design dependent topology optimization problems, namely convergence failure, singular behaviour, and an inactive volume constraint. Remedies to overcome these issues were introduced and further illustrated using a benchmark thermoelastic problem involving a bi-clamped beam subject to both mechanical and thermal loading. The detailed optimization and analysis of the silicon anode structure was subsequently presented. The optimal silicon anode structure featured a cube of anode material with a hollowed sphere-like core representing the electrolyte. This structure resembled the Schwarz P-type structures that have also been obtained for topology optimization problems in other fields. The iteration history, mesh independence, influence of volume fraction and minimum length scale were all investigated. It was found that smaller length scales introduced manufacturing difficulties due to the optimal designs lacking connectivity. The von Mises stress distribution was presented, and average values compared for different anode designs. These results indicated a significantly improved mechanical performance for the optimal design relative to a homogeneous anode structure of equivalent volume. Finally, equivalence of results was shown for the minimum compliance and minimum elastic strain energy formulations for this particular design problem.

Chapter 5

Maximizing Electrical Conduction

In this chapter we explore the design objective of maximizing the electrical conduction of the silicon anode. It is crucial to optimize the anode structure for this objective in order for the design to exhibit efficient electronic pathways, particularly when considering the low electrical conductivity of silicon. An anode structure that maximizes electrical conduction will generate improved battery capacity and rate capability. The governing equations for heat and electric conduction are analogous, and therefore the problem formulation for maximizing heat conduction and a benchmark test case involving a heat sink are first presented. Subsequently, the anode structure is optimized for maximum electrical conduction.

5.1 Problem Formulation

First, let us consider the problem of steady-state heat conduction with no convective heat transfer. Figure 5.1 depicts a body defined by the volume Ω and outer surface Γ, which is subjected to a prescribed temperature distribution T^* on part of the boundary Γ_T, and the normal heat flux q^* is prescribed on the boundary Γ_q,

$$T = T^* \qquad \text{on } \Gamma_T, \tag{5.1}$$

$$\mathbf{q} \cdot \mathbf{n} = q^* \qquad \text{on } \Gamma_q. \tag{5.2}$$

The governing partial differential equation for steady-state heat conduction is

$$\boldsymbol{\nabla}^T (\mathbf{D} \boldsymbol{\nabla} T) + S = 0, \tag{5.3}$$

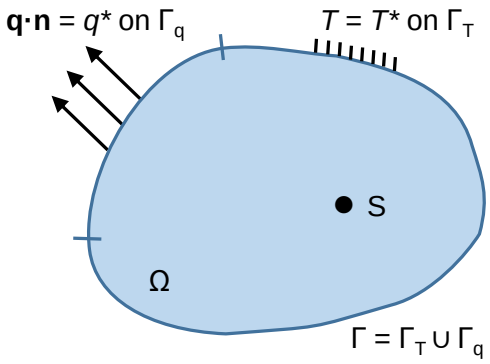

Figure 5.1: The reference domain with a prescribed temperature and heat flux on the boundary, and an internal heat source.

or equivalently in its variational form

$$\int_{\Omega} \nabla W \cdot (\mathbf{D} \nabla T)\, \mathrm{d}\Omega + \int_{\Gamma_q} W q^* \, \mathrm{d}\Gamma - \int_{\Omega} W S \, \mathrm{d}\Omega = 0, \tag{5.4}$$

where $\mathbf{D}$ is the conductivity tensor, S is the internal heat generation, and W is a weight function. Further details, including the derivation of the strong form, weak form, and the finite element approximation may be found in Appendix B. This governing equation, also known as Poisson's equation, may be used to describe various physics problems by making appropriate parameter substitutions, as shown in Table 5.1 (Donoso & Sigmund, 2004; Huebner et al., 2001; Kohn & Strang, 1986b).

Table 5.1: Physical interpretation of equation parameters

Problem	T	$\mathbf{D}$	S	q
Heat conduction	Temperature	Thermal conductivity	Internal heat generation	Boundary heat flux
Electric conduction	Voltage	Electric conductivity	Internal current source	Boundary current
Diffusion flow	Hydraulic head	Permeability	Internal source flow	Boundary flow
Electro-statics	Electrostatic potential	Permittivity	Internal charge density	Electric field
Magneto-statics	Magnetic vector	Medium's response	Internal current density	Magnetic field

The objective of maximizing heat conduction or electricity may be considered the scalar version of the minimum compliance problem formulation (Kohn & Wirth, 2014). As such, the objective function is often referred to as the thermal or electrical compliance. This objective may be expressed in variational form as

$$\min_{T\in\mathbb{T},\rho} : \quad l(T) \tag{5.5}$$

$$\begin{aligned} \text{subject to} : \quad & a(T,W) = l(W), \quad \text{for all } W \in \mathbb{T}, \\ & \int_\Omega \rho(x)\ d\Omega \leq V_f, \\ & \rho(x) \in \{0,1\}, \end{aligned} \tag{5.6}$$

where

$$a(T,W) = \int_\Omega \boldsymbol{\nabla} W \cdot (\mathbf{D}\boldsymbol{\nabla} T)\ \mathrm{d}\Omega, \tag{5.7}$$

$$l(W) = \int_\Omega W S\,\mathrm{d}\Omega - \int_{\Gamma_q} W q^*\,\mathrm{d}\Gamma, \tag{5.8}$$

and $\mathbb{T}$ denotes the space of kinematically admissible temperature fields, x is a point within the domain Ω, $\rho(x)$ is the pointwise volume fraction, and V_f is the upper bound on material volume fraction. Using a finite element discretization, the maximum heat conduction objective may be expressed as

$$\min_{x} : \quad c(\tilde{\mathbf{x}}) = \mathbf{T}(\tilde{\mathbf{x}})^{\mathsf{T}}\mathbf{K}(\tilde{\mathbf{x}})\mathbf{T}(\tilde{\mathbf{x}}) \tag{5.9}$$

$$\begin{aligned} \text{subject to} : \quad & \mathbf{K}(\tilde{\mathbf{x}})\mathbf{T}(\tilde{\mathbf{x}}) = \mathbf{F} = \mathbf{F}_q + \mathbf{F}_S, \\ & \frac{V(\tilde{\mathbf{x}})}{V_0} \leq V_f^{max}, \\ & \mathbf{0} \leq \mathbf{x} \leq \mathbf{1}, \end{aligned}$$

where $c(\tilde{\mathbf{x}})$ is the thermal compliance, which may be considered as an average measure of temperature within the design domain. Minimizing this objective corresponds to maximizing the heat conduction. $\mathbf{T}(\tilde{\mathbf{x}})$ is the global temperature vector, $\mathbf{K}(\tilde{\mathbf{x}})$ is the global conductance matrix, $\mathbf{F}$ is the design independent global thermal load vector comprised of both flux and source terms, $V(\tilde{\mathbf{x}}) = \sum_{e=1}^{N} \tilde{x}_e v_e$ is the material volume, V_0 is the design domain volume, and V_f is the prescribed volume fraction. The conductance matrix and thermal load vector are

assembled from their element contributions as follows:

$$\mathbf{k}_e(\tilde{x}_e) = \int_{\Omega_e} \mathbf{B}_e^T \mathbf{D}_e(\tilde{x}_e) \mathbf{B}_e \, \mathrm{d}\Omega, \tag{5.10}$$

where $\mathbf{B}_e$ contains the shape function derivatives and $\mathbf{D}_e(\tilde{x}_e)$ is the element conductivity matrix comprised of the thermal conductivity values as a function of material density. For an isotropic material, this is given by

$$\mathbf{D}_e(\tilde{x}_e) = d_e(\tilde{x}_e)\mathbf{I}, \tag{5.11}$$

where $d_e(\tilde{x}_e)$ is the element's conductivity as a function of element density, and $\mathbf{I}$ is a 3x3 identity matrix. Therefore, the element conductance matrix may be written as

$$\begin{aligned} \mathbf{k}_e(\tilde{x}_e) &= d_e(\tilde{x}_e) \int_{\Omega_e} \mathbf{B}_e^T \mathbf{I} \mathbf{B}_e \, \mathrm{d}\Omega \\ &= d_e(\tilde{x}_e) \bar{\mathbf{k}}_e, \end{aligned} \tag{5.12}$$

where $\bar{\mathbf{k}}_e$ is the element conductance for a unit thermal conductivity. The element thermal load vector is given by

$$\begin{aligned} \mathbf{f}_e &= \mathbf{f}_e^q + \mathbf{f}_e^s \\ &= -\int_{\Gamma_e^q} \mathbf{N}_e{}^T q^* \, \mathrm{d}\Gamma + \int_{\Omega_e} \mathbf{N}_e{}^T S \, \mathrm{d}\Omega. \end{aligned} \tag{5.13}$$

5.1.1 Sensitivity Analysis.

The sensitivity of the conduction objective is analogous to that provided in Equation 3.20 for the design independent linear elastic problem. The derivative of the thermal compliance with respect to physical element densities $\tilde{x}_e$ is

$$\frac{\partial c(\tilde{\mathbf{x}})}{\partial \tilde{x}_e} = -\mathbf{t}_e(\tilde{x}_e)^T \frac{\partial \mathbf{k}_e(\tilde{x}_e)}{\partial \tilde{x}_e} \mathbf{t}_e(\tilde{x}_e). \tag{5.14}$$

This sensitivity implies that adding conductive material to the design by increasing the element density will decrease the compliance and therefore improve heat conduction through the structure. This is why an upper limit on volume must be prescribed, and this constraint will remain active throughout the optimization process. As with the previous problem formulations,

the chain rule is used to convert the above derivative with respect to physical element density to a derivative with respect to the element design variable x_e.

5.2 Heat conduction test case

This section explores a classical heat conduction problem studied by numerous authors including Dede (2009), Chen et al. (2010), and Bendsøe & Sigmund (2003) . The problem involves determining the optimal material distribution of a 3D structure consisting of a highly conductive material and an insulator, such that heat conduction is maximized. The design domain undergoes internal heat generation, with a heat sink at the base of the domain, adiabatic boundaries, and a constraint on the maximum allowable volume of the conductive material. A schematic of the problem setup is depicted in Figure 5.2.

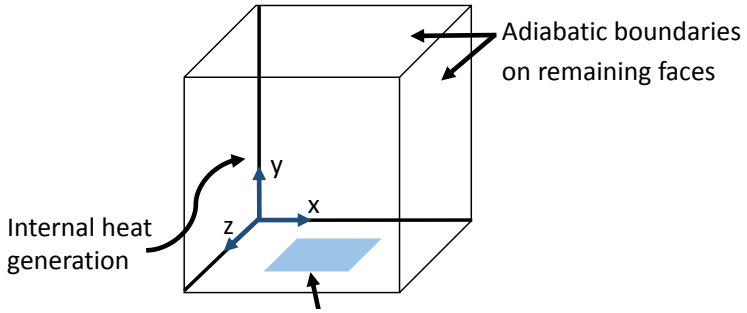

Figure 5.2: Boundary conditions for the heat conduction test case.

Results obtained by both Dede (2009) and Chen et al. (2010) are shown in Figure 5.3. The optimal topology exhibits a 'branched' structure which fans out towards the boundaries of the domain so that heat is drawn from the domain down to the heat sink.

5.2.1 Implementation

This 3D heat conduction test case is implemented in our topology optimization code using design options and parameter values that would best replicate the problem setup used by previous authors. A cubic design domain with side lengths of 0.2 m is discretized into 50 x 50 x 50 cubic elements. We only analyze one quarter of the domain due to the double symmetry of the structure. The desired volume fraction is set to $V_f = 0.30$, and an initial homogeneous distribution of material is prescribed where the element density is set to the given volume fraction. Internal heat generation is applied to all nodes throughout the domain, using an

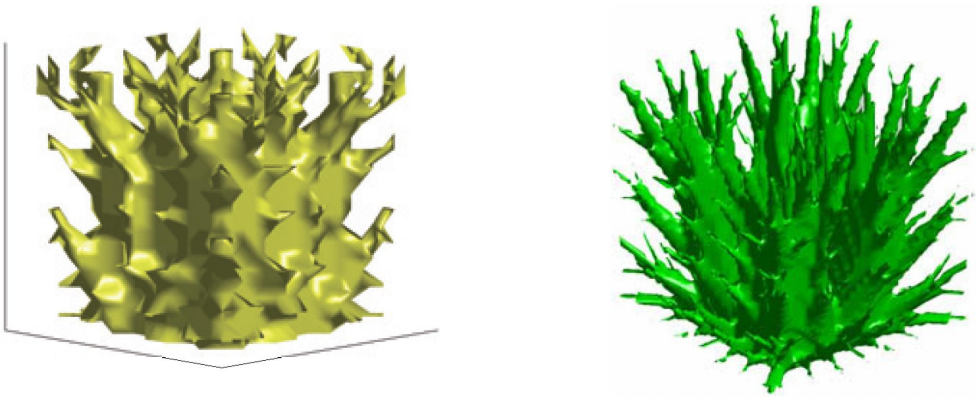

(a) (b)

Figure 5.3: Optimal structure obtained by (a) Dede (2009), and (b) Chen et al. (2010). Reprinted from Chen et al. (2010), Copyright (2010), with permission from Elsevier.

element thermal load vector of $\mathbf{f}_s^e = 0.01^*[1,1,1,1,1,1,1,1]^T$ W. There is a heat sink in a rectangular patch on the bottom face of the domain where the temperature is set to $T = 0°C$. For this problem we consider two materials, both of which exhibit isotropic thermal conductivity. The highly conductive material has a thermal conductivity of $k = 1$ $Wm^{-1\circ}C^{-1}$, while the less conductive material has a thermal conductivity of $k = 0.001$ $Wm^{-1\circ}C^{-1}$. A SIMP interpolation scheme is used in conjunction with a continuation scheme. The maximum penalty factor is set to $p = 3$. The algorithm uses a density filter with a filter radius of r = 0.01 m or 2.5 element lengths. The MMA is the chosen optimizer for this problem, because the loading is design independent and therefore the sensitivity is unconditionally negative. The GCMMA method will yield virtually identical results for this particular application, albeit with a greater computational time.

5.2.2 Results

Figure 5.4 shows the optimized structure obtained using our topology optimization code. It appears that these results are in good agreement with those presented in Figure 5.3. Iteration history of both the thermal compliance and volume fraction are shown in Figure 5.5. The compliance converges by approximately 50 iterations while the upper volume fraction limit of $vf = 0.30$ is attained. Possible reasons for slight discrepancies between the three optimized structures include use of different material properties values, thermal load, filter, filter radius,

plotting threshold, continuation scheme, solver, and optimization algorithm.

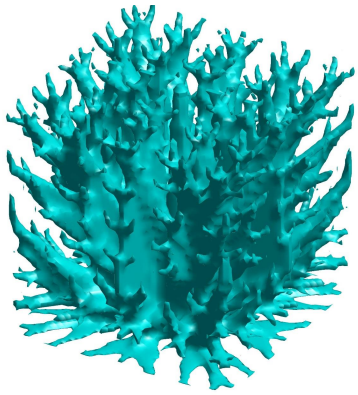

Figure 5.4: Optimal structure obtained using our topology optimization code.

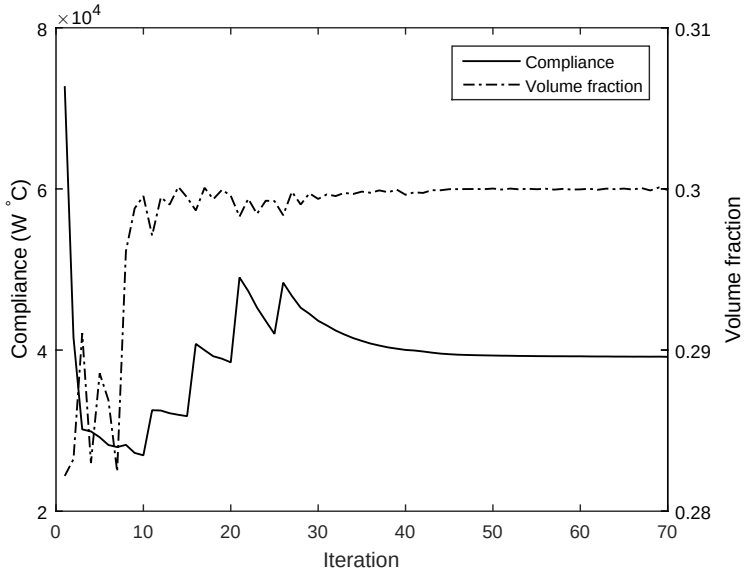

Figure 5.5: Plot showing thermal compliance and volume fraction vs iterations.

5.3 Topology optimization of the anode structure

Let us modify the heat conduction problem formulation for the objective of finding the material distribution in a silicon anode structure that maximizes electrical conduction during cycling, and therefore generates optimal charge transport pathways through the anode. As previously stated, the strong form may be expressed using Equation 5.3 and appropriate variable substi-

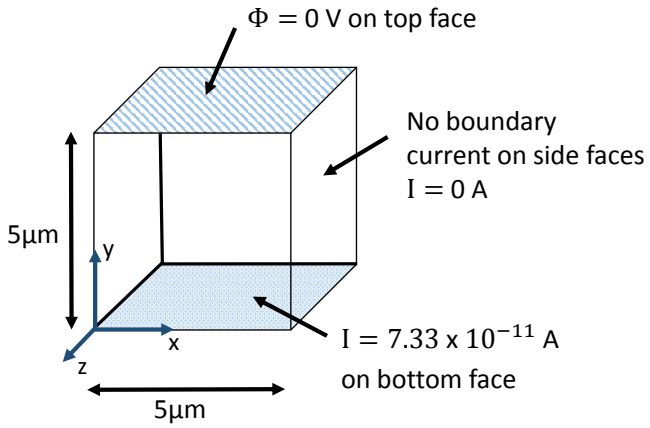

Figure 5.6: Schematic of boundary conditions applied to the periodic base cell.

tutions given in Table 5.1. As such, the governing Poisson's equation for electric conduction is given by

$$\nabla^T (\mathbf{D} \nabla \Phi) + S = 0, \tag{5.15}$$

where $\mathbf{D}$ is the electrical conductivity tensor, typically assigned the variable $\boldsymbol{\sigma}$ but in this case we wish to avoid any confusion with stress. Φ is the voltage and S is a current source.

5.3.1 Loading and boundary conditions

We study a 5 μm x 5 μm x 5 μm cubic base cell which is periodic in the x-z plane and discretized into finite elements, depicted in Figures 4.6a and 5.6. We model an anode undergoing galvanostatic charging, where the current remains at a constant value. This is implemented as a prescribed voltage of $\Phi = 0.0$ V on the top surface of the domain, and a current into the electrode from the bottom surface of the domain. We consider a maximum battery capacity of 4200 mAh/g, and a charging or C rate of $C/5$, which indicates that for the given current it will take 5 hours to fully lithiate or delithiate under ideal conditions (Quiroga-González et al., 2013). Assuming 30% of the domain is occupied by active silicon material with a density of 2328 kg m^{-3}, we obtain a current of 7.33 x 10^{-11} A. For this problem we assume no internal current source, and no flux on the remaining boundary faces. The discrete problem formulation

is given by

$$\begin{aligned} \min_{x}: \quad & c(\tilde{\mathbf{x}}) = \mathbf{\Phi}(\tilde{\mathbf{x}})^T \mathbf{K}(\tilde{\mathbf{x}})\mathbf{\Phi}(\tilde{\mathbf{x}}) \\ \text{subject to}: \quad & \mathbf{K}(\tilde{\mathbf{x}})\mathbf{\Phi}(\tilde{\mathbf{x}}) = \mathbf{F}, \\ & \frac{V(\tilde{\mathbf{x}})}{V_0} \leq V_f^{max}, \\ & \mathbf{0} \leq \mathbf{x} \leq \mathbf{1}, \end{aligned} \tag{5.16}$$

where $c(\tilde{\mathbf{x}})$ may be considered as the electrical compliance, $\mathbf{\Phi}(\tilde{\mathbf{x}})$ is the global voltage vector, $\mathbf{K}(\tilde{\mathbf{x}})$ is the global electrical conductance matrix, and $\mathbf{F}$ is the design independent global electrical load vector, which has non-zero terms due to the boundary current.

5.3.2 Problem parameters

As in Chapter 4.4, we consider two material phases: the anode and the electrolyte. The silicon anode is a semiconductor and is assigned an isotropic conductivity of $d_{anode} = 0.067$ Sm^{-1} (Ryu et al., 2004). The electrolyte is an electrical insulator, and is prescribed a very small conductivity to avoid singularities, $d_{electrolyte} = 1$ x 10^{-5} Sm^{-1}. Unless otherwise stated, the required volume fraction is $V_f = 0.3$ and is set to be the upper bound on anode material volume. The initial element density is set to $V_f = 0.25$, or 0.05 below the material limit. The SIMP interpolation is used for the electrical conductivity $d(\tilde{x}_e)$ with a maximum penalty value of $p = 3$. To prevent numerical difficulties such as mesh dependence, and to impose a minimum length scale, density filtering is employed with a filter radius of r $= 2\mu$m. We utilize the MMA method to determine the updated densities on each iteration.

5.3.3 Results

Figure 5.7 depicts the optimized anode structure using the above material parameters. In order to maximize electrical conduction, it appears that the structure must have direct electronic pathways through the thickness of the electrode. These structures show some resemblance to the silicon nanowires discussed in Section 1.3.5.

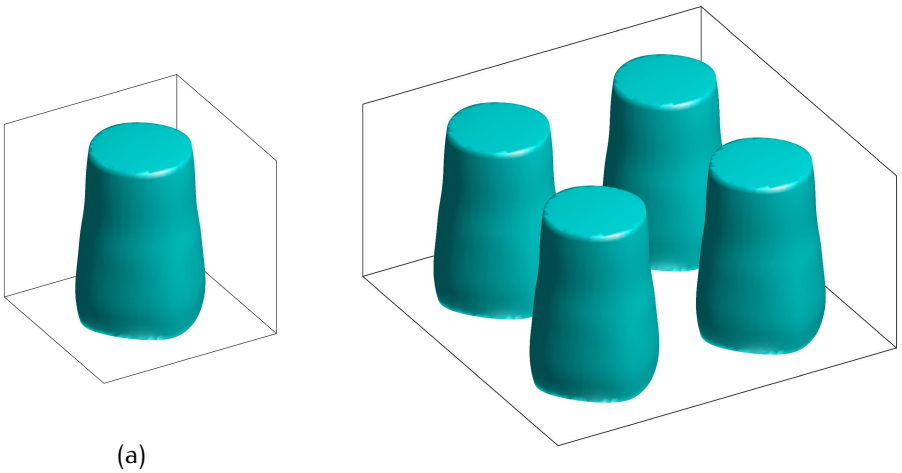

(a)

(b)

Figure 5.7: Anode structure optimized for maximum electrical conduction with a volume fraction of $V_f = 0.3$: (a) 1 base cell, (b) 2 x 2 base cells.

The iteration history for electrical compliance and volume fraction are shown in Figure 5.8. The compliance converges to an optimum value of 3.9318 x 10^{-7} A-V by 160 iterations. The volume fraction attains the upper bound of 30% material for the conductive silicon phase.

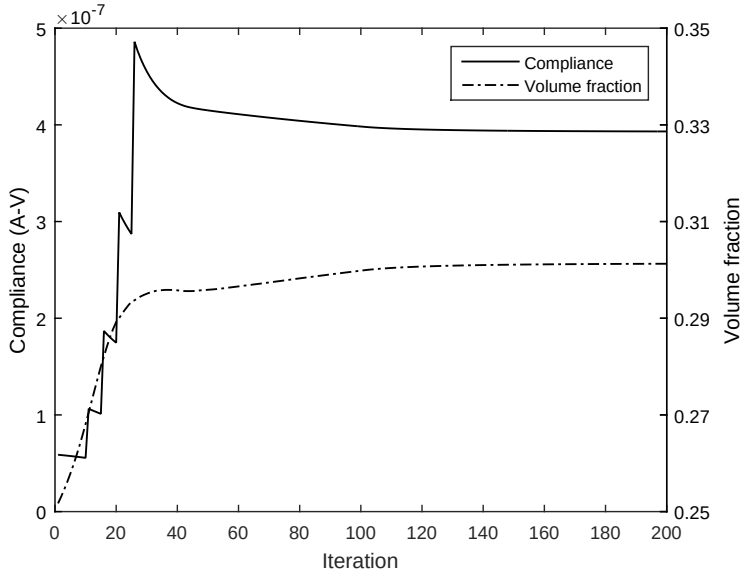

Figure 5.8: Electrical compliance and volume fraction as a function of iterations.

Figure 5.9 depicts the optimal structures for various numbers of elements. The design is consistent for the different discretizations, confirming mesh independence.

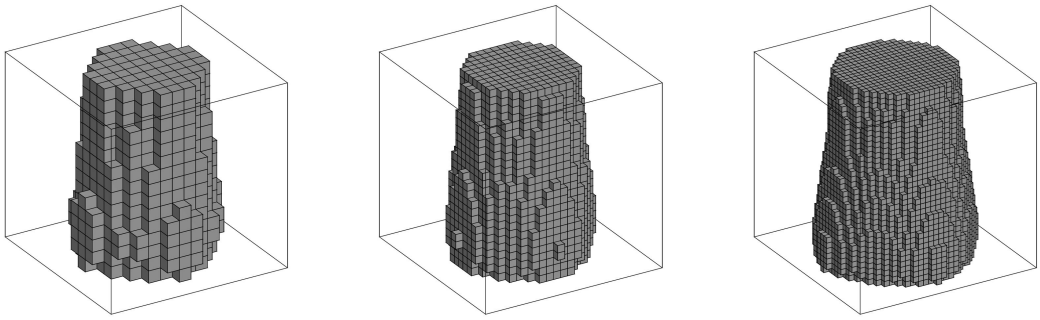

(a) 15 x 15 x 15 elements (b) 25 x 25 x 25 elements (c) 35 x 35 x 35 elements

Figure 5.9: Optimized structure for varying numbers of elements.

As with the minimum compliance objective, a selection of volume fractions were tested to determine how changing the limit on the allowable material influenced the final design. Figure 5.10 shows that increasing the volume fraction results in a larger radius of the cylindrical structure. For larger volume fractions the structure becomes increasingly tapered, allowing more current to be transported through the silicon structure from the base of the cell. Figure 5.11 depicts the electrical compliance vs volume fraction. For this problem the electrical compliance decreases with increasing volume fraction. Therefore, a structure with a greater material volume will be a better conductor of electricity.

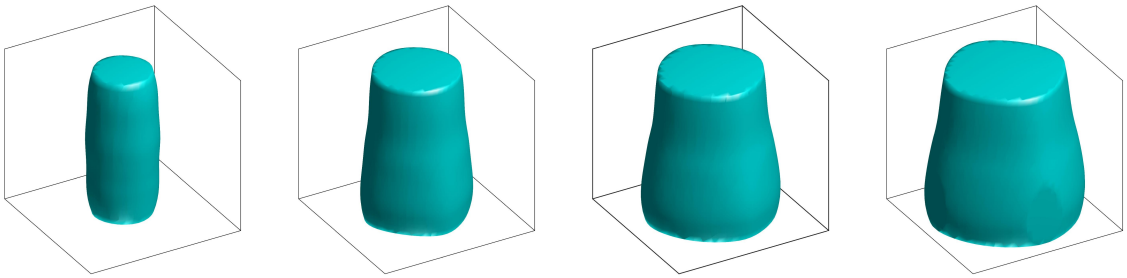

(a) $V_f = 0.15$ (b) $V_f = 0.30$ (c) $V_f = 0.45$ (d) $V_f = 0.60$

Figure 5.10: Optimized base cell structures for varying volume fractions.

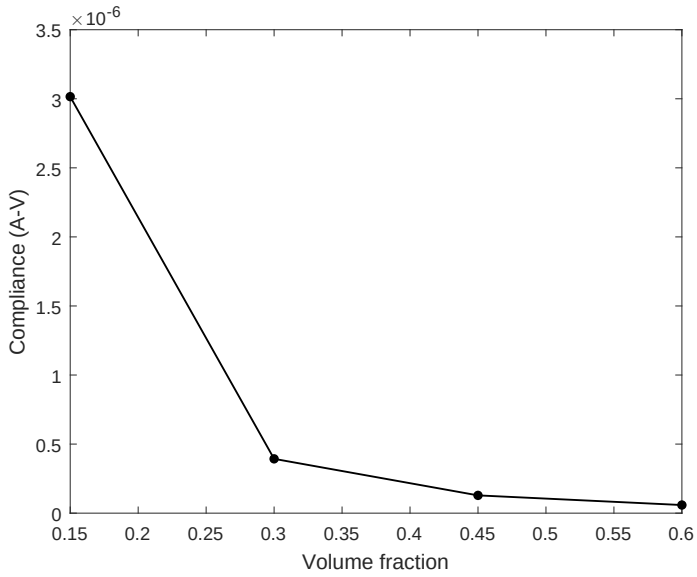

Figure 5.11: Compliance as a function of prescribed volume fraction.

5.3.3.1 Influence of minimum length scale and aspect ratio

The length scale associated with the solution of this optimization problem is dependent on the comparative values of the filter radius, domain size, and the number of elements. The remainder of this chapter explores the effect of changing these values on the topology of the structure.

The filtering radius directly impacts the minimum length scale of the solution, as an element's density is taken to be a weighted average of the neighbouring elements within this radius. This conduction problem was originally run with a filter radius of r = 2 μm, the same size used to obtain the optimal anode structures presented in Chapter 4. For this design the material is lumped together in a single cylindrical structure, as shown in Figure 5.7. The simulation was subsequently run with various filter radii to determine whether this length scale will have an impact on the topolgogy of the optimized structure. The following radii were tested: r = 1 μm, r = 0.5 μm, r = 0.25 μm, and r = 0.17 μm. The optimized structures are shown in Figure 5.12. The top depicts the base cell produced as output from the analysis, while an offset base cell is depicted in the bottom row for additional clarity.

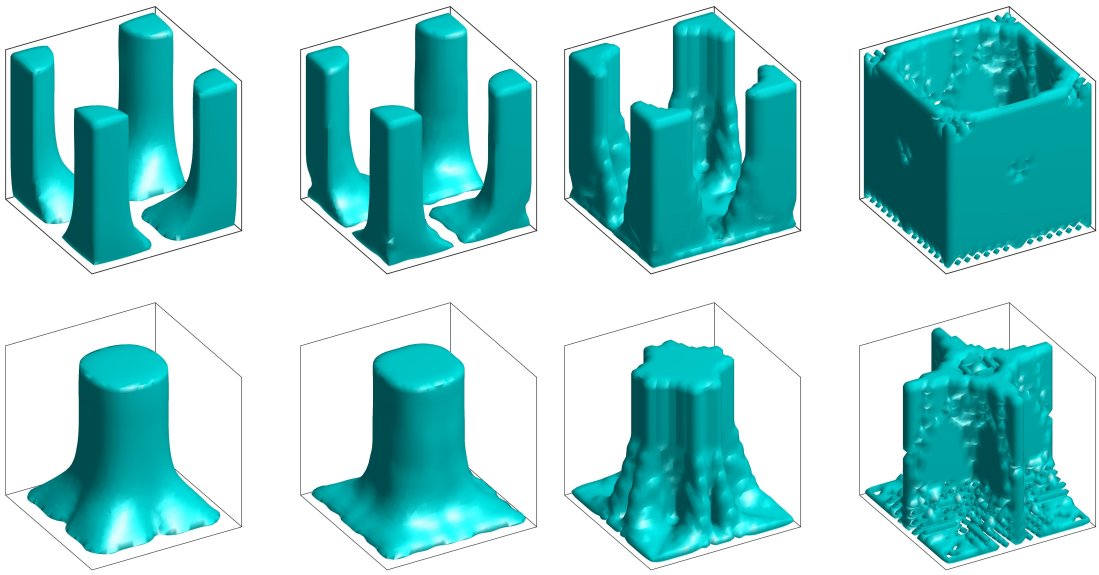

(a) r = 1 μm (b) r = 0.5 μm (c) r = 0.25 μm (d) r = 0.17 μm

Figure 5.12: Optimized base cell for various filter radii, a 5 μm x 5 μm x 5 μm domain and a volume fraction of $V_f = 0.3$. The top row depicts the base cell designs directly from the simulation, while the bottom row shows the designs shifted by half a base cell in the x and z-directions.

The most noticeable change between the r = 2 μm design and the structures shown in Figure 5.12 is that the material has accumulated in the corners rather than the center of the base cell. However, plotting the shifted base cell shows that we still obtain similar cylindrical structures to the r = 2 μm design. This change in material location is related to the magnitude of the filter radius. For this problem formulation, the filter radius will cause material to progressively accumulate together throughout the iterations, where the degree of accumulation is dependent on the size of the filter radius. A larger filter radius means a greater number of neighboring elements' densities are used to determine the weighted average density of each element. If the filter radius is large enough, such as r = 2 μm, the material will typically accumulate in the center of the cell, while smaller radii allow the material to accumulate in the four corners. This is because the influence of the small radii does not exceed the width of the void area between the quarter cylinders, and as such material is free to accumulate in the corners.

Another observation is that a larger filter radius will typically produce structures with greater surface curvature and therefore lower silicon/electrolyte interface area. Furthermore, decreasing the filter radius results in a more tapered base of the cylindrical structure, where

the current enters the domain from the current collector. This change in base shape increases the amount of current flowing through the structure. This is because a set value of current is prescribed at each node on the bottom face of the domain. As such, the greater the bottom face area covered by the silicon, the greater the current flowing through the anode structure. The structure for r = 0.25 μm resembles the base of a tree trunk, where the 'roots' fan out to draw in the current from the base of the cell. When the filter radius is reduced even further to r = 0.17 μm, which is equivalent to one element length, non-physical checkerboarding behaviour can be observed.

A plot of electrical compliance vs filter radius presented in Figure 5.13 shows that the compliance decreases with decreasing filter radius. As might be expected, the smallest filter radius of r = 0.17 μm shows an artificially low electrical compliance value due to the checkerboarding behaviour. Further details on this matter may be found in Chapter 3.7. Therefore, a trade-off exists between obtaining the optimum structure and a structure that is non-physical. As such, caution must be exercised when choosing an appropriate length scale to ensure the design is well-posed and manufacturable.

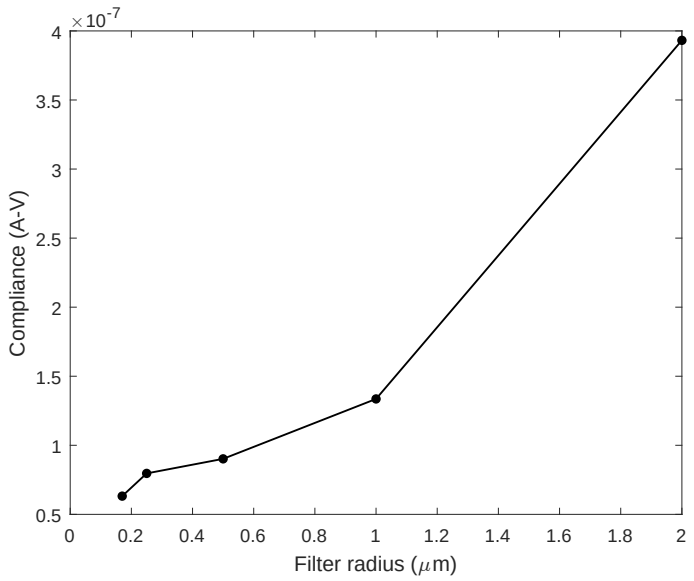

Figure 5.13: Electrical compliance as a function of prescribed volume fraction.

We now investigate the effect of changing the base cell aspect ratio. Until this point, we have considered a base cell with equal side lengths of 5 μm. A modified base cell with the same footprint area as the original base cell but a height three times greater is analysed. The

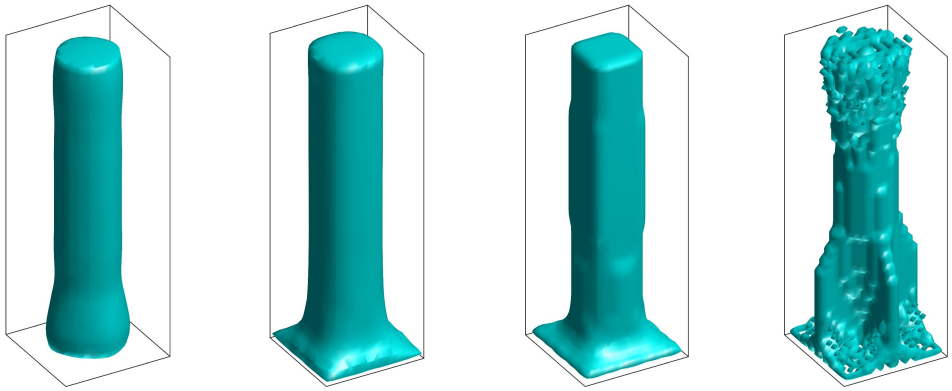

(a) r = 2 μm (b) r = 1 μm (c) r = 0.5 μm (d) r = 0.25 μm

Figure 5.14: Optimized base cell for various filter radii, 5 μm x 5 μm x 15 μm domain and a volume fraction of $V_f = 0.3$

overall dimensions are 5 μm x 5 μm x 15 μm with an element discretization of 20 x 20 x 60 elements. A volume fraction of 0.3 is prescribed, and filter radii of r = 2 μm, r = 1 μm, r = 0.5 μm, r = 0.25 μm, and r = 0.17 μm are considered. Figure 5.14 depicts the optimal structures. When a filter radius of 2 μm is used, we obtain a structure very similar to that presented in Figure 5.14a, only elongated in the vertical direction. Decreasing the filter radius has a very similar effect to the results shown above, where the base of the cylinder becomes increasingly tapered and a reduction in the value of compliance is observed. Furthermore, the cross-section appears to transition from a circular shape to a square. For this aspect ratio, we observe checkerboarding starting at a larger radius of r = 0.25 μm. The results for r = 0.17 μm appear almost identical to Figure 5.14d and are therefore not shown. These results further illustrate the importance of using regularization methods to ensure well-posed solutions.

5.4 Summary

This chapter aimed to determine silicon anode designs that maximized the electrical conduction through the structure. Due to the analogous nature of heat and electric conduction, the problem formulation for heat conduction and a benchmark heat conduction problem involving a heat sink and internal heat generation were first presented. The anode structure was subsequently optimized for maximum electrical conduction, producing rod-like designs that provided an efficient conduction pathway through the thickness of the anode structure. The iteration history, mesh independence, and influence of volume fraction were studied, and subsequently

a parameter investigation involving the minimum length scale and base cell aspect ratio was conducted. It was found that a reduction in length scale progressively decreased the value of electrical compliance; however, checkerboarding behaviour was observed once the length scale became very small. Increasing the base cell aspect ratio resulted in elongated silicon structures, with similar observed trends as the original aspect ratio for a reduction in length scale.

Chapter 6

Combining Objectives

In this chapter we perform multi-objective topology optimization to produce anode structures that simultaneously address the structural and conduction design requirements. First, the concepts of Pareto optimal solutions and the weighted sum method are presented. A verification problem originally analysed by Chen et al. (2010) is subsequently explored. Multi-objective topology optimization is then applied to the silicon anode problem, and a parameter study is conducted to determine the influence of the minimum length scale and prescribed volume fraction on the optimal solutions.

6.1 Problem formulation

Multi-objective optimization methods aim to determine a solution that best satisfies a number of objectives which are typically conflicting and non-commensurable. Following the convention of Koski & Silvennoinen (1987), the multi-objective optimization problem may be defined as

$$\begin{aligned} \min_{x\in\Omega} : \quad & [f_1(\mathbf{x}), f_2(\mathbf{x}), \ldots, f_i(\mathbf{x}), \ldots, f_m(\mathbf{x})]^T \\ \text{subject to} : \quad & g(\mathbf{x}) \leq 0, \\ & h(\mathbf{x}) = 0, \end{aligned} \tag{6.1}$$

where f_i are the different objective functions for $i = 1, 2, \ldots, m$, to be minimized simultaneously subject to inequality and equality constraints. The vector of design variables is given by $\mathbf{x} = [x_1, x_2, \ldots, x_n]^T$, and Ω is the feasible set in the design space R^n. Due to the competing nature of the objective functions, there usually exists no single global solution that would

simultaneously give an optimum for all m objectives. As such a trade-off is required, and the concept of Pareto optimality (Pareto, 1906) is used to determine the series of solutions that make up the optimum. The Pareto optimum is defined by Koski & Silvennoinen (1987) as follows:

Definition: A vector $\mathbf{x}^* \in \Omega$ is Pareto optimal for the optimization problem given by Equation 6.1 if and only if there exists no $\mathbf{x} \in \Omega$ such that $f_i(\mathbf{x}) \leq f_i(\mathbf{x}^*)$ for $i = 1, 2, \ldots, m$ with $f_j(\mathbf{x}) < f_j(\mathbf{x}^*)$ for at least one j.

In other words, $\mathbf{x}^*$ is Pareto-optimal if there exists no feasible solution $\mathbf{x}$ that would decrease at least one objective function without causing a simultaneous increase in at least one other objective The set of Pareto-optimal points forms a Pareto front, also called a Pareto curve for a two-objective problem. A schematic of a Pareto curve and Pareto-optimal points is depicted in Figure 6.1.

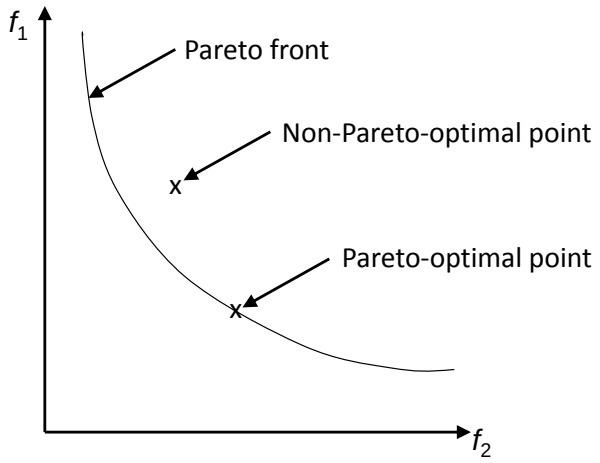

Figure 6.1: Pareto front for two objective functions, f_1 and f_2.

One method to obtain Pareto optimal solutions is the weighted sum, or weighting method (Zadeh, 1963). The multi-objective problem is reformulated as a single objective problem using weight factors, where the summation of the weights is unity, and the objectives are normalized. Using the weighting method, the following problem is solved:

$$\begin{aligned} \min_{x \in \Omega} : \quad F &= \sum_{i=1}^{m} w_i \frac{f_i}{f_i^*} \\ &= w_1 \frac{f_1}{f_1^*} + w_2 \frac{f_2}{f_2^*} + \ldots + w_m \frac{f_m}{f_m^*}, \end{aligned} \tag{6.2}$$

where F is the multi-objective function, and w_i is the ith objective weighting function with the requirements of $0 \leq w_i \leq 1$ and $\sum_{i=1}^{m} w_i = 1$. The ith objective function is given by f_i while f_i^* is the maximum objective function value, which is used for normalization. This method involves a priori articulation of preferences, where the user indicates the relative importance of the objective functions by assigning values to the weights before running the optimization algorithm (Marler & Arora, 2004). Equation 6.2 determines one particular optimal solution on the Pareto front. The weights may be continuously altered to form the complete set of Pareto-optimal designs.

6.2 Multi-objective topology optimization test case

A validation step was first undertaken by reproducing the results presented by Chen et al. (2010). Chen et al. (2010) developed a topology optimization algorithm for multifunctional 3D finite periodic structures, simultaneously addressing the maximum stiffness and maximum heat conductivity criteria using a weighted average method. This test case was used to verify that our underlying computational methodology and implementation of the multiple objective topology optimization problem formulation was correct.

6.2.1 Problem formulation and implementation

The problem formulation presented by Chen et al. (2010) may be written as:

$$\min_{x} : \quad c(\tilde{\mathbf{x}}) = w_s C_s(\tilde{\mathbf{x}}) + w_c C_c(\tilde{\mathbf{x}}) \tag{6.3}$$

$$= w_s \frac{\mathbf{U}(\tilde{\mathbf{x}})^{\mathsf{T}} \mathbf{K_s}(\tilde{\mathbf{x}}) \mathbf{U}(\tilde{\mathbf{x}})}{C_s^*} + w_c \frac{\mathbf{T}(\tilde{\mathbf{x}})^{T} \mathbf{K}_c(\tilde{\mathbf{x}}) \mathbf{T}(\tilde{\mathbf{x}})}{C_c^*} \tag{6.4}$$

$$\text{subject to :} \quad \frac{V(\tilde{\mathbf{x}})}{V_0} = V_f^{max},$$

$$\mathbf{0} \leq \mathbf{x} \leq \mathbf{1},$$

where $C_s(\tilde{\mathbf{x}})$ and $C_c(\tilde{\mathbf{x}})$ are the stiffness and conduction objective functions, respectively. The weighting factors for the mechanical and thermal compliance objectives are w_s and w_c, respectively. $\mathbf{U}(\tilde{\mathbf{x}})$ is the displacement field due to both the mechanical and thermal loadings, $\mathbf{K_s}(\tilde{\mathbf{x}})$ is the global stiffness matrix, $\mathbf{T}(\tilde{\mathbf{x}})$ is the temperature field, and $\mathbf{K_c}(\tilde{\mathbf{x}})$ is the global conductivity matrix. The individual objectives are normalized by their maximum values, C_s^* and C_c^*.

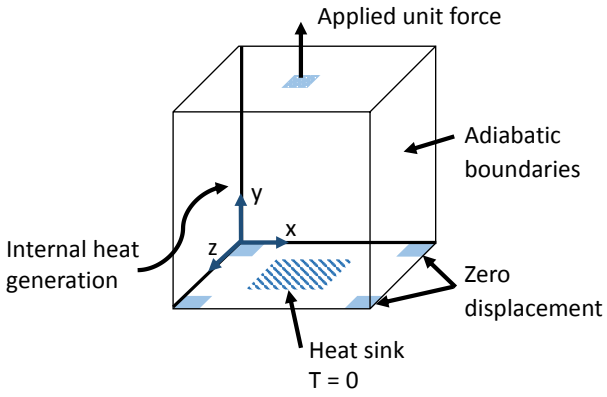

Figure 6.2: Loading and boundary conditions for the multi-objective test case.

Figure 6.2 depicts the loading and boundary conditions for the problem. Vertical displacement is restrained at the bottom four corners of the domain, while a unit force is applied in an upwards direction on the center of the top surface. This design problem is commonly referred to as the 'stool' problem, and has been explored by other authors such as Borrvall & Petersson (2001) and Suresh (2013). The heat conduction problem is the same as presented in Chapter 5.2. The design domain is heated evenly at all nodes and a heat sink is located in a square section at the center of the bottom surface, where the temperature is kept to be zero degrees.

Like Chapter 5.2, a cubic design domain with side lengths of 0.2 m is discretized into 50 x 50 x 50 cubic elements. The desired volume fraction is set to $V_f = 0.25 - 0.30$, and an initial homogeneous distribution of material is prescribed where the element density is set to the lower bound on volume fraction. We consider two materials, a solid and void. The solid phase is stiff and conductive with a Young's modulus of $E = 1$ GPa, a Poisson's ratio of $\nu = 0.3$, and an isotropic thermal conductivity of $d = 1$ $\mathrm{Wm}^{-1\circ}\mathrm{C}^{-1}$. The void phase is assigned very small material parameter values to prevent singular behaviour. We consider a SIMP interpolation scheme for the Young's modulus and thermal conductivity with a maximum penalty parameter of $p = 3$, while a RAMP interpolation scheme is used for the thermal load, with a maximum value of $p = 8$. A density filter is implemented with a filter radius of r = 0.01 m or 2.5 element lengths.

6.2.2 Results

The results of Chen et al. (2010) are provided in Figure 6.3, while the structural topologies obtained using our code are shown in Figure 6.4. The Pareto front shows how the competing design objectives influence the resulting topologies as the weights are varied from the full stiffness design, $w_s = 1$, to the full conduction design, $w_s = 0$. When the stiffness objective dominates we obtain a structure with struts, or legs of the stool, connecting the corners to the location of applied loading. The four legs of the stool are connected by thin bars at the base of domain. When the conduction objective dominates, the optimal design is a doubly-symmetric tree-like configuration with numerous fine twigs to draw heat from the domain down to the heat sink. Intermediate weights show a progression of structures that have both strut and twig-like features. The Pareto front clearly illustrates the design trade-off, where a reduction in the value of one objective will be accompanied by an increase in the value of the competing objective.

It is clear that the two sets of results depict a similar progression of structures. Slight discrepancies may be attributed to the use of a different filter, filter radius, plotting threshold, continuation scheme, and solver, none of which were specified in the paper. Overall, our results appear in agreement with those presented in Chen et al. (2010), thereby verifying our computational methodology and implementation.

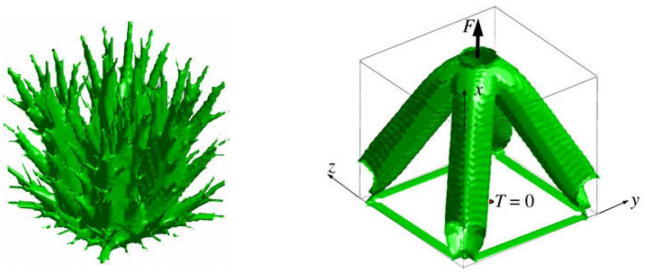

(a) $w_s = 0$ (b) $w_s = 1$

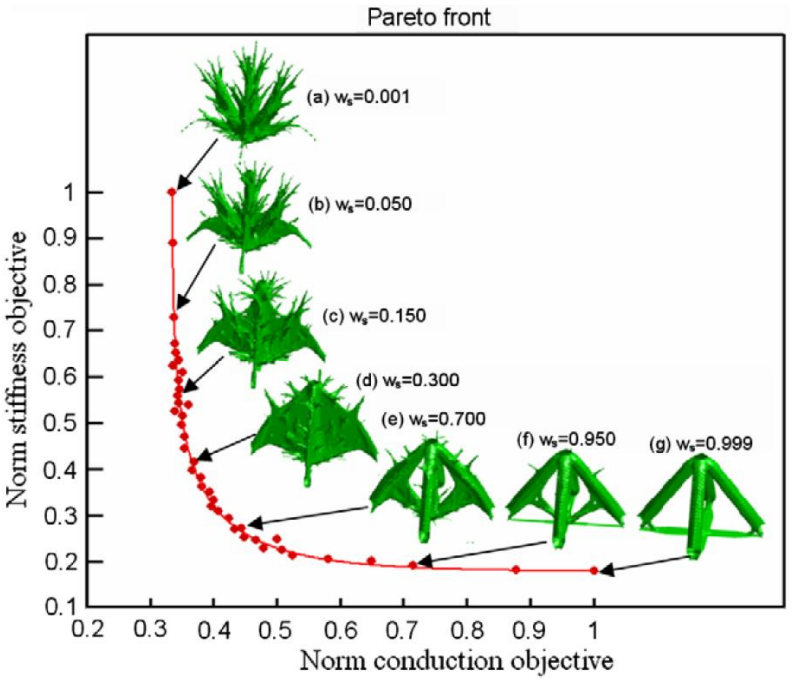

(c) Pareto front and corresponding structural topologies

Figure 6.3: Topology optimization results produced by Chen et al. (2010). Reprinted from Chen et al. (2010), Copyright (2010), with permission from Elsevier.

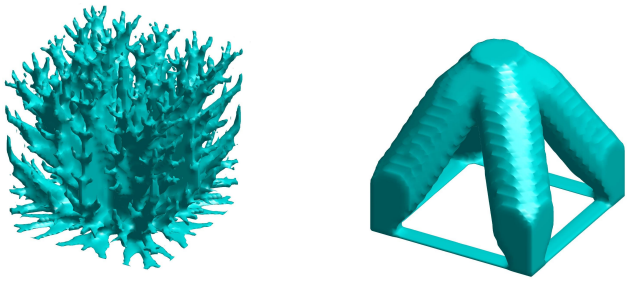

(a) $w_s = 0$ (b) $w_s = 1$

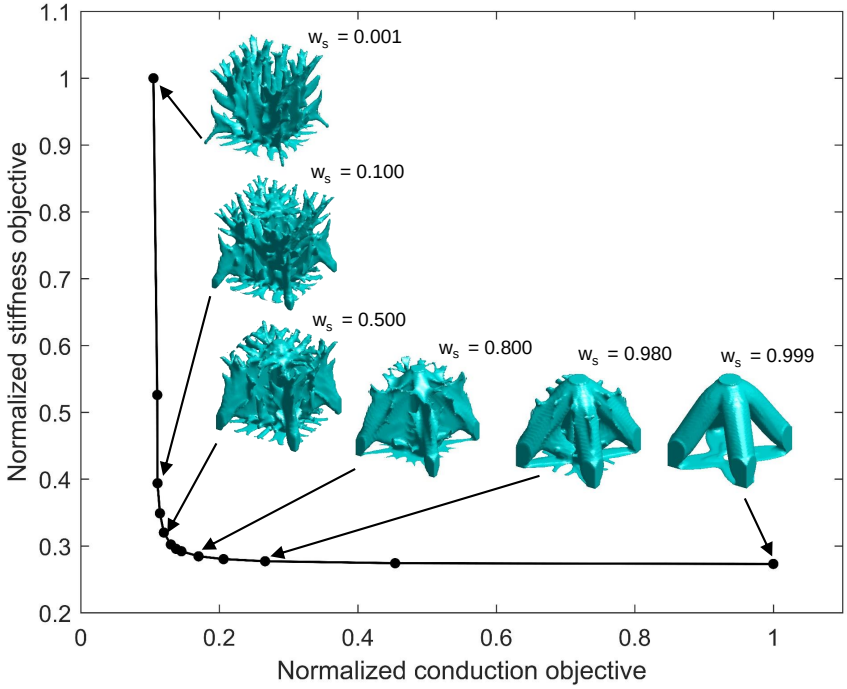

(c) Pareto front and corresponding structural topologies

Figure 6.4: Topology optimization results produced using our algorithm.

6.3 Multi-objective topology optimization of the anode structure

Multi-objective topology optimization is now applied to the silicon anode structure undergoing lithiation. The design objectives of minimum compliance for design-dependent volume expansion presented in Chapter 4, and maximum electrical conduction presented in Chapter 5, are combined into a single objective function using the weighted sum method. The Pareto curves and optimal designs for different combinations of filter radius and prescribed volume fraction are presented and discussed.

6.3.1 Problem formulation and implementation

The multi-objective problem formulation is the weighted sum of the individual minimum compliance and maximum conduction objectives.

$$
\begin{aligned}
\min_{x}: \quad & c(\tilde{\mathbf{x}}) = w_s \frac{\mathbf{U}(\tilde{\mathbf{x}})^{\mathsf{T}} \mathbf{K_s}(\tilde{\mathbf{x}}) \mathbf{U}(\tilde{\mathbf{x}})}{C_s^*} + w_c \frac{\mathbf{\Phi}(\tilde{\mathbf{x}})^{T} \mathbf{K}_c(\tilde{\mathbf{x}}) \mathbf{\Phi}(\tilde{\mathbf{x}})}{C_c^*} \\
\text{subject to}: \quad & V_f^{min} \leq \frac{V(\tilde{\mathbf{x}})}{V_0} \leq V_f^{max}, \\
& \mathbf{K_s}(\tilde{\mathbf{x}}) \mathbf{U}(\tilde{\mathbf{x}}) = \mathbf{F}_s(\tilde{\mathbf{x}}) = \mathbf{F}_s^m + \mathbf{F}_s^v(\tilde{\mathbf{x}}), \\
& \mathbf{K}_c(\tilde{\mathbf{x}}) \mathbf{\Phi}(\tilde{\mathbf{x}}) = \mathbf{F}_c, \\
& \mathbf{0} \leq \mathbf{x} \leq \mathbf{1}.
\end{aligned}
\tag{6.5}
$$

For clarity, the same subscripts of s and c from Equation 6.4 are used to represent the structural and conduction objectives, respectively. $\mathbf{U}(\tilde{\mathbf{x}})$ is the displacement field due to the design dependent thermoelastic loading, $\mathbf{K_s}(\tilde{\mathbf{x}})$ is the global stiffness matrix, $\mathbf{\Phi}(\tilde{\mathbf{x}})$ is the global voltage vector, and $\mathbf{K_c}(\tilde{\mathbf{x}})$ is the global electrical conductance matrix. The objectives are normalized by their maximum values C_s^* and C_c^*, which are calculated by running the algorithm for zero weights, i.e, $w_s = 0$ and $w_c = 0$, respectively. We prescribe both an upper and lower bound on the volume fraction. The structural objective will push the solution to the lower bound on volume fraction, while the conduction objective will push the solution towards the upper bound. As such, the design domain is initialized with densities equal to the median value between these two bounds. All other parameters remain the same as presented in Chapters 4 and 5.

6.3.2 Results

Figure 6.5 depicts the Pareto curve for a volume fraction $V_f = 0.30$ and a filter radius r = 2 μm. The Pareto weight of the structural objective is varied between $w_s = 0$ and $w_s = 1$. When the weight is $w_s = 1$, only the structural objective is considered and the resulting optimal structure is the same as that presented in Chapter 4.4.3. The value of the normalized structural objective is at a minimum, while the normalized conduction objective takes its maximum value of 1. As the Pareto weight decreases, the conduction objective begins to have an effect on the optimized structure. The circular hollows on the vertical faces become elliptical in shape, allowing for more material to be aligned in the direction of current flow. By $w_s = 0.68$ the

connection between the vertical struts at the top of the structure is severed. Repeating this periodic structure in the x-z plane results in columnar structures with square cross-sections. A further reduction in Pareto weight causes the structure to collapse down to half the base cell height, with material lining the vertical face and a cylindrical hollow in the center of the domain. The material then accumulates in the center of the domain before it finally stretches out to form the cylindrical structures for the full conduction objective at the Pareto weight of $w_s = 0$.

It is interesting to note that the optimized structures for $w_s = 0$ and $w_s = 0.68$ bear a close resemblance, only with differing cross-sections and tapering at the base of the structures. We would therefore expect both structures to have similar conduction objective values. The difference between these objective values may be attributed to the effect of the large filter radius of r = 2 μm and the influence of the conduction objective. As discussed in Section 5.3.3.1, when conduction dominates and the filter radius is set to r = 2 μm, material will accumulate in the center of the domain producing structures with a circular cross-section. However, when the structural objective dominates, material tends to accumulate near the edges of the domain. The circular cross-section structures of $w_s = 0$ will have a lower silicon/electrolyte interface area than the square cross-section structures of $w_s = 0.68$. This low interface area is implicitly favored for the conduction objective and therefore results in a lower conduction objective value. The transition structures between $w_s = 0.00 - 0.68$ may also be attributed to the conduction objective favoring low interface area structures.

Further evidence that conduction is the dominant objective for this range of Pareto weights is given in Figure 6.6, where the final volume fraction is plotted as a function of the Pareto weight. It is known that the conduction objective will drive the solution towards the upper volume fraction bound of $V_f = 0.30$, while the structural objective will drive the solution towards the lower volume fraction bound of $V_f = 0.25$. Therefore, this figure clearly shows which objective is dominant for each Pareto weight. There is a distinct transition from conduction to structural objective dominance just below $w_s = 0.7$, which corresponds well with the observation that the low interface area transitional structures are related to the influence of the conduction objective.

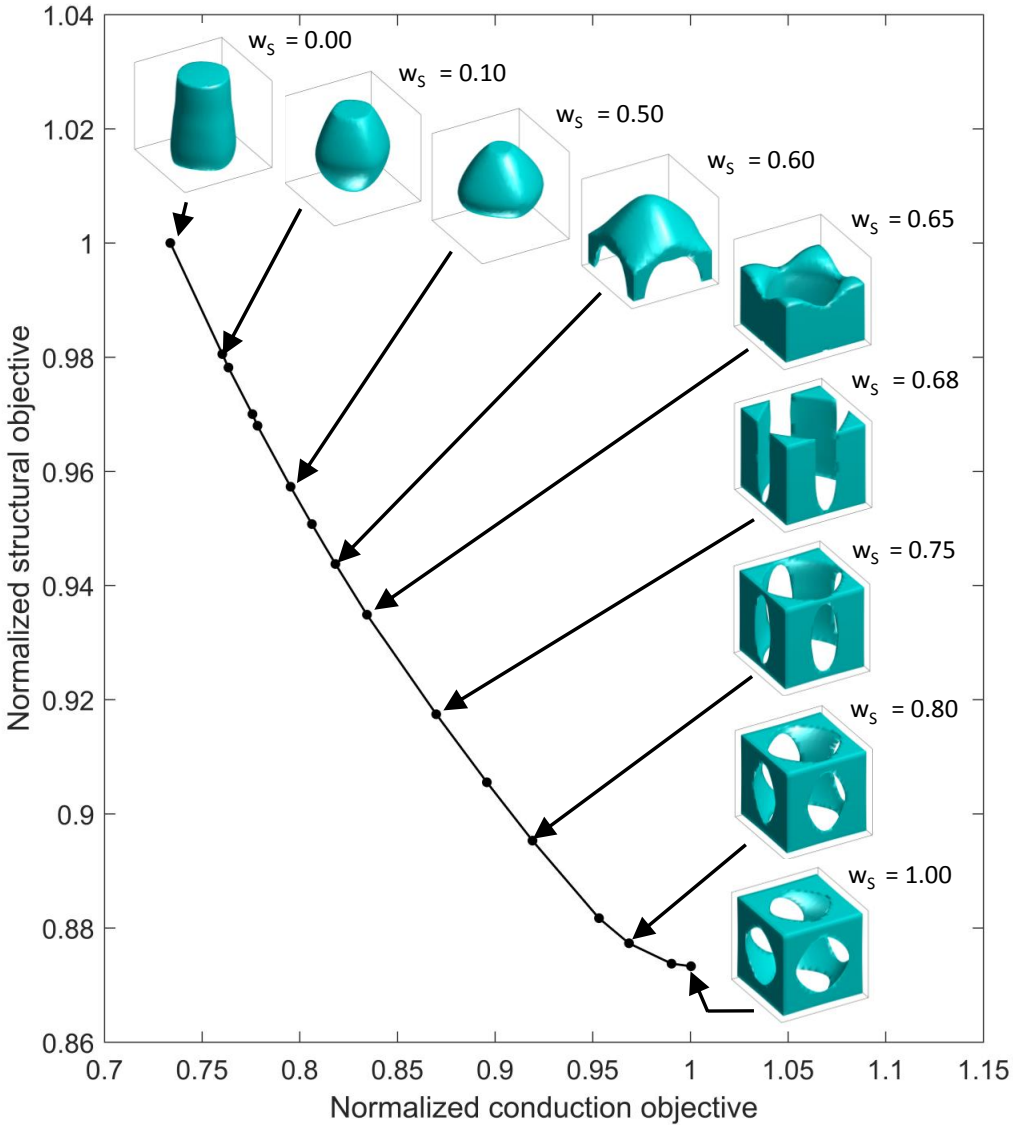

Figure 6.5: Pareto front and corresponding optimal topologies for $V_f = 0.30$ and a filter radius of r = 2 μm.

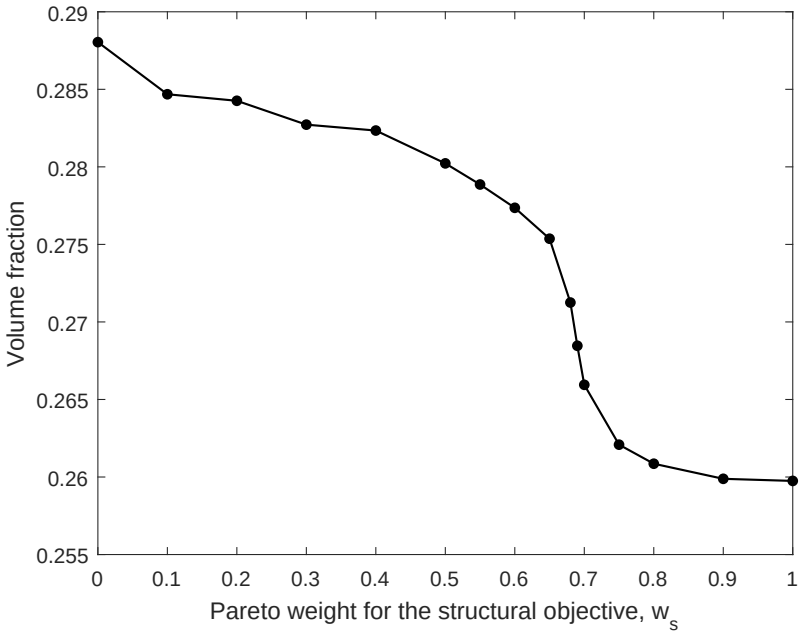

Figure 6.6: Volume fraction as a function of Pareto weight for $V_f = 0.30$ and a filter radius of r = 2 μm.

6.3.2.1 Influence of minimum length scale

For the previous Pareto curve shown in Figure 6.5, a large filter radius of r = 2 μm was chosen to ensure manufacturability of the full structural objective design. In this section, smaller filter radii of r = 1 μm and r = 0.5 μm are used to determine their influence on the multi-objective solutions. The same normalization values are used as for r = 2 μm so that the Pareto curves may be easily compared. It is expected that not all solutions are manufacturable, particularly when the structural objective dominates.

Figure 6.7 depicts the Pareto curve and associated optimal solutions for a volume fraction of $V_f = 0.30$ and a filter radius of r = 1 μm, and also the previous Pareto curve for r = 2 μm is shown in grey. Comparing these curves confirms some observations made in previous chapters. Firstly, for a full structural objective the value of the normalized structural compliance is slightly lower for the smaller filter radius (see Chapter 4.4.3.1). Similarly for the full conduction objective, the value of the normalized electrical compliance is significantly less for the r = 1 μm filter radius (see Chapter 5.3.3.1). Interestingly, the r = 1 μm curve almost overlaps with the majority of the r = 2 μm Pareto curve. This indicates that data points on these curves that

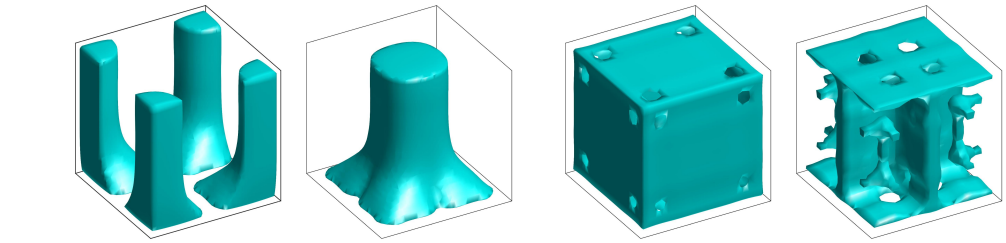

(a) $w_s = 0$ (b) $w_s = 1$

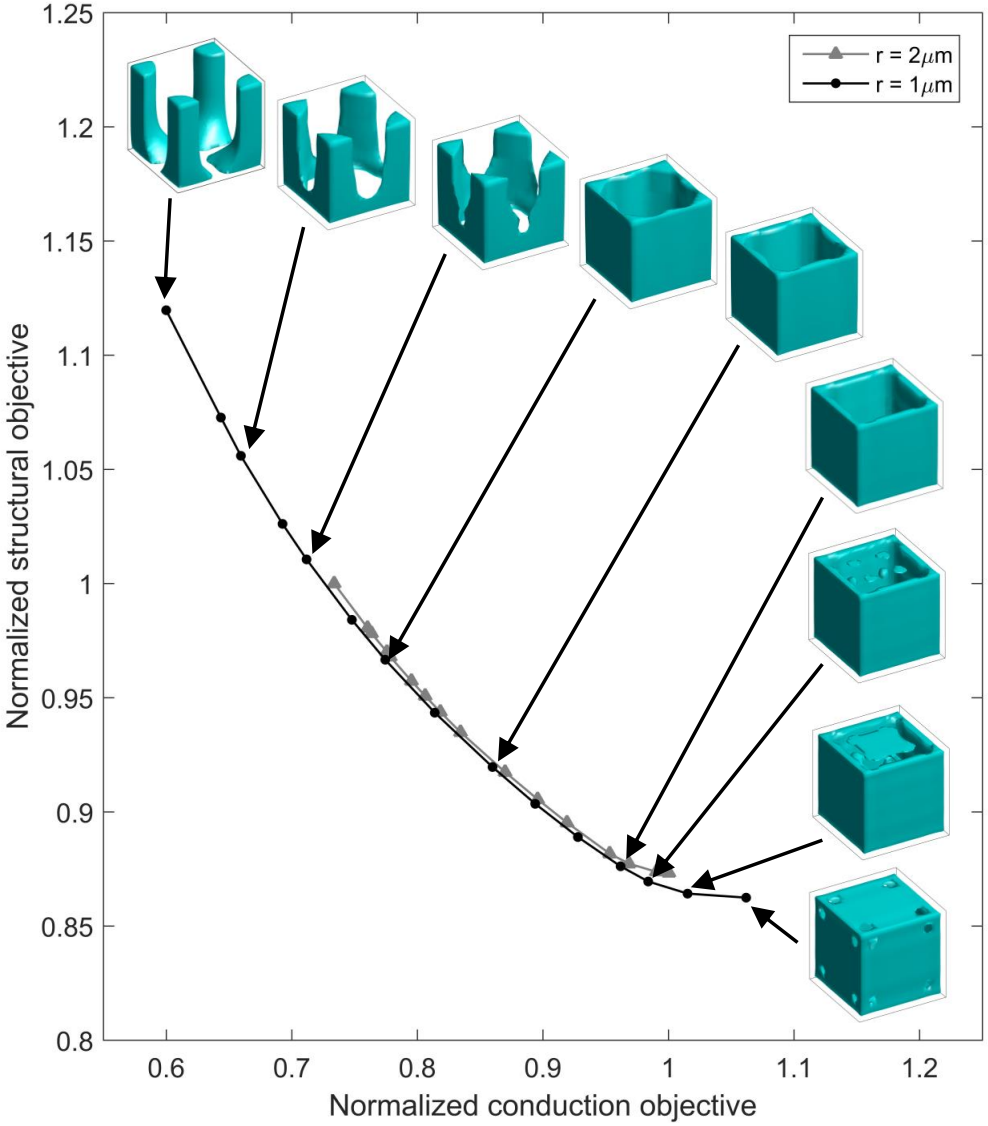

(c) Pareto front

Figure 6.7: Pareto front and optimal topologies for $V_f = 0.30$ and a filter radius of r = 1 μm: (a) base cell (*left*) and shifted base cell (*right*) for the full conduction objective, $w_s = 0$, (b) base cell (*left*) and shifted base cell (*right*) for the full structural objective, $w_s = 1$, (c) Pareto front for both r = 1 μm (*black*) and r = 2 μm (*grey*), and the corresponding optimal structures for r = 1 μm.

coincide with each other will have almost the same values and proportions of the objective functions, and therefore would be expected to exhibit similar performance.

The optimal structures show a clear progression from the full structural objective, $w_s = 1$, to the full conduction objective, $w_s = 0$. The full structural objective, depicted in Figure 6.7b, may be considered as a hollow cube with an internal floating structure and holes on the faces near the corners. As the structural Pareto weight decreases, the increasing influence of the conduction objective causes the top and bottom faces to loose material, the side faces to gain material, and the internal floating structure to disappear. This results in a intermediate rigid frame structure that exhibits direct conduction pathways. When conduction begins to dominate, material begins to accumulate at the corners of the structure, while the central sections of the side faces loose material until the full conduction structure is obtained (Figure 6.7a).

A further reduction in filter radius to r = 0.5 μm results in subtle changes, as shown in Figure 6.8. As in Chapter 4.4.3.1, for $w_s = 1$ a small increase in the value of the structural objective is observed relative to the value for r = 2 μm. For the full conduction objective, the value of the normalized electrical compliance is lower than the two larger filter radii, which is in agreement with the observations detailed in Chapter 5.3.3.1. The progression of optimal structures is very similar to that depicted in Figure 6.7. From the full stiffness solution shown in Figure 6.8b, the vertical sides gain material promoting conduction pathways while the top and bottom faces become open. The floating internal structures decrease in size as the Pareto weight decreases, until they disappear altogether. The intermediate frame structure is produced which is almost identical to the structure shown in Figure 6.7c, except with a smaller radius of curvature in the corners due to the smaller filter radius. As conduction prevails, the walls of the intermediate structure recede, while the corners gain material to become the cylindrical structures of the full conduction objection (Figure 6.8a).

The intermediate frame structure is the stable solution for the central section of both the r = 1 μm and r = 0.5 μm Pareto curves. This structure offers a clear compromise between the structural and conduction objectives. The base cell, shifted base cell, and 2 x 2 base cell representations of this frame structure are depicted in Figure 6.9. This design provides the structural rigidity required by the minimum structural compliance objective. Furthermore, by virtue of the volume fraction, there are distinct spaces for the anode structure to expand into during lithiation. The electrical conduction objective is achieved by using direct conduction pathways from the top to the bottom of the anode structure. For a volume fraction of $V_f = 0.30$,

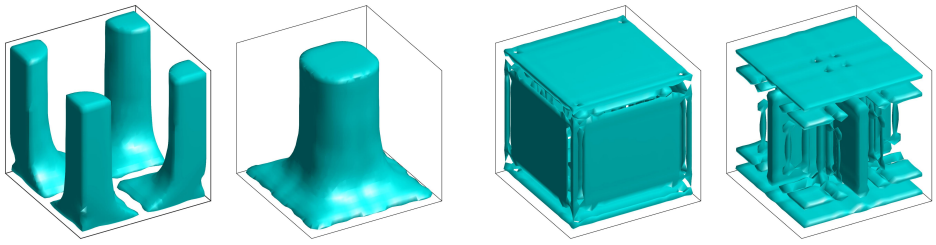

(a) $w_s = 0$ (b) $w_s = 1$

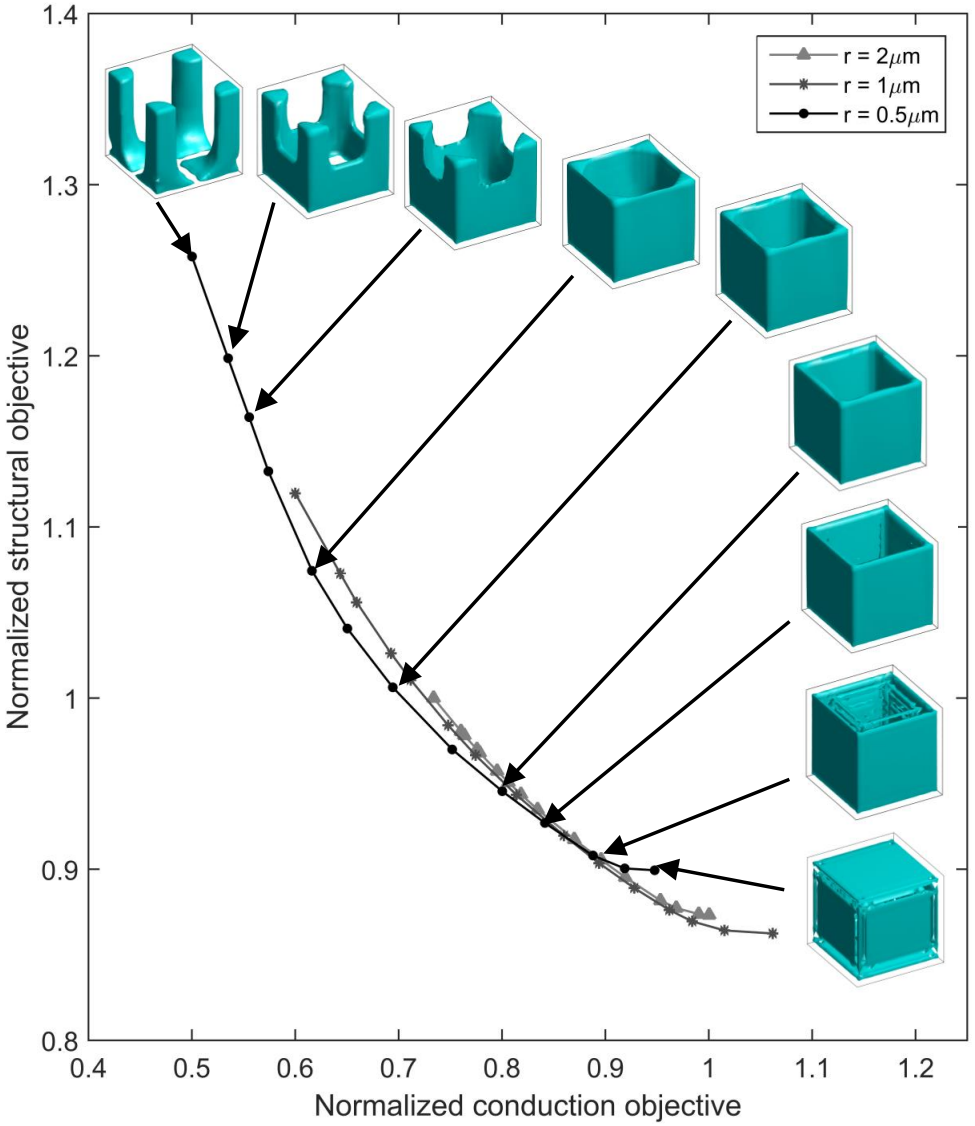

(c) Pareto front

Figure 6.8: Pareto front and optimal topologies for $V_f = 0.30$ and a filter radius of r = 0.5 μm: (a) base cell (*left*) and shifted base cell (*right*) for the full conduction objective, $w_s = 0$, (b) base cell (*left*) and shifted base cell (*right*) for the full structural objective, $w_s = 1$, (c) Pareto fronts for r = 2 μm, r = 1 μm and r = 0.5 μm, and the corresponding optimal structures for r = 0.5 μm for various Pareto weights.

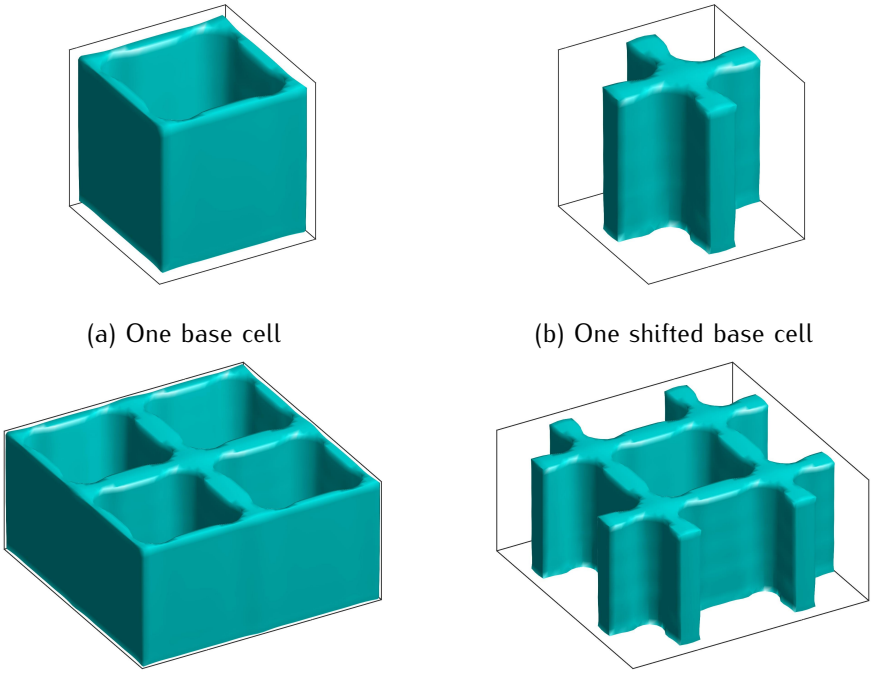

(a) One base cell

(b) One shifted base cell

(c) 2 x 2 base cells

(d) 2 x 2 shifted base cells

Figure 6.9: The intermediate frame structure that provides the best design compromise in terms of the combined minimum structural compliance and maximum electrical conduction objectives for $V_f = 0.30$.

this frame structure is recommended as the best silicon anode design in terms of combined minimum structural compliance and maximum electrical conduction.

6.3.2.2 Influence of volume fraction

The final stage of the parameter investigation was to perform the multi-objective analysis with different prescribed volume fractions in order to assess the effect of this parameter on the Pareto curve and its associated solutions. Two additional volume fraction windows are considered, namely $V_f = 0.40 - 0.45$ and $V_f = 0.55 - 0.60$. Following previous convention, both volume fractions will be subsequently referred to by their upper limit of $V_f = 0.45$ and $V_f = 0.60$, respectively. A filter radius of r = 1 μm was used for these analyses.

The Pareto fronts for volume fractions $V_f = 0.45$ and $V_f = 0.60$ are given in Figures 6.10 and 6.11. In addition to the original base cell (denoted A.), the shifted base cell (denoted B.) is provided for the higher Pareto weights to assist with visualization. The progression of structures along the Pareto fronts appear very similar for both volume fractions, and present

some resemblance to the structures associated with the Pareto curve for a $V_f = 0.30$. Starting at the full structural objective, $w_s = 1$, a cubic structure with holes on the side faces is observed. For the $V_f = 0.45$ the internal structure is floating, while for $V_f = 0.60$ the internal structure is connected to the side walls. A slight decrease in the Pareto weight results in the conduction objective beginning to influence the solution and create a more vertically-oriented structure. The holes on the side faces close, while holes on the top face appear. These holes are smaller for the larger volume fraction. The internal structure becomes a connected conduction pathway between the top and bottom faces. A further reduction in Pareto weight causes the internal structure to begin to disappear, as shown by base cell B., and material begins to accumulate near the sides of the domain. In the center section of the Pareto curve, an intermediate structure is produced which is similar to the frame structure obtained for a $V_f = 0.30$. However, a notable difference is that this intermediate structure does not line the side faces of the base cell. For clarity, Figure 6.12 shows 2 x 2 base cells and 2 x 2 shifted base cells of this intermediate structure for a volume fraction of $V_f = 0.60$. This structure exhibits direct conduction pathways, and also has the interesting feature of the material within the original base cell being able to expand in both inward and outward directions. A small amount of expansion would result in the structure resembling a high volume fraction frame-like structure, similar to that depicted in Figure 6.9. As the weight is further decreased and the conduction objective begins to dominate, the sides of the intermediate structure recede and material gathers at the corners to eventually produce the tapered cylindrical structures for $w_s = 0$.

Figure 6.13 shows the Pareto curves for the volume fractions $V_f = 0.30$, $V_f = 0.45$ and $V_f = 0.60$ and a filter radius of r = 1 μm on the same plot. These individual Pareto curves appear to be constituents of the full Pareto front. This Pareto front clearly depicts the competing nature of the objective function, and illustrates the range of attainable objective function values for the different volume fractions. As expected, the lowest structural objective value is obtained at the lowest volume fraction, while the lowest conduction objective value is obtained by the highest volume fraction. Therefore, in order to best resolve the primary design concern of lithiation-induced mechanical degradation, it is recommended that the silicon anode structures be designed using the rigid frame structure with the lowest practicable volume fraction.

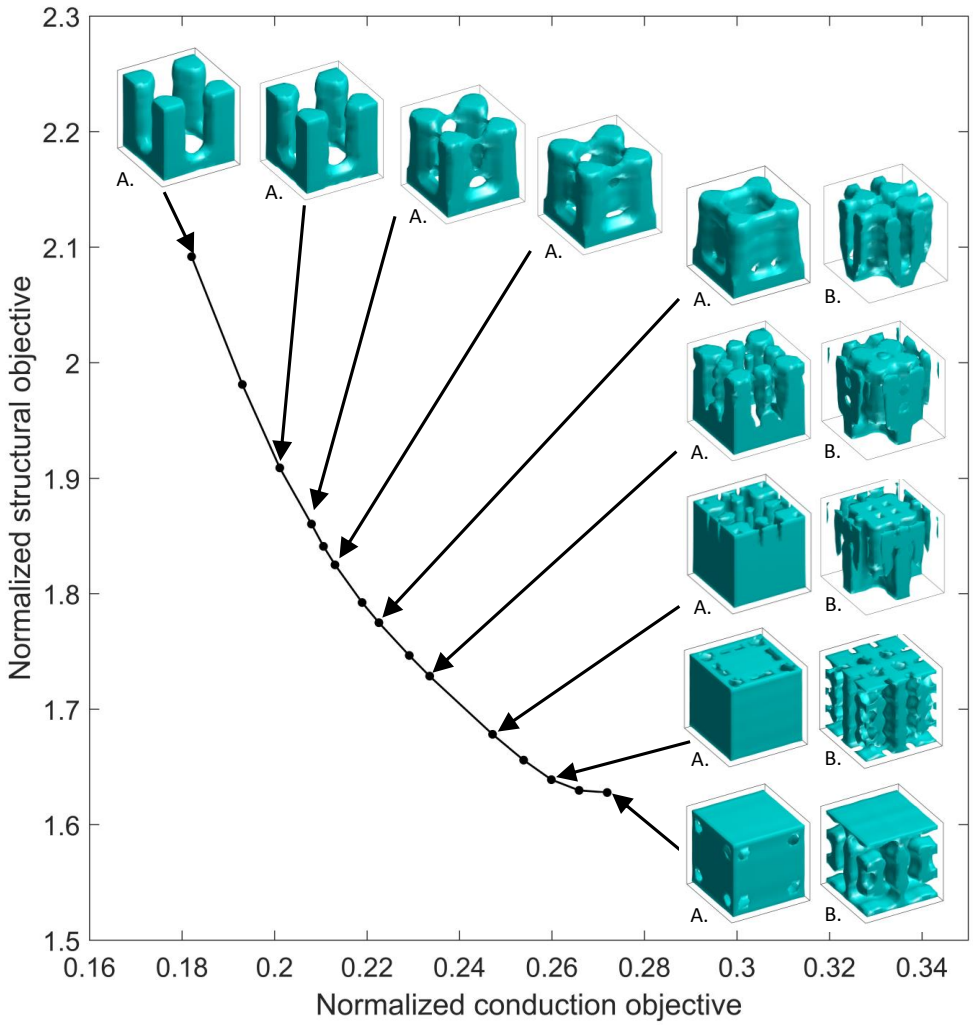

Figure 6.10: Pareto front and corresponding optimal topologies for $V_f = 0.45$ and a filter radius of r = 1 μm.

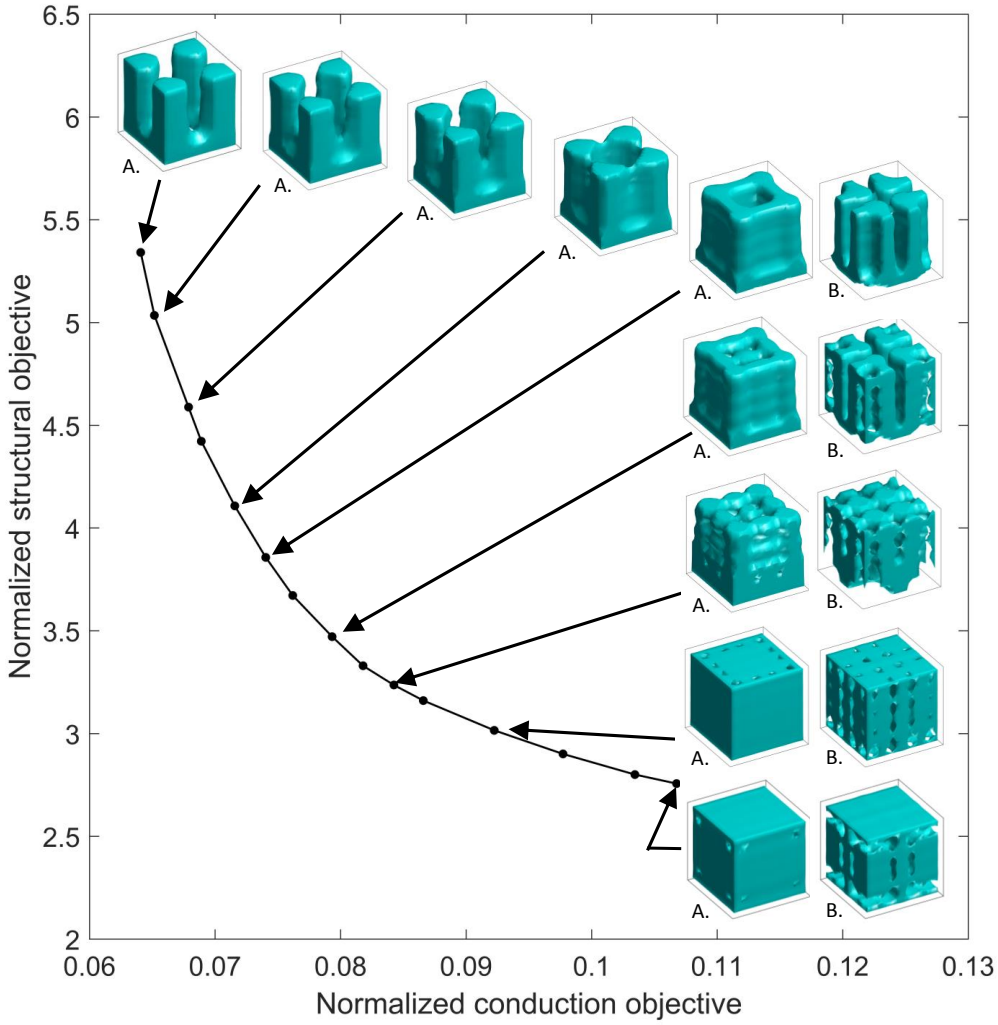

Figure 6.11: Pareto front and corresponding optimal topologies for $V_f = 0.60$ and a filter radius of r = 1 μm.

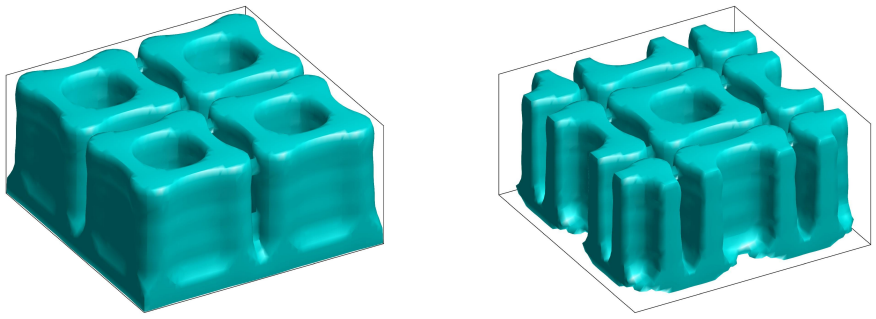

(a) 2 x 2 base cells

(b) 2 x 2 shifted base cells

Figure 6.12: The intermediate structure which provides the best design compromise in terms of the combined minimum structural compliance and maximum electrical conduction objectives for $V_f = 0.60$ and r = 1 μm.

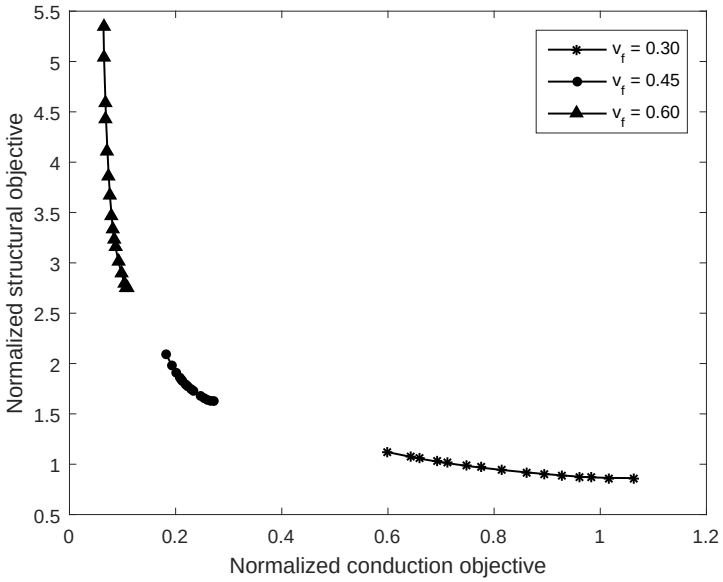

Figure 6.13: Pareto curves for r = 1 μm and $V_f = 0.30$, $V_f = 0.45$ and $V_f = 0.60$.

6.4 Summary

This chapter considered a bi-objective problem formulation that simultaneously optimized both the structural and conduction design criteria that were presented individually in previous chapters. The weighted sum method was used to determine the set of Pareto-optimal points that form the Pareto front. First, a multi-objective test case was implemented in order to verify the underlying computational methodology and implementation. Following this, a selection of anode configurations of varying minimum length scale and volume fraction were optimized using the bi-objective formulation. For a volume fraction of $V_f = 0.30$, it was found that a smaller length scale resulted in a more stable progression of structures, with a distinct intermediate phase that resembled a frame-like structure. This frame structure provided the structural rigidity and direct conduction pathways required by the design objectives. However, due to the smaller length scale not every transition structure was manufacturable, particularly for designs dominated by the structural objective. Larger volume fractions of $V_f = 0.45$ and $V_f = 0.60$ were subsequently optimized, which produced a similar transition of structures as for $V_f = 0.30$. The three tested volume fractions formed an overall Pareto front, which provided a further insight into the competing nature of the structural and conduction design criteria.

Chapter 7

Concluding Remarks and Future Work

7.1 Summary

This thesis presented a topology optimization methodology for the systematic design of optimal multifunctional silicon anode structures in lithium-ion batteries. The methodology utilized density methods, regularization techniques, continuation schemes, and mathematical programming methods such as the globally convergent method of moving asymptotes.

The first stage of this research aimed to address the mechanical degradation of silicon anode structures due to the lithiation-induced expansion. The design objective of minimum compliance was considered, subject to a constraint on volume and design dependent volume expansion that simulated lithiation of the anode structure. The optimal design resembled the triply-periodic Schwarz P minimal surface, which has also been obtained for other design objectives as detailed in the Chapter 2. The results were studied through the investigation of the iteration history, mesh independence, influence of volume fraction, and minimum length scale. A smaller volume fraction was found to yield an improved performance as a result of less volume expansion due to less material, and also larger void spaces that better accommodated the expansion. On the other hand, decreasing the minimum length scale below $r = 2$ μm produced structures unsuitable for manufacture due to their finer features and an internal floating structure that lacked connectivity. Stress analysis indicated that the optimized structures would exhibit significantly improved mechanical performance in comparison to a solid structure of equivalent volume. Furthermore, the results were found to be almost identical for minimum compliance and minimum elastic strain energy formulations and, as such, it may be concluded that these design objectives were equally effective for this particular optimization problem.

The second phase aimed to determine topology optimized anode designs that maximized electrical conduction through the silicon structure. The analysis produced rod-like structures that provided efficient conduction pathways through the thickness of the anode structure, similar to the silicon nanowire structures used by experimentalists. As with the mechanical compliance problem, the iteration history, mesh independence, and influence of volume fraction were studied. A greater volume fraction, by means of a larger cross-sectional area of the rod structure, was found to yield a lower value of electrical compliance and therefore improved conduction performance. A parameter investigation involving the minimum length scale and base cell aspect ratio was also conducted. A reduction in length scale was found to be advantageous by way of a significant decrease in the value of electrical compliance. The smaller length scales of r $= 0.25 - 1.0$ μm resulted in an increased tapering out from the base of the structure, allowing more current to enter the anode. Furthermore, a decrease in length scale resulted in a smaller radius of curvature of the structural features, thereby increasing the electrode-electrolyte interface area. However, once the length scale became very small, checkerboarding behaviour was observed. As such there was a clear trade-off between obtaining the minimum compliance structure, and a structure that was non-physical. Furthermore, increasing the base cell aspect ratio resulted in elongated silicon structures, with similar observed trends as the original aspect ratio for a reduction in length scale.

The final stage of this thesis was to simultaneously address the structural and conduction design criteria using a bi-objective topology optimization formulation. The weighted sum method was used to derive the Pareto fronts for a selection of silicon anode configurations of varying minimum length scales and volume fractions. For a volume fraction of $V_f = 0.30$, it was found to be beneficial to perform the analysis using smaller minimum length scales of r $= 0.5 -$ 1.0 μm. This was due to a considerably more stable progression of structures along the Pareto curve, yet almost coincident Pareto fronts. Furthermore, the smaller length scales produced a consistent frame-like structure for a broad range of intermediate Pareto weights. This frame structure was deemed to be an excellent compromise between the competing design criteria, as it provided both the structural rigidity and direct conduction pathways required by these design objectives. A similar transition of structures was observed for larger volume fractions of $V_f = 0.45$ and $V_f = 0.60$. Interestingly, for these larger volume fractions the intermediate frame structure had slanted sides, allowing expansion in both internal and external directions. Finally, the Pareto fronts of the three volume fractions were combined to form an overall Pareto

front, which provided a key insight into the competing nature of the objective functions, and also the attainable range of objective function values for the different volume fractions. As the mechanical degradation associated with the lithiation-induced expansion was the primary design concern for this thesis, the recommended multifunctional silicon anode design was the rigid frame structure using the lowest practicable volume fraction whilst ensuring sufficient active material to yield the required electrochemical performance of the battery.

The developments and results presented in this thesis provide a solid foundation for the informed design and development of optimal multifunctional silicon anode structures for use in lithium-ion batteries.

7.2 Future work

There are many potential avenues of future work in terms of the computational methodology, the silicon anode design problem, and also application to other design problems. Firstly, the structures presented in this work could be manufactured and tested by experimentalists, or could be incorporated into numerical models of battery systems to simulate the electrochemical performance of the battery as a whole.

With regard to the computational methodology, future developments include incorporating non-linear elasticity to better model the lithiation behaviour of the anode structure. There are some challenges associated with non-linear elasticity topology optimization due to the numerical instabilities that occur as a result of the low density elements in the incremental and iterative non-linear finite element analysis. Despite these difficulties, it may prove fruitful to consider non-linear elasticity for the anode design problem due to the large volume expansion of the silicon structure.

Furthermore, periodic boundary conditions could be implemented as opposed to the sliding boundary conditions used in this work. The periodicity of the structure impacts the solution through the calculation of the sensitivity values, therefore, improved structures may be found by considering periodic boundary conditions, or by maintaining the symmetric boundary conditions and incorporating periodicity into the sensitivity calculations.

Rather than optimizing for stress on a global level using the minimum compliance design objective, another possible area of future work would be to perform stress-based topology optimization. Applying stress-based topology optimization to the silicon anode problem could

produce structures that minimize the local stresses, and would therefore reduce the peak stresses in the structure. Stress-based topology optimization is is an additional challenge due to three key problems, namely the singularity phenomenon, the local nature of stress constraints, and the highly non-linear stress behaviour (Bendsøe & Sigmund, 2003). As such, in recent years there has been significant interest by the topology optimization community in developing techniques to overcome these problems; however, most methods are still in a developmental phase.

In terms of the anode design problem an additional objective function could be implemented, such as considering buckling or maximizing the diffusion of lithium-ions into the anode structure. Diffusion processes greatly influence the performance metrics of the battery, such as the charge and discharge rate and cycling stability. Therefore this design objective would be an excellent addition to the analysis. A large surface area is likely to be characteristic of a maximum diffusion anode structure, which is somewhat at odds with the structures presented in this thesis. It would therefore be interesting to incorporate this objective into the multi-objective analysis to determine its influence on the multifunctional anode structure.

Finally, the methodology developed in this thesis could be directly applied to other design problems with only minor changes to the problem set-up. Possible applications include thermal insulators, which are required to be stiff, lightweight, and inhibit heat transfer through the structure, or exhaust washed structures in aerospace applications which must be mechanically robust and provide efficient conduction pathways to reduce thermal expansion.

Appendix A

Finite Element Formulation for Linear Elasticity

This appendix details the finite element formulation for linear elasticity in order to solve for the nodal displacements throughout the design domain. The strong and weak formulations are given, in addition to the finite element approximation using the Galerkin method, and accompanying computational implementation details. The author recommends standard finite element texts for complete derivations and further reading, for example, Fish & Belytschko (2007); Gosz (2006); Huebner et al. (2001); Kattan (2007); Khennane (2013); Logan (2012); Ross (1998); Zienkiewicz et al. (2013).

A.1 Strong form of the linear elasticity equations

Let us consider a body defined by the volume Ω and outer surface Γ, as shown in Figure A.1. The body is subjected to prescribed displacements $\mathbf{u}^*$ applied on a part of the boundary Γ_u, prescribed boundary tractions $\mathbf{t}^*$ on the boundary Γ_t, and body forces $\mathbf{b}$ such as self-weight are also considered,

$$\mathbf{u} = \mathbf{u}^* \qquad \text{on } \Gamma_u, \tag{A.1}$$

$$\boldsymbol{\sigma}\mathbf{n} = \mathbf{t}^* \qquad \text{on } \Gamma_t. \tag{A.2}$$

The equilibrium equation for (quasistatic) linear elasticity may be expressed in matrix Voigt form as

$$\boldsymbol{\nabla}^T \boldsymbol{\sigma} + \mathbf{b} = \mathbf{0}, \tag{A.3}$$

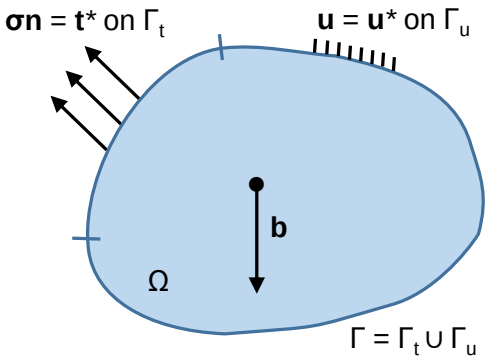

Figure A.1: The reference domain

where ∇ is the symmetric gradient operator

$$\nabla = \begin{bmatrix} \frac{\partial}{\partial x} & 0 & 0 \\ 0 & \frac{\partial}{\partial y} & 0 \\ 0 & 0 & \frac{\partial}{\partial z} \\ \frac{\partial}{\partial y} & \frac{\partial}{\partial x} & 0 \\ 0 & \frac{\partial}{\partial z} & \frac{\partial}{\partial y} \\ \frac{\partial}{\partial z} & 0 & \frac{\partial}{\partial x} \end{bmatrix}, \tag{A.4}$$

$\boldsymbol{\sigma}$ is the vector of stress components and $\mathbf{b}$ is the vector of body forces. The equilibrium equation may be expressed in long form as:

$$\begin{bmatrix} \frac{\partial}{\partial x} & 0 & 0 & \frac{\partial}{\partial y} & 0 & \frac{\partial}{\partial z} \\ 0 & \frac{\partial}{\partial y} & 0 & \frac{\partial}{\partial x} & \frac{\partial}{\partial z} & 0 \\ 0 & 0 & \frac{\partial}{\partial z} & 0 & \frac{\partial}{\partial y} & \frac{\partial}{\partial x} \end{bmatrix} \begin{Bmatrix} \sigma_{xx} \\ \sigma_{yy} \\ \sigma_{zz} \\ \sigma_{xy} \\ \sigma_{yz} \\ \sigma_{xz} \end{Bmatrix} + \begin{Bmatrix} b_x \\ b_y \\ b_z \end{Bmatrix} = \begin{Bmatrix} 0 \\ 0 \\ 0 \end{Bmatrix}. \tag{A.5}$$

A.2 Weak form of the linear elasticity equations

The governing differential equation may be recast into an integral weak form, from which we may obtain accurate approximate solutions. In order to construct the weak form, the equilibrium equation (Equation A.3) is multiplied by an appropriate weight function $\mathbf{W} = [W_x, W_y, W_z]^T$.

This weight function must be admissible, meaning $\mathbf{W}$ and its derivatives must vanish wherever conditions are imposed on $\mathbf{u}(\mathbf{x})$ or its derivatives. This product is then integrated over the domain Ω,

$$\int_{\Omega} \mathbf{W}^T \left(\nabla^T \boldsymbol{\sigma} + \mathbf{b} \right) \, \mathrm{d}\Omega = 0. \tag{A.6}$$

Integration by parts is used to reduce the order of derivatives to a minimum, yielding the weak form of the equilibrium equations for linear elasticity,

$$\int_{\Omega} (\nabla \mathbf{W})^T \, \boldsymbol{\sigma} \, \mathrm{d}\Omega - \int_{\Omega} \mathbf{W}^T \mathbf{b} \, \mathrm{d}\Omega - \int_{\Gamma_t} \mathbf{W}^T \mathbf{t}^* \, \mathrm{d}\Gamma = 0. \tag{A.7}$$

Or equivalently in irreducible form, written completely in terms of displacements using the stress-strain relation $\boldsymbol{\sigma} = \mathbf{C}\boldsymbol{\epsilon}$, and the strain-displacement relation $\boldsymbol{\epsilon} = \nabla \mathbf{u}$, where $\mathbf{C}$ is the constitutive matrix

$$\int_{\Omega} (\nabla \mathbf{W})^T \, \mathbf{C} \nabla \mathbf{u} \, \mathrm{d}\Omega - \int_{\Omega} \mathbf{W}^T \mathbf{b} \, \mathrm{d}\Omega - \int_{\Gamma_t} \mathbf{W}^T \mathbf{t}^* \, \mathrm{d}\Gamma = 0. \tag{A.8}$$

A.3 Finite element approximation by the Galerkin method

The design domain is discretized into isoparametric hexahedral or eight-node brick elements, chosen for their good accuracy and ease of mesh creation (Figure A.2).

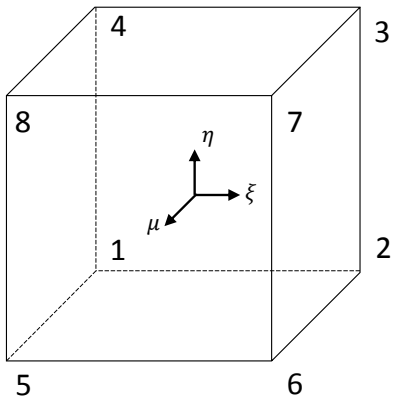

Figure A.2: Eight-node brick element

The associated shape functions are

$$
\begin{aligned}
N_1(\xi,\eta,\mu) &= 1/8(1-\xi)(1-\eta)(1-\mu), \\
N_2(\xi,\eta,\mu) &= 1/8(1+\xi)(1-\eta)(1-\mu), \\
N_3(\xi,\eta,\mu) &= 1/8(1+\xi)(1+\eta)(1-\mu), \\
N_4(\xi,\eta,\mu) &= 1/8(1-\xi)(1+\eta)(1-\mu), \\
N_5(\xi,\eta,\mu) &= 1/8(1-\xi)(1-\eta)(1+\mu), \\
N_6(\xi,\eta,\mu) &= 1/8(1+\xi)(1-\eta)(1+\mu), \\
N_7(\xi,\eta,\mu) &= 1/8(1+\xi)(1+\eta)(1+\mu), \\
N_8(\xi,\eta,\mu) &= 1/8(1-\xi)(1+\eta)(1+\mu).
\end{aligned}
\tag{A.9}
$$

These shape functions, often called tri-linear shape functions as they vary linearly in the ξ, η, and μ directions, are used to map the tri-unit cube in the parent domain into an arbitrary hexahedron in the physical domain. The resulting hexahedron has straight edges but its faces are in general not planar surfaces.

Approximate solutions may be obtained from Equation A.8 by replacing the integrals with a sum of integrals over each element, and inserting appropriate trial solutions and weights based on interpolation functions,

$$
\sum_e \left(\int_{\Omega_e} (\nabla \mathbf{W}_e)^T \, \mathbf{C}_e \nabla \mathbf{u}_e \, d\Omega - \int_{\Omega_e} \mathbf{W}_e{}^T \mathbf{b} \, d\Omega - \int_{\Gamma_{t,e}} \mathbf{W}_e{}^T \mathbf{t}^* \, d\Gamma \right) = 0. \tag{A.10}
$$

The element displacement vector $\mathbf{u}_e$ is given by interpolated nodal values

$$
\mathbf{u}_e = \mathbf{N}_e \mathbf{d}_e, \tag{A.11}
$$

$$\begin{Bmatrix} u_x \\ u_y \\ u_z \end{Bmatrix} = \begin{bmatrix} N_1 & 0 & 0 & N_2 & 0 & 0 & \cdots & N_8 & 0 & 0 \\ 0 & N_1 & 0 & 0 & N_2 & 0 & \cdots & 0 & N_8 & 0 \\ 0 & 0 & N_1 & 0 & 0 & N_2 & \cdots & 0 & 0 & N_8 \end{bmatrix} \begin{Bmatrix} d_{1x} \\ d_{1y} \\ d_{1z} \\ d_{2x} \\ d_{2y} \\ d_{2z} \\ \vdots \\ d_{8x} \\ d_{8y} \\ d_{8z} \end{Bmatrix}, \tag{A.12}$$

where $\mathbf{N}_e$ is the element shape function matrix, and $\mathbf{d}_e$ is the vector of nodal displacements for element e. And similarly for the weights we have

$$\mathbf{W}_e = \mathbf{N}_e \mathbf{w}_e. \tag{A.13}$$

The approximate strain field within an element $\boldsymbol{\epsilon}_e$ may be expressed in terms of nodal displacements using the strain-displacement matrix $\mathbf{B}_e$, often referred to as the B-matrix,

$$\boldsymbol{\epsilon}_e = \begin{Bmatrix} u_{x,x} \\ u_{y,y} \\ u_{z,z} \\ u_{x,y} + u_{y,x} \\ u_{y,z} + u_{z,y} \\ u_{x,z} + u_{z,x} \end{Bmatrix} = \boldsymbol{\nabla} \mathbf{u}_e = \mathbf{B}_e \mathbf{d}_e. \tag{A.14}$$

The B-matrix is a 6 x 24 matrix and can be expressed as

$$\mathbf{B}_e = \begin{bmatrix} \mathbf{B}_1 & \mathbf{B}_2 & \mathbf{B}_3 & \mathbf{B}_4 & \mathbf{B}_5 & \mathbf{B}_6 & \mathbf{B}_7 & \mathbf{B}_8 \end{bmatrix}, \tag{A.15}$$

where

$$\mathbf{B}_i = \begin{bmatrix} N_{i,x} & 0 & 0 \\ 0 & N_{i,y} & 0 \\ 0 & 0 & N_{i,z} \\ N_{i,y} & N_{i,x} & 0 \\ 0 & N_{i,z} & N_{i,y} \\ N_{i,z} & 0 & N_{i,x} \end{bmatrix}. \tag{A.16}$$

Because the shape functions are defined in terms of the natural coordinates, ξ, η, and μ, derivatives of the shape functions with respect to physical coordinates in the B-matrix require the chain rule,

$$\frac{\partial N_i}{\partial \xi} = \frac{\partial N_i}{\partial x}\frac{\partial x}{\partial \xi} + \frac{\partial N_i}{\partial y}\frac{\partial y}{\partial \xi} + \frac{\partial N_i}{\partial z}\frac{\partial z}{\partial \xi}, \tag{A.17}$$

$$\frac{\partial N_i}{\partial \eta} = \frac{\partial N_i}{\partial x}\frac{\partial x}{\partial \eta} + \frac{\partial N_i}{\partial y}\frac{\partial y}{\partial \eta} + \frac{\partial N_i}{\partial z}\frac{\partial z}{\partial \eta}, \tag{A.18}$$

$$\frac{\partial N_i}{\partial \mu} = \frac{\partial N_i}{\partial x}\frac{\partial x}{\partial \mu} + \frac{\partial N_i}{\partial y}\frac{\partial y}{\partial \mu} + \frac{\partial N_i}{\partial z}\frac{\partial z}{\partial \mu}, \tag{A.19}$$

which can be expressed in matrix form

$$\begin{Bmatrix} N_{i,\xi} \\ N_{i,\eta} \\ N_{i,\mu} \end{Bmatrix} = \mathbf{J} \begin{Bmatrix} N_{i,x} \\ N_{i,y} \\ N_{i,z} \end{Bmatrix}, \tag{A.20}$$

or in terms of derivatives with respect to physical coordinates

$$\begin{Bmatrix} N_{i,x} \\ N_{i,y} \\ N_{i,z} \end{Bmatrix} = \mathbf{J}^{-1} \begin{Bmatrix} N_{i,\xi} \\ N_{i,\eta} \\ N_{i,\mu} \end{Bmatrix}, \tag{A.21}$$

where $\mathbf{J}$ is the Jacobian matrix defined by

$$\begin{aligned}\mathbf{J} = \frac{\partial(x, y, z)}{\partial(\xi, \eta, \mu)} &= \begin{bmatrix} \frac{\partial x}{\partial \xi} & \frac{\partial y}{\partial \xi} & \frac{\partial z}{\partial \xi} \\ \frac{\partial x}{\partial \eta} & \frac{\partial y}{\partial \eta} & \frac{\partial z}{\partial \eta} \\ \frac{\partial x}{\partial \mu} & \frac{\partial y}{\partial \mu} & \frac{\partial z}{\partial \mu} \end{bmatrix} \\ &= \begin{bmatrix} N_{1,\xi} & N_{2,\xi} & \cdots & N_{8,\xi} \\ N_{1,\eta} & N_{2,\eta} & \cdots & N_{8,\eta} \\ N_{1,\mu} & N_{2,\mu} & \cdots & N_{8,\mu} \end{bmatrix} \begin{bmatrix} x_1 & y_1 & z_1 \\ x_2 & y_2 & z_2 \\ \vdots & \vdots & \vdots \\ x_8 & y_8 & z_8 \end{bmatrix},\end{aligned} \tag{A.22}$$

with x_i, y_i, and z_i being the coordinates of the ith node. Equation A.10 becomes

$$\sum_e \left(\int_{\Omega_e} \mathbf{W}_e{}^T \mathbf{B}_e{}^T \mathbf{C}_e \mathbf{B}_e \mathbf{d}_e \, \mathrm{d}\Omega - \int_{\Omega_e} \mathbf{W}_e{}^T \mathbf{N}_e{}^T \mathbf{b} \, \mathrm{d}\Omega - \int_{\Gamma_{t,e}} \mathbf{W}_e{}^T \mathbf{N}_e{}^T \mathbf{t}^* \, \mathrm{d}\Gamma \right) = 0. \tag{A.23}$$

Upon assembly of each element's contribution, the weak form may be expressed as

$$\mathbf{W}^T(\mathbf{K}\mathbf{U} - \mathbf{F}) = 0, \tag{A.24}$$

where $\mathbf{K}$ is the global stiffness matrix, $\mathbf{U}$ is the global nodal displacement vector and $\mathbf{F}$ is the global force vector, which may be assembled from the associated elemental expressions, $\mathbf{k}_e$, $\mathbf{d}_e$ and $\mathbf{f}_e$, respectively. Due to the arbitrary nature of $\mathbf{W}$, the governing equation reduces to

$$\mathbf{K}\mathbf{U} = \mathbf{F}. \tag{A.25}$$

A.3.1 The constitutive matrix

The three-dimensional constitutive matrix for an isotropic element e is

$$\mathbf{C}_e(\tilde{x}_e) = E_e(\tilde{x}_e)\bar{\mathbf{C}}_e, \tag{A.26}$$

where $E_e(\tilde{x}_e)$ is the element's Young's modulus which is a function of element density, and $\bar{\mathbf{C}}_e$ is the constitutive matrix for a unit Young's modulus, given by

$$\bar{\mathbf{C}}_e = \frac{1}{(1+\nu)(1-2\nu)} \begin{bmatrix} 1-\nu & \nu & \nu & 0 & 0 & 0 \\ \nu & 1-\nu & \nu & 0 & 0 & 0 \\ \nu & \nu & 1-\nu & 0 & 0 & 0 \\ 0 & 0 & 0 & \frac{(1-2\nu)}{2} & 0 & 0 \\ 0 & 0 & 0 & 0 & \frac{(1-2\nu)}{2} & 0 \\ 0 & 0 & 0 & 0 & 0 & \frac{(1-2\nu)}{2} \end{bmatrix}. \tag{A.27}$$

A.3.2 The element stiffness matrix

The element stiffness matrix is given by

$$\begin{aligned} \mathbf{k}_e(\tilde{x}_e) &= \int_{\Omega_e} \mathbf{B}_e^T \mathbf{C}_e(\tilde{x}_e) \mathbf{B}_e \, \mathrm{d}\Omega \\ &= \int_{-1}^{+1} \int_{-1}^{+1} \int_{-1}^{+1} \mathbf{B}_e^T \mathbf{C}_e(\tilde{x}_e) \mathbf{B}_e \, |\mathbf{J}| \, \mathrm{d}\xi \, \mathrm{d}\eta \, \mathrm{d}\mu \\ &= E_e(\tilde{x}_e) \int_{-1}^{+1} \int_{-1}^{+1} \int_{-1}^{+1} \mathbf{B}_e^T \bar{\mathbf{C}}_e \mathbf{B}_e \, |\mathbf{J}| \, \mathrm{d}\xi \, \mathrm{d}\eta \, \mathrm{d}\mu \\ &= E_e(\tilde{x}_e) \bar{\mathbf{k}}_e, \end{aligned} \tag{A.28}$$

where $\bar{\mathbf{k}}_e$ is the element stiffness matrix for a unit Young's modulus. Moving the density dependent variable outside the integral allows for a single element stiffness calculation that is valid for all elements due to the regularity of the mesh. This integration, typically performed using numerical Gauss quadrature, was carried out using symbolic manipulation software.

A.3.3 The element nodal force vector

The element force vector is comprised of two terms relating to the contributions from body forces and surface tractions

$$\begin{aligned} \mathbf{f}_e &= \mathbf{f}_e^b + \mathbf{f}_e^t \\ &= \int_{\Omega_e} \mathbf{N}_e{}^T \mathbf{b} \, \mathrm{d}\Omega + \int_{\Gamma_{t,e}} \mathbf{N}_e{}^T \mathbf{t}^* \, \mathrm{d}\Gamma. \end{aligned} \tag{A.29}$$

Appendix B

Finite Element Formulation for Steady State Heat Conduction

This appendix details the finite element formulation for steady state heat conduction with no convective heat transfer. The author recommends the following texts for further reading on the heat conduction formulation: Fish & Belytschko (2007); Gosz (2006); Huebner et al. (2001); Lewis et al. (2008); Ross (1998). By using appropriate variable substitutions, this finite element formulation is also valid for steady state electric conduction. More details on the governing equations for electric conduction may be found in texts such as Huebner et al. (2001); Ida (2007); Jin (2002); van Rienen (2012).

B.1 Strong form of the steady-state electric conduction equation

Let us consider a body defined by the volume Ω and outer surface Γ, as shown in Figure B.1. The body is subjected to a prescribed temperature distribution T^* on part of the boundary Γ_T and the normal heat flux q^* is prescribed on the boundary Γ_q,

$$T = T^* \qquad \text{on } \Gamma_T, \tag{B.1}$$

$$\mathbf{q} \cdot \mathbf{n} = q^* \qquad \text{on } \Gamma_q. \tag{B.2}$$

In order to derive the strong form of the steady state heat equation we apply the principle of conservation of energy, which requires the heat flux $\mathbf{q}$ flowing through the boundaries of a control volume must be equal to the heat generated within the boundary S. Both heat flux and internal heat generation have units of energy per unit area and time. The energy balance

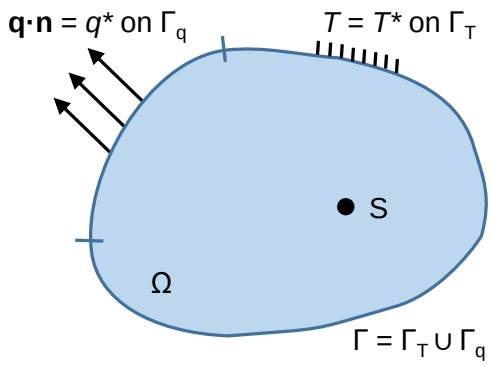

Figure B.1: The reference domain

statement may be written as

$$\nabla \cdot \mathbf{q} - S = 0. \tag{B.3}$$

Fourier's law relates the flux and temperature gradient vectors and is given by

$$\mathbf{q} = -\mathbf{D}\nabla T, \tag{B.4}$$

where $\mathbf{D}$ is the is the conductivity tensor. The negative sign reflects the fact that heat flows in the opposite direction to the gradient. Substituting Fourier's law into the energy balance statement yields the governing partial differential equation for steady-state heat conduction,

$$\nabla^T (\mathbf{D}\nabla T) + S = 0. \tag{B.5}$$

B.2 Weak form of the steady-state heat equation

The governing differential equation may be recast into an integral weak form, from which we may obtain accurate approximate solutions. In order to construct the weak form, the balance equation (Equation B.3) is multiplied by an appropriate scalar-valued test function $W(x, y, z)$. This weight function must be admissible, meaning $W(x, y, z)$ and its derivatives must vanish wherever conditions are imposed on T or its derivatives. This product is then integrated over the domain Ω,

$$\int_\Omega W\,(\nabla\cdot\mathbf{q} - S)\,\mathrm{d}\Omega = 0. \tag{B.6}$$

Integration by parts is used on the flux term of Equation B.6

$$\int_\Omega W\nabla\cdot\mathbf{q}\,\mathrm{d}\Omega = \int_\Omega \nabla\cdot(W\mathbf{q})\,\mathrm{d}\Omega - \int_\Omega \nabla W\cdot\mathbf{q}\,\mathrm{d}\Omega. \tag{B.7}$$

Applying the divergence theorem to the first term of the right hand side of Equation B.7, and subsequently splitting this integral into the prescribed temperature and flux boundaries yields

$$\begin{aligned}\int_\Omega \nabla\cdot(W\mathbf{q})\,\mathrm{d}\Omega &= \int_\Gamma W\mathbf{q}\cdot\mathbf{n}\,\mathrm{d}\Gamma \\ &= \int_{\Gamma_q} Wq^*\,\mathrm{d}\Gamma + \int_{\Gamma_T} W\mathbf{q}\cdot\mathbf{n}\,\mathrm{d}\Gamma.\end{aligned} \tag{B.8}$$

Substituting Equations B.7 and B.8 into Equation B.6 yields

$$-\int_\Omega \nabla W\cdot\mathbf{q}\,\mathrm{d}\Omega + \int_{\Gamma_q} Wq^*\,\mathrm{d}\Gamma + \int_{\Gamma_T} W\mathbf{q}\cdot\mathbf{n}\,\mathrm{d}\Gamma - \int_\Omega WS\,\mathrm{d}\Omega = 0. \tag{B.9}$$

The test functions are set to zero on the prescribed temperature boundaries, causing the integral on Γ_T to vanish. The weak form is therefore given by

$$-\int_\Omega \nabla W\cdot\mathbf{q}\,\mathrm{d}\Omega + \int_{\Gamma_q} Wq^*\,\mathrm{d}\Gamma - \int_\Omega WS\,\mathrm{d}\Omega = 0, \tag{B.10}$$

or equivalently, the weak form may be written in terms of temperature using Fourier's law (Equation B.4)

$$\int_\Omega \nabla W\cdot(\mathbf{D}\nabla T)\,\mathrm{d}\Omega + \int_{\Gamma_q} Wq^*\,\mathrm{d}\Gamma - \int_\Omega WS\,\mathrm{d}\Omega = 0. \tag{B.11}$$

B.3 Finite element approximation by the Galerkin method

As for the finite element formulation for linear elasticity detailed in Appendix A, the design domain is discretized using eight-node brick finite elements with shape functions given in Equation A.9. Approximate solutions may be obtained from Equation B.11 by replacing the integrals with a sum of integrals over each element, and inserting appropriate trial solutions and weights based on interpolation functions,

$$\sum_e \left(\int_{\Omega_e} \nabla W_e\cdot(\mathbf{D}_e\nabla T_e)\,\mathrm{d}\Omega + \int_{\Gamma_{q,e}} W_e q^*\,\mathrm{d}\Gamma - \int_{\Omega_e} W_e S\,\mathrm{d}\Omega \right) = 0. \tag{B.12}$$

The element temperature T_e is given by interpolated nodal values

$$T_e = \mathbf{N}_e \mathbf{t}_e, \tag{B.13}$$

where $\mathbf{N}_e$ is the shape function matrix. For this problem $\mathbf{N}_e$ is a vector as we only have one degree of freedom for each node in the element,

$$\mathbf{N}_e = \begin{bmatrix} N_1 & N_2 & N_3 & N_4 & N_5 & N_6 & N_7 & N_8 \end{bmatrix}, \tag{B.14}$$

and the nodal temperature vector is given by

$$\mathbf{t}_e = \begin{bmatrix} t_1 & t_2 & t_3 & t_4 & t_5 & t_6 & t_7 & t_8 \end{bmatrix}^T. \tag{B.15}$$

And similarly for the weights we have

$$W_e = \mathbf{N}_e \mathbf{w}_e. \tag{B.16}$$

The gradient of the element temperature is given by

$$\nabla T_e = \begin{Bmatrix} \dfrac{\partial T_e}{\partial x} \\ \dfrac{\partial T_e}{\partial y} \\ \dfrac{\partial T_e}{\partial z} \end{Bmatrix} = \mathbf{B}_e \mathbf{t}_e. \tag{B.17}$$

For this problem, the B-matrix is a 3 x 8 matrix

$$\mathbf{B}_e = \begin{bmatrix} \dfrac{\partial N_1^e}{\partial x} & \dfrac{\partial N_2^e}{\partial x} & \cdots & \dfrac{\partial N_8^e}{\partial x} \\ \dfrac{\partial N_1^e}{\partial y} & \dfrac{\partial N_2^e}{\partial y} & \cdots & \dfrac{\partial N_8^e}{\partial y} \\ \dfrac{\partial N_1^e}{\partial z} & \dfrac{\partial N_2^e}{\partial z} & \cdots & \dfrac{\partial N_8^e}{\partial z} \end{bmatrix}. \tag{B.18}$$

The derivatives of the shape functions with respect to the physical coordinates are found using Equation A.21 of Appendix A. Similarly, the gradient of the weight function is given by

$$\nabla W_e = \mathbf{B}_e \mathbf{w}_e. \tag{B.19}$$

The above relations are substituted into Equation B.12

$$\sum_e \left(\int_{\Omega_e} \mathbf{w}_e{}^T \mathbf{B}_e{}^T \mathbf{D}_e \mathbf{B}_e \mathbf{t}_e \, \mathrm{d}\Omega + \int_{\Gamma_{q,e}} \mathbf{N}_e \mathbf{w}_e q^* \, \mathrm{d}\Gamma - \int_{\Omega_e} \mathbf{N}_e \mathbf{w}_e S \, \mathrm{d}\Omega \right) = 0. \tag{B.20}$$

Upon assembly of each element's contribution, the weak form may be expressed as

$$\mathbf{W}^T(\mathbf{K}\mathbf{T} - \mathbf{F}) = 0, \tag{B.21}$$

where $\mathbf{K}$ is the global conductance matrix, $\mathbf{T}$ is the global nodal temperature vector and $\mathbf{F}$ is the global thermal load vector, which may be assembled from the associated elemental expressions, $\mathbf{k}_e$, $\mathbf{t}_e$, and $\mathbf{f}_e$, respectively. Due to the arbitrary nature of $\mathbf{W}$, the governing equation reduces to

$$\mathbf{K}\mathbf{T} = \mathbf{F}. \tag{B.22}$$

B.3.1 Element conductivity matrix

The three-dimensional conductivity matrix for an isotropic element e is

$$\begin{aligned} \mathbf{D}_e(\tilde{x}_e) &= \begin{bmatrix} d_e(\tilde{x}_e) & 0 & \\ 0 & d_e(\tilde{x}_e) & 0 \\ 0 & 0 & d_e(\tilde{x}_e) \end{bmatrix} \\ &= d_e(\tilde{x}_e) \begin{bmatrix} 1 & 0 & 0 \\ 0 & 1 & 0 \\ 0 & 0 & 1 \end{bmatrix} \\ &= d_e(\tilde{x}_e)\mathbf{I}, \end{aligned} \tag{B.23}$$

where $d_e(\tilde{x}_e)$ is the element's conductivity as a function of element density, and $\mathbf{I}$ is the identity matrix.

B.3.2 Element conductance matrix

The element conductance matrix is given by

$$\begin{aligned}\mathbf{k}_e(\tilde{x}_e) &= \int_{\Omega_e} \mathbf{B}_e^T \mathbf{D}_e(\tilde{x}_e)\mathbf{B}_e \, \mathrm{d}\Omega \\ &= \int_{-1}^{+1}\int_{-1}^{+1}\int_{-1}^{+1} \mathbf{B}_e^T \mathbf{D}_e(\tilde{x}_e)\mathbf{B}_e \, |\mathbf{J}| \, \mathrm{d}\xi \, \mathrm{d}\eta \, \mathrm{d}\mu \\ &= d_e(\tilde{x}_e) \int_{-1}^{+1}\int_{-1}^{+1}\int_{-1}^{+1} \mathbf{B}_e^T \mathbf{I} \mathbf{B}_e \, |\mathbf{J}| \, \mathrm{d}\xi \, \mathrm{d}\eta \, \mathrm{d}\mu \\ &= d_e(\tilde{x}_e)\bar{\mathbf{k}}_e,\end{aligned} \tag{B.24}$$

where $\bar{\mathbf{k}}_e$ is the element conductance for a unit thermal conductivity. Moving the density dependant variable from the integral allows for a single element conductance calculation that is valid for all elements due to the regularity of the mesh. This integration, typically performed using numerical Gauss quadrature, was carried out using symbolic manipulation software.

B.3.3 Element nodal thermal load vector

The element nodal thermal load vector is given by two terms, the element boundary flux vector and the element source flux vector

$$\begin{aligned}\mathbf{f}_e &= \mathbf{f}_e^q + \mathbf{f}_e^s \\ &= -\int_{\Gamma_{q,e}} \mathbf{N}_e{}^T q^* \, \mathrm{d}\Gamma + \int_{\Omega_e} \mathbf{N}_e{}^T S \, \mathrm{d}\Omega.\end{aligned} \tag{B.25}$$

Bibliography

Aifantis, K., Hackney, S., & Kumar, R. (2010). *High Energy Density Lithium Batteries: Materials, Engineering, Applications*. Wiley.

Andreassen, E., Lazarov, B. S., & Sigmund, O. (2014). Design of manufacturable 3D extremal elastic microstructure. *Mechanics of Materials*, *69*(1), 1–10.

Arico, A. S., Bruce, P., Scrosati, B., Tarascon, J.-M., & Van Schalkwijk, W. (2005). Nanostructured materials for advanced energy conversion and storage devices. *Nature materials*, *4*(5), 366–377.

Baggetto, L., Danilov, D., & Notten, P. H. L. (2011). Honeycomb-structured silicon: Remarkable morphological changes induced by electrochemical (de)lithiation. *Advanced Materials*, *23*(13), 1563–1566.

Baggetto, L., Niessen, R. A. H., Roozeboom, F., & Notten, P. H. L. (2008). High energy density all-solid-state batteries: A challenging concept towards 3D integration. *Advanced Functional Materials*, *18*(7), 1057–1066.

Beaulieu, L. Y., Eberman, K. W., Turner, R. L., Krause, L. J., & Dahn, J. R. (2001). Colossal reversible volume changes in lithium alloys. *Electrochemical and Solid State Letters*, *4*.

Beaulieu, L. Y., Hatchard, T. D., Bonakdarpour, A., Fleischauer, M. D., & Dahn, J. R. (2003). Reaction of Li with alloy thin films studied by in situ AFM . *Journal of The Electrochemical Society*, *150*(11), A1457–A1464.

Bendsøe, M. (1989). Optimal shape design as a material distribution problem. *Structural Optimization*, *1*, 193–202.

Bendsøe, M. (1995). *Optimization of Structural Topology, Shape, and Material*. Springer.

Bendsøe, M. & Sigmund, O. (2003). *Topology Optimization: Theory, Methods and Applications*. Springer.

Bendsøe, M. P. & Kikuchi, N. (1988). Generating optimal topologies in structural design using a homogenization method. *Comput. Methods Appl. Mech. Eng.*, *71*(2), 197–224.

Bendsøe, M. P. & Sigmund, O. (1999). Material interpolation schemes in topology optimization. *Archive of Applied Mechanics*, *69*(9-10), 635–654.

Benedek, R. & Thackeray, M. (2002). Lithium reactions with intermetallic-compound electrodes. *Journal of Power Sources*, *110*(2), 406 – 411.

Bhandakkar, T. K. & Gao, H. (2010). Cohesive modeling of crack nucleation under diffusion induced stresses in a thin strip: Implications on the critical size for flaw tolerant battery electrodes. *International Journal of Solids and Structures*, *47*(10), 1424 – 1434.

Bhandakkar, T. K. & Gao, H. (2011). Cohesive modeling of crack nucleation in a cylindrical electrode under axisymmetric diffusion induced stresses. *International Journal of Solids and Structures*, *48*(16 -17), 2304 – 2309.

Borrvall, T. & Petersson, J. (2001). Large-scale topology optimization in 3D using parallel computing. *Computer Methods in Applied Mechanics and Engineering*, *190*(46-47), 6201 – 6229.

Bourdin, B. (2001). Filters in topology optimization. *International Journal for Numerical Methods in Engineering*, *50*(9), 2143–2158.

Bruns, T. E. (2005). A reevaluation of the SIMP method with filtering and an alternative formulation for solid-void topology optimization. *Structural and Multidisciplinary Optimization*, *30*(6), 428–436.

Bruns, T. E. & Tortorelli, D. A. (2001). Topology optimization of non-linear elastic structures and compliant mechanisms. *Computer Methods in Applied Mechanics and Engineering*, *190*(26), 3443–3459.

Bruyneel, M. & Duysinx, P. (2005). Note on topology optimization of continuum structures including self-weight. *Structural and Multidisciplinary Optimization*, *29*(4), 245–256.

Bucci, G., Nadimpalli, S. P., Sethuraman, V. A., Bower, A. F., & Guduru, P. R. (2014). Measurement and modeling of the mechanical and electrochemical response of amorphous Si thin film electrodes during cyclic lithiation. *Journal of the Mechanics and Physics of Solids*, *62*, 276 – 294. Sixtieth anniversary issue in honor of Professor Rodney Hill.

Ceder, G., Hautier, G., Jain, A., & Ong, S. (2011). Recharging lithium battery research with first-principles methods. *MRS Bulletin*, *36*, 185–191.

Challis, V., Roberts, A., & Wilkins, A. (2008). Design of three dimensional isotropic microstructures for maximized stiffness and conductivity. *International Journal of Solids and Structures*, *45*(14 -15), 4130 – 4146.

Chan, C., Peng, H., Liu, G., McIlwrath, K., Zhang, X., Huggins, R., & Cui, Y. (2008). High-performance lithium battery anodes using silicon nanowires. *Nature Nanotechnology*, *3*, 31–35.

Chen, B.-C., Silva, E. C. N., & Kikuchi, N. (2001). Advances in computational design and optimization with application to MEMS. *International Journal for Numerical Methods in Engineering*, *52*(1-2), 23–62.

Chen, Y., Zhou, S., & Li, Q. (2009). Computational design for multifunctional microstructural composites. *International Journal of Modern Physics B*, *23*(06n07), 1345–1351.

Chen, Y., Zhou, S., & Li, Q. (2010). Multiobjective topology optimization for finite periodic structures. *Computers & Structures*, *88*(11 -12), 806 – 811.

Cheng, Y.-T. & Verbrugge, M. W. (2008). The influence of surface mechanics on diffusion induced stresses within spherical nanoparticles. *Journal of Applied Physics*, *104*(8).

Christensen, J. & Newman, J. (2006). Stress generation and fracture in lithium insertion materials. *Journal of Solid State Electrochemistry*, *10*(5), 293–319.

de Kruijf, N., Zhou, S., Li, Q., & Mai, Y.-W. (2007). Topological design of structures and composite materials with multiobjectives. *International Journal of Solids and Structures*, *44*(22), 7092–7109.

de Lima, C. R., Mello, L. A., Lima, R. G., & Silva, E. C. (2007). Electrical impedance tomography through constrained sequential linear programming: a topology optimization approach. *Measurement Science and Technology*, *18*(9), 2847.

Deaton, J. & Grandhi, R. (2013a). Stiffening of restrained thermal structures via topology optimization. *Structural and Multidisciplinary Optimization*, *48*(4), 731–745.

Deaton, J. & Grandhi, R. (2013b). Stress-based topology optimization of thermal structures. In *Proceedings of the 10th World Congress on Structural and Multidisciplinary Optimization*, Orlando, Florida.

Deaton, J. & Grandhi, R. (2014). A survey of structural and multidisciplinary continuum topology optimization: post 2000. *Structural and Multidisciplinary Optimization*, *49*(1), 1–38.

Dede, E. (2009). Multiphysics topology optimization of heat transfer and fluid flow systems. In *Proceedings of the COMSOL Conference*, Boston, MA.

Deng, J., Yan, J., & Cheng, G. (2013). Multi-objective concurrent topology optimization of thermoelastic structures composed of homogeneous porous material. *Structural and Multidisciplinary Optimization*, *47*(4), 583–597.

Deshpande, R., Cheng, Y.-T., & Verbrugge, M. W. (2010). Modeling diffusion-induced stress in nanowire electrode structures. *Journal of Power Sources*, *195*(15), 5081 – 5088.

Díaz, A. & Sigmund, O. (1995). Checkerboard patterns in layout optimization. *Structural optimization*, *10*(1), 40–45.

Donoso, A. & Sigmund, O. (2004). Topology optimization of multiple physics problems modelled by poisson's equation. *Latin American Journal of Solids and Structures*, *1*(2), 169–189.

Doyle, M., Fuller, T. F., & Newman, J. (1993). Modeling of galvanostatic charge and discharge of the lithium/polymer/insertion cell. *Journal of The Electrochemical Society*, *140*(6), 1526–1533.

Fish, J. & Belytschko, T. (2007). *A First Course in Finite Elements*. John Wiley and Sons.

Fleury, C. & Braibant, V. (1986). Structural optimization: A new dual method using mixed variables. *International Journal for Numerical Methods in Engineering*, *23*, 409–428.

Gao, T. & Zhang, W. (2010). Topology optimization involving thermo-elastic stress loads. *Structural and Multidisciplinary Optimization*, *42*(5), 725–738.

Gao, T., Zhang, W., Zhu, J., Xu, Y., & Bassir, D. (2008). Topology optimization of heat conduction problem involving design-dependent heat load effect. *Finite Elements in Analysis and Design*, *44*(14), 805–813.

Gersborg-Hansen, A., Bendsøe, M., & Sigmund, O. (2006). Topology optimization of heat conduction problems using the finite volume method. *Structural and Multidisciplinary Optimization*, *31*(4), 251–259.

Gibiansky, L. V. & Sigmund, O. (2000). Multiphase composites with extremal bulk modulus. *Journal of the Mechanics and Physics of Solids*, *48*(3), 461–498.

Golmon, S., Maute, K., & Dunn, M. L. (2012). Multiscale design optimization of lithium ion batteries using adjoint sensitivity analysis. *International Journal for Numerical Methods in Engineering*, *92*(5), 475–494.

Golmon, S., Maute, K., & Dunn, M. L. (2014). A design optimization methodology for Li^+ batteries. *Journal of Power Sources*, *253*, 239 – 250.

Gosz, M. (2006). *Finite Element Method: Applications in Solids, Structures, and Heat Transfer*. Taylor and Francis.

Guest, J. K. & Prévost, J. H. (2006). Optimizing multifunctional materials: Design of microstructures for maximized stiffness and fluid permeability. *International Journal of Solids and Structures*, *43*(22-23), 7028 – 7047.

Guest, J. K. & Prévost, J. H. (2007). Design of maximum permeability material structures. *Computer Methods in Applied Mechanics and Engineering*, *196*(4), 1006–1017.

Halkjær, S., Sigmund, O., & Jensen, J. (2006). Maximizing band gaps in plate structures. *Structural and Multidisciplinary Optimization*, *32*(4), 263–275.

Haslinger, J., Hillebrand, A., Kärkkäinen, T., & Miettinen, M. (2002). Optimization of conducting structures by using the homogenization method. *Structural and Multidisciplinary Optimization*, *24*(2), 125–140.

Hassani, B. & Hinton, E. (1998a). A review of homogenization and topology opimization II - analytical and numerical solution of homogenization equations. *Computers and Structures*, *69*(6), 719 – 738.

Hassani, B. & Hinton, E. (1998b). A review of homogenization and topology optimization I - homogenization theory for media with periodic structure. *Computers and Structures*, *69*(6), 707–717.

Hassani, B. & Hinton, E. (1998c). A review of homogenization and topology optimization III - topology optimization using optimality criteria. *Computers and Structures*, *69*(6), 739 – 756.

He, Y., Yu, X., Li, G., Wang, R., Li, H., Wang, Y., Gao, H., & Huang, X. (2012). Shape evolution of patterned amorphous and polycrystalline silicon microarray thin film electrodes caused by lithium insertion and extraction. *Journal of Power Sources*, *216*, 131–138.

Huang, R., Fan, X., Shen, W., & Zhu, J. (2009). Carbon-coated silicon nanowire array films for high-performance lithium-ion battery anodes. *Applied Physics Letters*, *95*(13).

Huang, X., Radman, A., & Xie, Y. (2011). Topological design of microstructures of cellular materials for maximum bulk or shear modulus. *Computational Materials Science*, *50*(6), 1861–1870.

Huang, X., Xie, Y., Jia, B., Li, Q., & Zhou, S. (2012). Evolutionary topology optimization of periodic composites for extremal magnetic permeability and electrical permittivity. *Structural and Multidisciplinary Optimization*, *46*(3), 385–398.

Huebner, K., Dewhirst, D., Smith, D., & Byrom, T. (2001). *The Finite Element Method For Engineers* (Fourth ed.). John Wiley and Sons.

Huggins, R. & Nix, W. (2000). Decrepitation model for capacity loss during cycling of alloys in rechargeable electrochemical systems. *Ionics*, *6*(1-2), 57–63.

Ida, N. (2007). *Engineering Electromagnetics* (2nd ed.). Springer Publishing Company, Incorporated.

Iga, A., Nishiwaki, S., Izui, K., & Yoshimura, M. (2009). Topology optimization for thermal conductors considering design-dependent effects, including heat conduction and convection. *International Journal of Heat and Mass Transfer*, *52*(11), 2721–2732.

Iwai, H., Kuroyanagi, A., Saito, M., Konno, A., Yoshida, H., Yamada, T., & Nishiwaki, S. (2011). Power generation enhancement of solid oxide fuel cell by cathode–electrolyte interface modification in mesoscale assisted by level set-based optimization calculation. *Journal of Power Sources*, *196*(7), 3485–3495.

Jin, J. (2002). *The Finite Element Method in Electromagnetics*. Wiley.

Jog, C. (1996). Distributed-parameter optimization and topology design for non-linear thermoelasticity. *Computer Methods in Applied Mechanics and Engineering*, *132*(1), 117–134.

Kang, Y.-M., Suh, S.-B., & Kim, Y.-S. (2009). First-principle calculation-assisted structural study on the nanoscale phase transition of Si for Li-Ion secondary batteries. *Inorganic Chemistry*, *48*(24), 11631–11635.

Kasavajjula, U., Wang, C., & Appleby, A. (2007). Nano- and bulk-silicon-based insertion anodes for lithium-ion secondary cells. *Journal of Power Sources*, *163*, 1003–1039.

Kattan, P. (2007). *MATLAB Guide to Finite Elements: An Interactive Approach* (Second ed.). Springer.

Khennane, A. (2013). *Introduction to Finite Element Analysis Using MATLAB and Abaqus*. CRC Press.

Kim, C. & Sun, H. (2012). Topology optimization of gas flow channel routes in an automotive fuel cell. *International Journal of Automotive Technology*, *13*(5), 783–789.

Kim, G.-H., Smith, K., Lee, K.-J., Santhanagopalan, S., & Pesaran, A. (2011). Multi-domain modeling of lithium-ion batteries encompassing multi-physics in varied length scales. *Journal of The Electrochemical Society*, *158*(8), A955–A969.

Kim, J. W., Ryu, J. H., Lee, K. T., & Oh, S. M. (2005). Improvement of silicon powder negative electrodes by copper electroless deposition for lithium secondary batteries. *Journal of Power Sources*, *147*(1-2), 227 – 233.

Klankowski, S. A., Rojeski, R. A., Cruden, B. A., Liu, J., Wu, J., & Li, J. (2013). A high-performance lithium-ion battery anode based on the core-shell heterostructure of silicon-coated vertically aligned carbon nanofibers. *J. Mater. Chem. A*, *1*, 1055–1064.

Kohn, R. V. & Strang, G. (1986a). Optimal design and relaxation of variational problems, I. *Communications on Pure and Applied Mathematics*, *39*(1), 113–137.

Kohn, R. V. & Strang, G. (1986b). Optimal design and relaxation of variational problems, II. *Communications on Pure and Applied Mathematics*, *39*(2), 139–182.

Kohn, R. V. & Strang, G. (1986c). Optimal design and relaxation of variational problems, III. *Communications on Pure and Applied Mathematics*, *39*(3), 353–377.

Kohn, R. V. & Wirth, B. (2014). Optimal fine-scale structures in compliance minimization for a uniaxial load. *Proceedings of the Royal Society of London A: Mathematical, Physical and Engineering Sciences*, *470*(2170).

Koski, J. & Silvennoinen, R. (1987). Norm methods and partial weighting in multicriterion optimization of structures. *International Journal for Numerical Methods in Engineering*, *24*(6), 1101–1121.

Kumaresan, K., Sikha, G., & White, R. E. (2008). Thermal model for a li-ion cell. *Journal of The Electrochemical Society*, *155*(2), A164–A171.

Le, C., Norato, J., Bruns, T., Ha, C., & Tortorelli, D. (2010). Stress-based topology optimization for continua. *Structural and Multidisciplinary Optimization*, *41*(4), 605–620.

Lee, E., James, K., & Martins, J. (2012). Stress-constrained topology optimization with design-dependent loading. *Structural and Multidisciplinary Optimization*, *46*(5), 647–661.

Lewis, R., Nithiarasu, P., & Seetharamu, K. (2008). *Fundamentals of the Finite Element Method for Heat and Fluid Flow*. Wiley.

Li, H., Shi, L., Lu, W., Huang, X., & Chen, L. (2001). Studies on capacity loss and capacity fading of nanosized snsb alloy anode for li-ion batteries. *Journal of The Electrochemical Society*, *148*(8), A915–A922.

Li, J. & Dahn, J. R. (2007). An in situ x-ray diffraction study of the reaction of Li with crystalline Si. *Journal of The Electrochemical Society*, *154*(3), A156–A161.

Li, Q., Steven, G., & Xie, Y. (1999a). On equivalence between stress criterion and stiffness criterion in evolutionary structural optimization. *Structural optimization*, *18*(1), 67–73.

Li, Q., Steven, G. P., Querin, O. M., & Xie, Y. (1999). Shape and topology design for heat conduction by evolutionary structural optimization. *International Journal of Heat and Mass Transfer*, *42*(17), 3361 – 3371.

Li, Q., Steven, G. P., & Xie, Y. (1999b). Displacement minimization of thermoelastic structures by evolutionary thickness design. *Computer Methods in Applied Mechanics and Engineering*, *179*(3), 361–378.

Li, Y., Saitou, K., & Kikuchi, N. (2004). Topology optimization of thermally actuated compliant mechanisms considering time-transient effect. *Finite Elements in Analysis and Design*, *40*(11), 1317 – 1331.

Liang, B., Liu, Y., & Xu, Y. (2014). Silicon-based materials as high capacity anodes for next generation lithium ion batteries. *Journal of Power Sources*, *267*(0), 469 – 490.

Liang, L., Zhang, J., Chen, L.-P., & hong Zhang, X. (2010). FVM-based multi-objective topology optimization and Matlab implementation. In *2010 International Conference on Computer Application and System Modeling (ICCASM)*, volume 1, (pp. V1–672–V1–678).

Liu, W.-R., Wang, J.-H., Wu, H.-C., Shieh, D.-T., Yang, M.-H., & Wu, N.-L. (2005). Electrochemical characterizations on Si and C-coated Si particle electrodes for lithium-ion batteries. *Journal of The Electrochemical Society*, *152*(9), A1719–A1725.

Logan, D. (2012). *A First Course in the Finite Element Method* (Fifth ed.). Cengage Learning.

Marler, R. T. & Arora, J. S. (2004). Survey of multi-objective optimization methods for engineering. *Structural and multidisciplinary optimization*, *26*(6), 369–395.

Mello, L., de Lima, C., Amato, M., Lima, R., & Silva, E. (2008). Three-dimensional electrical impedance tomography: A topology optimization approach. *Biomedical Engineering, IEEE Transactions on*, *55*(2), 531–540.

Meyers, M., Mishra, A., & Benson, D. (2006). Mechanical properties of nanocrystalline materials. *Progress in Materials Science*, *51*(4), 427 – 556.

Michell, A. (1904). LVIII. The limits of economy of material in frame-structures. *Philosophical Magazine Series 6*, *8*(47), 589–597.

Neves, M., Rodrigues, H., & Guedes, J. (2000). Optimal design of periodic linear elastic microstructures. *Computers & Structures*, *76*(1-3), 421 – 429.

Newman, J. & Tiedemann, W. (1975). Porous-electrode theory with battery applications. *AIChE Journal*, *21*(1), 25–41.

Nomura, T., Sato, K., Taguchi, K., Kashiwa, T., & Nishiwaki, S. (2007). Structural topology optimization for the design of broadband dielectric resonator antennas using the finite difference time domain technique. *International Journal for Numerical Methods in Engineering*, *71*(11), 1261–1296.

Notten, P., Roozeboom, F., Niessen, R., & Baggetto, L. (2007). 3-D integrated all-solid-state rechargeable batteries. *Advanced Materials*, *19*(24), 4564–4567.

Obrovac, M. N. & Christensen, L. (2004). Structural changes in silicon anodes during lithium insertion/extraction. *Electrochemical and Solid-State Letters*, *7*(5), A93–A96.

Ohara, S., Suzuki, J., Sekine, K., & Takamura, T. (2004). A thin film silicon anode for Li-ion batteries having a very large specific capacity and long cycle life. *Journal of Power Sources*, *136*(2), 303 – 306. Selected papers presented at the International Power Sources Symposium.

Olhoff, N., Bendsøe, M. P., & Rasmussen, J. (1991). On CAD-integrated structural topology and design optimization. *Computer Methods in Applied Mechanics and Engineering*, *89*(1-3), 259 – 279. Second World Congress on Computational Mechanics.

Oudenhoven, J. F. M., Baggetto, L., & Notten, P. H. L. (2011). All-solid-state lithium-ion microbatteries: A review of various three-dimensional concepts. *Advanced Energy Materials*, *1*(1), 10–33.

Pareto, V. (1906). *Manuale di Economia Politica, Societa Editrice Libraria.* Translated into English by A.S. Schwier as *Manual of Political Economy*, edited by A. S. Schwier and A.N. Page, 1971. New York: A.M. Kelley.

Patil, S., Zhou, S. W., & Li, Q. (2008). Design of periodic microstructural materials by using evolutionary structural optimization method. *Advanced Materials Research*, *32*, 279–283.

Paulino, G. H., Silva, E. C. N., & Le, C. H. (2009). Optimal design of periodic functionally graded composites with prescribed properties. *Structural and Multidisciplinary Optimization*, *38*(5), 469–489.

Pedersen, P. & Pedersen, N. (2008). Design of notches and grooves by means of elliptic shapes. *The Journal of Strain Analysis for Engineering Design*, *43*(1), 1–14.

Pedersen, P. & Pedersen, N. (2010a). Strength optimized designs of thermoelastic structures. *Structural and Multidisciplinary Optimization*, *42*(5), 681–691.

Pedersen, P. & Pedersen, N. (2010b). Strength optimized designs of thermoelastic structures. *Structural and Multidisciplinary Optimization*, *42*(5), 681–691.

Pedersen, P. & Pedersen, N. (2012). Interpolation/penalization applied for strength design of 3D thermoelastic structures. *Structural and Multidisciplinary Optimization*, *45*(6), 773–786.

Peng, K., Jie, J., Zhang, W., & Lee, S.-T. (2008). Silicon nanowires for rechargeable lithium-ion battery anodes. *Applied Physics Letters*, *93*(3), 033105.

Penzler, P., Rumpf, M., & Wirth, B. (2012). A phase-field model for compliance shape optimization in nonlinear elasticity. *ESAIM: Control, Optimisation and Calculus of Variations*, *18*(01), 229–258.

Petrova, S. I. (2010). Topology optimization of eddy current systems by level-set and primal-dual methods. In *Proceedings of the International MultiConference of Engineers and Computer Scientists*, volume 1.

Prager, W. (1968). Optimality criteria in structural design. *Proceedings of the National Academy of Sciences of the United States of America*, *61*(3), 794.

Querin, O., Young, V., Steven, G., & Xie, Y. (2000). Computational efficiency and validation of bi-directional evolutionary structural optimisation. *Computer methods in applied mechanics and engineering*, *189*(2), 559–573.

Quiroga-González, E., Carstensen, J., & Föll, H. (2013). Optimal conditions for fast charging and long cycling stability of silicon microwire anodes for lithium ion batteries, and comparison with the performance of other Si anode concepts. *Energies*, *6*(10), 5145–5156.

Rodrigues, H. & Fernandes, P. (1995). A material based model for topology optimization of thermoelastic structures. *International Journal for Numerical Methods in Engineering*, *38*(12), 1951–1965.

Ross, C. (1998). *Advanced Applied Finite Element Methods*. Horwood Publishing.

Rozvany, G. I. (2009). A critical review of established methods of structural topology optimization. *Structural and Multidisciplinary Optimization*, *37*(3), 217–237.

Ryu, J. H., Kim, J. W., Sung, Y.-E., & Oh, S. M. (2004). Failure modes of silicon powder negative electrode in lithium secondary batteries. *Electrochemical and Solid-State Letters*, *7*(10), A306–A309.

Salvadori, A., Bosco, E., & Grazioli, D. (2014). A computational homogenization approach for Li-ion battery cells: Part 1 - formulation. *Journal of the Mechanics and Physics of Solids*, *65*, 114 – 137.

Schwarz, H. A. (1890). *Gesammelte Mathematische Abhandlungen*. Springer.

Scrosati, B. & Garche, J. (2010). Lithium batteries: Status, prospects and future. *Journal of Power Sources*, *195*(9), 2419 – 2430.

Sethian, J. & Wiegmann, A. (2000). Structural boundary design via level set and immersed interface methods. *Journal of Computational Physics*, *163*(2), 489 – 528.

Sethuraman, V. A., Chon, M. J., Shimshak, M., Srinivasan, V., & Guduru, P. R. (2010). In situ measurements of stress evolution in silicon thin films during electrochemical lithiation and delithiation. *Journal of Power Sources*, *195*(15), 5062 – 5066.

Shenoy, V., Johari, P., & Qi, Y. (2010). Elastic softening of amorphous and crystalline Li-Si phases with increasing Li concentration: a first-principles study. *Journal of Power Sources*, *195*(19), 6825–6830.

Shin, H.-C., Corno, J. A., Gole, J. L., & Liu, M. (2005). Porous silicon negative electrodes for rechargeable lithium batteries. *Journal of Power Sources*, *139*(1-2), 314 – 320.

Shukla, A. & Prem Kumar, T. (2008). Materials for next-generation lithium batteries. *Current Science*, *94*(3), 314–331.

Sigmund, O. (1994). Materials with prescribed constitutive parameters: an inverse homogenization problem. *International Journal of Solids and Structures*, *31*(17), 2313–2329.

Sigmund, O. (2000). A new class of extremal composites. *Journal of the Mechanics and Physics of Solids*, *48*(2), 397 – 428.

Sigmund, O. (2001a). Design of multiphysics actuators using topology optimization - Part I: One-material structures. *Computer Methods in Applied Mechanics and Engineering*, *190*(49-50), 6577 – 6604.

Sigmund, O. (2001b). Design of multiphysics actuators using topology optimization - Part II: Two-material structures. *Computer Methods in Applied Mechanics and Engineering*, *190*(49-50), 6605 – 6627.

Sigmund, O. & Jensen, J. S. (2003). Systematic design of phononic band–gap materials and structures by topology optimization. *Philosophical Transactions of the Royal Society of London A: Mathematical, Physical and Engineering Sciences*, *361*(1806), 1001–1019.

Sigmund, O. & Petersson, J. (1998). Numerical instabilities in topology optimization: A survey on procedures dealing with checkerboards, mesh-dependencies and local minima. *Structural optimization*, *16*(1), 68–75.

Sigmund, O. & Torquato, S. (1996). Composites with extremal thermal expansion coefficients. *Applied Physics Letters*, *69*(21), 3203–3205.

Sigmund, O. & Torquato, S. (1997). Design of materials with extreme thermal expansion using a three-phase topology optimization method. *Journal of the Mechanics and Physics of Solids*, *45*(6), 1037 – 1067.

Sigmund, O. & Torquato, S. (1998). Design of materials with extreme elastic or thermoelastic properties using topology optimization. In *IUTAM Symposium on Transformation Problems in Composite and Active Materials*, volume 60, (pp. 233). Springer Science & Business Media.

Song, X., Diaz, A., & Benard, A. (2013). A 3D topology optimization model of the cathode air supply channel in planar solid oxide fuel cell. In *Proceedings of the 10th World Congress on Structural and Multidisciplinary Optimization*, Orlando, Florida.

Song, X., Diaz, A., Benard, A., & Nicholas, J. (2013). A 2D model for shape optimization of solid oxide fuel cell cathodes. *Structural and Multidisciplinary Optimization*, *47*(3), 453–464.

Spotnitz, R. (2003). Simulation of capacity fade in lithium-ion batteries. *Journal of Power Sources*, *113*(1), 72 – 80.

Stolpe, M. & Svanberg, K. (2001a). An alternative interpolation scheme for minimum compliance topology optimization. *Structural and Multidisciplinary Optimization*, *22*(2), 116–124.

Stolpe, M. & Svanberg, K. (2001b). On the trajectories of penalization methods for topology optimization. *Structural and Multidisciplinary Optimization*, *21*(2), 128–139.

Suresh, K. (2010). A 199-line matlab code for pareto-optimal tracing in topology optimization. *Structural and Multidisciplinary Optimization*, *42*(5), 665–679.

Suresh, K. (2013). Efficient generation of large-scale pareto-optimal topologies. *Structural and Multidisciplinary Optimization*, *47*(1), 49–61.

Svanberg, K. (1987). The method of moving asymptotes - a new method for structural optimization. *International Journal for Numerical Methods in Engineering*, *24*(2), 359–373.

Svanberg, K. (2002). A class of globally convergent optimization methods based on conservative convex separable approximations. *SIAM Journal on Optimization*, *12*(2), 555–573.

Szczech, J. R. & Jin, S. (2011). Nanostructured silicon for high capacity lithium battery anodes. *Energy Environ. Sci.*, *4*, 56–72.

Takamura, T., Uehara, M., Suzuki, J., Sekine, K., & Tamura, K. (2006). High capacity and long cycle life silicon anode for Li-ion battery. *Journal of Power Sources*, *158*(2), 1401 – 1404.

Takezawa, A., Yoon, G. H., Jeong, S. H., Kobashi, M., & Kitamura, M. (2014). Structural topology optimization with strength and heat conduction constraints. *Computer Methods in Applied Mechanics and Engineering*, *276*, 341 – 361.

Teki, R., Datta, M. K., Krishnan, R., Parker, T. C., Lu, T.-M., Kumta, P. N., & Koratkar, N. (2009). Nanostructured silicon anodes for lithium ion rechargeable batteries. *Small*, *5*(20), 2236–2242.

Torquato, S. & Donev, A. (2004). Minimal surfaces and multifunctionality. *Proceedings of the Royal Society of London A: Mathematical, Physical and Engineering Sciences*, *460*(2047), 1849–1856.

Torquato, S., Hyun, S., & Donev, A. (2002). Multifunctional composites: Optimizing microstructures for simultaneous transport of heat and electricity. *Phys. Rev. Lett.*, *89*, 266601.

Torquato, S., Hyun, S., & Donev, A. (2003). Optimal design of manufacturable three-dimensional composites with multifunctional characteristics. *Journal of Applied Physics*, *94*(9), 5748–5755.

Turteltaub, S. & Washabaugh, P. (1999). Optimal distribution of material properties for an elastic continuum with structure-dependent body force. *International Journal of Solids and Structures*, *36*(30), 4587 – 4608.

van Rienen, U. (2012). *Numerical Methods in Computational Electrodynamics: Linear Systems in Practical Applications*. Lecture Notes in Computational Science and Engineering. Springer Berlin Heidelberg.

Wachtler, M., Winter, M., & Besenhard, J. O. (2002). Anodic materials for rechargeable Li-batteries. *Journal of Power Sources*, *105*(2), 151 – 160. 7th Ulmer Elektrochemische Tage.

Wang, B., Yan, J., & Cheng, G. (2011). Optimal structure design with low thermal directional expansion and high stiffness. *Engineering Optimization*, *43*(6), 581–595.

Wang, C.-W. & Sastry, A. M. (2007). Mesoscale modeling of a Li-ion polymer cell. *Journal of The Electrochemical Society*, *154*(11), A1035–A1047.

Woodford, W. H., Chiang, Y.-M., & Carter, W. C. (2010). "Electrochemical shock" of intercalation electrodes: A fracture mechanics analysis. *Journal of The Electrochemical Society*, *157*(10), A1052–A1059.

Xia, Q. & Wang, M. (2008). Topology optimization of thermoelastic structures using level set method. *Computational Mechanics*, *42*(6), 837–857.

Xie, Y. & Steven, G. P. (1993). A simple evolutionary procedure for structural optimization. *Computers & structures*, *49*(5), 885–896.

Yan, J., Cheng, G.-d., & Liu, L. (2008). A uniform optimum material based model for concurrent optimization of thermoelastic structures and materials. *International Journal for Simulation and Multidisciplinary Design Optimization*, *2*(4), 259–266.

Yang, J., Wachtler, M., Winter, M., & Besenhard, J. O. (1999). Sub-microcrystalline Sn and Sn-SnSb powders as lithium storage materials for lithium-ion batteries. *Electrochemical and Solid-State Letters*, *2*(4), 161–163.

Yang, J., Winter, M., & Besenhard, J. (1996). Small particle size multiphase Li-alloy anodes for lithium-ion batteries. *Solid State Ionics*, *90*(1-4), 281 – 287.

Yang, Z., Lu, Z., & Zhao, Y.-P. (2009). Shape effects on the yield stress and deformation of silicon nanowires: A molecular dynamics simulation. *Journal of Applied Physics*, *106*(2), 023537.

Yin, L. & Ananthasuresh, G. (2001). Topology optimization of compliant mechanisms with multiple materials using a peak function material interpolation scheme. *Structural and Multidisciplinary Optimization*, *23*(1), 49–62.

Yin, L. & Ananthasuresh, G. (2002). A novel topology design scheme for the multi-physics problems of electro-thermally actuated compliant micromechanisms. *Sensors and Actuators A: Physical*, *97-98*, 599 – 609. Selected papers from Eurosenors {XV}.

Yip, S. (1998). Nanocrystals: the strongest size. *Nature*, *391*(6667), 532–533.

Yoshio, M., Wang, H., Fukuda, K., Umeno, T., Dimov, N., & Ogumi, Z. (2002). Carbon-coated Si as a lithium-ion battery anode material. *Journal of The Electrochemical Society*, *149*(12), A1598–A1603.

Zadeh, L. (1963). Optimality and non-scalar-valued performance criteria. *Automatic Control, IEEE Transactions on*, *8*(1), 59–60.

Zadin, V., Brandell, D., KasemÃďgi, H., Lellep, J., & Aabloo, A. (2013). Designing the 3D-microbattery geometry using the level-set method. *Journal of Power Sources*, *244*, 417 – 428. 16th International Meeting on Lithium Batteries (IMLB).

Zhang, W., Dai, G., Wang, F., Sun, S., & Bassir, H. (2007). Using strain energy-based prediction of effective elastic properties in topology optimization of material microstructures. *Acta Mechanica Sinica*, *23*(1), 77–89.

Zhang, W., Yang, J., Xu, Y., & Gao, T. (2014). Topology optimization of thermoelastic structures: mean compliance minimization or elastic strain energy minimization. *Structural and Multidisciplinary Optimization*, *49*(3), 417–429.

Zhang, W.-J. (2011). A review of the electrochemical performance of alloy anodes for lithium-ion batteries. *Journal of Power Sources*, *196*(1), 13–24.

Zhang, X., Sastry, A. M., & Shyy, W. (2008). Intercalation-induced stress and heat generation within single lithium-ion battery cathode particles. *Journal of The Electrochemical Society*, *155*(7), A542–A552.

Zhou, M. & Rozvany, G. (1991). The COC algorithm, Part II: topological, geometrical and generalized shape optimization. *Computer Methods in Applied Mechanics and Engineering*, *89*(1), 309–336.

Zhou, S., Cadman, J., Chen, Y., Li, W., Xie, Y. M., Huang, X., Appleyard, R., Sun, G., & Li, Q. (2012). Design and fabrication of biphasic cellular materials with transport properties - a modified bidirectional evolutionary structural optimization procedure and MATLAB program. *International Journal of Heat and Mass Transfer*, *55*(25), 8149–8162.

Zhou, S. & Li, Q. (2007). The relation of constant mean curvature surfaces to multiphase composites with extremal thermal conductivity. *Journal of Physics D: Applied Physics*, *40*(19), 6083.

Zhou, S. & Li, Q. (2008a). Computational design of microstructural composites with tailored thermal conductivity. *Numerical Heat Transfer, Part A: Applications*, *54*(7), 686–708.

Zhou, S. & Li, Q. (2008b). Computational design of multi-phase microstructural materials for extremal conductivity. *Computational Materials Science*, *43*(3), 549 – 564.

Zhou, S. & Li, Q. (2008c). Design of graded two-phase microstructures for tailored elasticity gradients. *Journal of Materials Science*, *43*(15), 5157–5167.

Zhou, S., Li, W., & Li, Q. (2010a). Design of 3-D periodic metamaterials for electromagnetic properties. *Microwave Theory and Techniques, IEEE Transactions on*, *58*(4), 910–916.

Zhou, S., Li, W., & Li, Q. (2010b). Level-set based topology optimization for electromagnetic dipole antenna design. *Journal of Computational Physics*, *229*(19), 6915 – 6930.

Zhuang, C., Xiong, Z., & Ding, H. (2007). A level set method for topology optimization of heat conduction problem under multiple load cases. *Computer Methods in Applied Mechanics and Engineering*, *196*(4-6), 1074 – 1084.

Zienkiewicz, O., Taylor, R., & Zhu, J. (2013). *The Finite Element Method: Its Basis and Fundamentals* (Seventh ed.). Oxford: Butterworth-Heinemann.

Zuo, K.-T., Chen, L.-P., Zhang, Y.-Q., & Yang, J. (2007). Study of key algorithms in topology optimization. *The International Journal of Advanced Manufacturing Technology*, *32*(7-8), 787–796.